On the Flow
in
Centrifugal Impellers

Frank C. Visser

CIP-GEGEVENS KONINKLIJKE BIBLIOTHEEK, DEN HAAG

Visser, Frank C.

On the flow in centrifugal impellers / Frank C. Visser. -
[S.l. : s.n.]
Proefschrift Universiteit Twente, Enschede. - Met lit.
opg. - Met samenvatting in het Nederlands.
ISBN 90-9008954-3
Trefw.: roterende systemen / centrifugaalkrachten /
stromingsleer.

ON THE FLOW
IN
CENTRIFUGAL IMPELLERS

PROEFSCHRIFT

Ter verkrijging van
de graad van doctor aan de Universiteit Twente,
op gezag van de rector magnificus,
prof.dr. Th.J.A. Popma,
volgens het besluit van het College voor promoties
in het openbaar te verdedigen
op donderdag 15 februari 1996 te 15.00 uur

door

Franciscus Cornelis Visser

geboren op 3 mei 1962
te Alkmaar

Dit proefschrift is goedgekeurd door de promotor:

prof.dr.ir. J.J.H. Brouwers

en de assistentpromotor:

dr.ir. J.B. Jonker

Aan Lenneke

Contents

Introductory remarks

This thesis is the outgrowth of the work carried out over the last couple of years at the Laboratory of Thermal Engineering of the University of Twente. It is divided into two chapters, which deal with the flow of an incompressible fluid in centrifugal impellers of low specific speed. These impellers are, basically, of the radial-flow type, in which the flow field may be considered two-dimensional for the larger part.

The first chapter is devoted in its entirety to the theory of the flow, and presents a non-numerical mathematical analysis based on the assumption of two-dimensional, irrotational, and solenoidal flow, with solutions in closed form and applications to impeller design.

The second chapter gives an account of the experimental investigation that was carried out into the flow conditions in (model) impellers of centrifugal pumps; the results of which principally served to verify the findings of the first chapter, but also initiated some further theoretical analysis into the effect of viscosity.

The thesis does not contain a general explanatory introduction, other than the one given here, because the basic concepts and ideas relating to the subject-matter are outlined thoroughly in the introductory part of the respective chapters. Moreover, it is assumed that the reader has a certain maturity with respect to the subject, including some general (working) knowledge of complex-function theory and special functions.

The subdivision into merely two (large) chapters originated from the desire to have separate coverage of the two topics: Theory & Experiment. As a result the two chapters can be read (almost) independently.

F. C. V.

Chapter 1

Theoretical analysis of inertially irrotational and solenoidal flow in two-dimensional radial-flow pump and turbine impellers with equiangular blades[*]

Abstract. *Using the theory of functions of a complex variable, in particular the method of conformal mapping, the irrotational and solenoidal flow in two-dimensional radial-flow pump and turbine impellers equipped with equiangular blades is analysed. Exact solutions are given for the fluid velocity along straight radial pump and turbine impeller blades, while for logarithmic spiral pump impeller blades solutions are given which hold asymptotically as* $(r_1/r_2)^{n/\cos(\beta)} \to 0$, *in which* r_1 *is impeller inner radius,* r_2 *is impeller outer radius,* n *is the number of blades and* β *is the blade angle. Both solutions are given in terms of a Fourier series, with the Fourier coefficients being given by the (Gauss) hypergeometric function and the beta function respectively. Furthermore, an expression for the blade-to-blade passage-flow velocity is presented that holds asymptotically in a region well away from the blade tips.*

The solutions presented, are used to derive analytical expressions for a number of parameters which are important for practical design of radial-flow turbomachinery, and which reflect the two-dimensional nature of the flow field. Parameters include rotational slip of the flow leaving radial impellers, hydrodynamic loading of the blades, conditions to avoid reverse flow between the blades, and conditions for shockless flow at impeller entry, with the number of blades and blade curvature as variables. In addition, analytical extensions to classical one-dimensional Eulerian-based expressions for developed head of pumps and delivered work of turbines are discussed, as well as the preliminary design of impeller housings.

1.1 Introduction

Computing the two-dimensional potential flow in radial-flow impellers, in particular by using the theory of functions of a complex variable, is not a recent development but has been done by a number of notable authors since the early years of this century. It was Kucharski (1918) who pioneered this field of fluid dynamics by thoroughly examining the flow field of a simplified impeller fitted out with straight radial blades with the inner tip placed at the centre of the impeller. Spannhake (1925*a*, *b*, 1930) presented improvements

---

[*] This chapter has been published for the greater part (under the same title) in *J. Fluid Mech. (1994), vol. 269, pp. 107-141.*

by taking a more realistic inlet-to-outlet radius ratio for the impeller, and introduced the method of conformal mapping to solve the flow problem. Employing the method of conformal mapping Sörensen (1972), Busemann (1928), and Schulz (1928*a*, *b*) treated the impeller with logarithmic spiral blades. Here Schulz developed and subsequently used a rather dubious alternative mapping, in that it violated the conservation of flux and circulation. Sörensen and Busemann based their study correctly on the work of König (1922). Uchimaru & Kito (1931) unfortunately applied the (questionable) results of Schulz to compute slip coefficients. Acosta (1954) extended the work of Busemann by computing the pressure distribution along the blades, and compared the results with experiments. Ayyubi & Rao (1971), and Mohana Kumar & Rao (1977) used Acosta's work as reference and developed similar results by using a distribution of elementary singularities on the blade surfaces.

The above-mentioned authors all contributed significantly to the solution of the potential flow problem in two-dimensional radial-flow impellers. However, results were mostly obtained by numerical evaluation and computation; solutions in closed form were limited to special cases only (Kucharski 1918; Spannhake 1925*a*). This situation is improved by the results outlined in this chapter, that is solutions in closed form are given for a number of important flow parameters which determine the performance of (two-dimensional) radial-flow impellers with equiangular blades. The results given provide an extension to formulae commonly applied at the preliminary design stage in the engineering of radial turbomachinery, such formulae being largely based on the application of one-dimensional Eulerian flow theory. Furthermore, the presented solutions can serve as a practical and meaningful reference for numerical methods used for complex, two- and quasi-three-dimensional, potential flow calculations (see for instance Badie 1993 and van Essen 1995).

1.2 Formulation

A single-stage turbomachine, or one stage of a multistage turbomachine, may be considered to be composed of three main parts: a stationary inlet or guidance system, the runner or impeller, and an outlet or collecting device. Since the impeller is responsible for the energy transfer, it seems clear that this component should be our first item of interest. Thus confining our attention to the flow field in isolated impellers, it would be highly desirable to be able to predict the developed head or the delivered work, and to determine the fluid velocity and the pressure distribution along the blades. This, however, is in general not feasible due to the behaviour of real fluids, and the complex geometries of impellers found in practice. Therefore the flow problem has to be simplified, leaving the essentials intact, so that practical solutions can be obtained.

The first assumption is that the fluid may be considered incompressible when dealing with pumps, fans, and hydraulic turbines. Secondly, the importance of the viscous forces compared to the non-viscous (inertia) forces acting on the fluid will be very small, so that the bulk of the fluid may be considered inviscid. The third assumption, usually implicitly made, is that the flow enters the impeller free from vorticity, so that the flow field may be characterised mathematically as irrotational and solenoidal taking into account the former two assumptions. The last assumption is that the flow field may be considered two-dimensional, that is the flow is restricted to depend on radial and angular coordinates only. This is a reasonable assumption for numerous radial-flow turbomachines having a

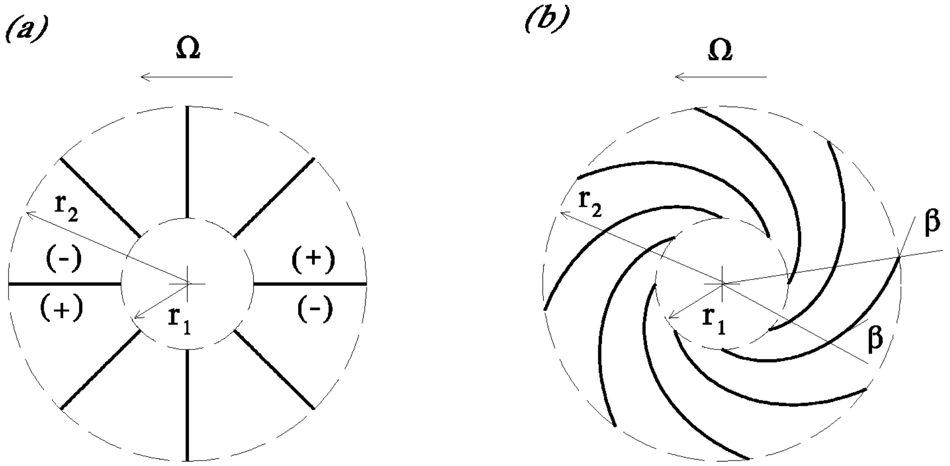

FIGURE 1.1. Two-dimensional radial-flow impellers. (a) straight radial blades ($\beta = 0$); (b) logarithmic spiral blades with $\beta = \frac{1}{3}\pi$.

low specific speed (see for instance Pfleiderer 1991).

The above-mentioned assumptions make it possible to use two-dimensional methods of potential flow theory, in particular the theory of functions of a complex variable, to compute the flow in radial-flow impellers. We additionally adopt equiangular blades, that is blades having a constant angle between radius and tangent. These blades are not only mathematically convenient, but also highly representative since most blade designs in practice are closely represented by equiangular blades. Furthermore, the analysis will be restricted to thin blades, that is blades with zero thickness.

So, in brief, the impellers considered are isolated, two-dimensional, of the radial-flow type, and consist of a finite number of negligibly thin, equally spaced, equiangular blades. The coinciding upper (+) and lower (−) blade surfaces of such impellers (see figure 1.1) are characterised mathematically by

$$r\frac{\mathrm{d}\phi}{\mathrm{d}r} = \tan(\beta) = \text{constant} \tag{1.1}$$

where r is radial distance and ϕ is polar angle. The blade angle β is constant for all radii and is taken counterclockwise positive (where $0 < \beta < \frac{1}{2}\pi$). The direction of revolution of the impeller, rotating with angular speed Ω, can be either clockwise (i.e. $\Omega < 0$) or counterclockwise (i.e. $\Omega > 0$), representing backward or forward curvature respectively.

Integration of (1.1) yields that equiangularly bladed impellers are described by e.g.

$$[\phi(r)]_j = \phi_{o1} + 2\pi\frac{j-1}{n} + \tan(\beta)\ln\left(\frac{r}{r_2}\right) \tag{1.2}$$

or

$$[r(\phi)]_j = r_2 \mathrm{e}^{-2\pi(j-1)/(n\tan(\beta))}\mathrm{e}^{(\phi-\phi_{o1})/\tan(\beta)} \tag{1.3}$$

in which n is the number of blades, j is a blade index $\{j \in I\!N | 1 \leq j \leq n\}$, ϕ_{o1} is an offset angle, in fact $\phi_{o1} = [\phi(r_2)]_{j=1}$, r_2 is the outer tip radius, and $r_1 \leq r \leq r_2$ where r_1 is the inner tip radius.

For $\beta \neq 0$ we generally speak of logarithmic spiral blades (see figure 1.1b), whereas straight radial blades are characterised by a blade angle equal to zero. Putting $\beta = 0$ in

(1.2) we readily obtain that straight radial blades are described by

$$[\phi]_j = \phi_{o1} + 2\pi \frac{j-1}{n} \tag{1.4}$$

Next, for the flow field in the impeller, which is considered two-dimensional, solenoidal, and irrotational *with respect to the non-rotating frame of reference* (!), a velocity potential φ and a stream function ψ can be defined, as is customary in general fluid dynamics, see for instance Batchelor (1967) or Lamb (1932). The complex potential ($\varphi + \mathrm{i}\psi$) associated with this flow will be denoted by $f(z)$, and, hence

$$\frac{\mathrm{d}f}{\mathrm{d}z} = v_x - \mathrm{i}v_y \tag{1.5}$$

where v_x and v_y are the (absolute) velocity components in the x- and y-directions respectively, and $z = x + \mathrm{i}y$, with x and y referring to non-rotating Cartesian (x,y)-coordinates. Furthermore, for convenience in algebraic manipulation, we will distinguish the following potentials:

(*a*) A potential f_Ω due to the rotation of the impeller. This flow will be referred to as displacement flow.

(*b*) A potential f_Q representing the volume flow rate through the impeller, which is incorporated by a source placed at the centre of the impeller; for turbines the source will have a negative strength.

(*c*) A potential f_Γ related to a rectilinear vortex placed at the centre of the impeller. This vortex represents either a prerotation or prewhirl by which we can impose shockless entry for pump impellers, or merely the circulation of the flow leaving turbine impellers.

(*d*) A potential f_K for the imposition of the Kutta condition (known also as Zhukovski's hypothesis). This condition, being set by the effect of viscosity, expresses the physical fact that there is a smooth flow off both surfaces of the impeller blades at the trailing edge.

1.3 Method of solution

To solve the flow field, in particular the fluid velocity along the blades, we will employ a conformal transformation which maps the impeller on the unit circle. In the resulting image or circle plane we can easily determine the previously mentioned sub-flows, by using the theory of functions of a complex variable.

The mapping function that will be employed is originally credited to König (1922), and originates from the transformation of a plane source–vortex flow to a source–vortex flow in a circle plane, see also Acosta (1954), Betz (1964, pp. 245-255), or Busemann (1928). Denoting the physical plane by z and the image plane by ζ and placing the centre of the impeller at the origin in $z = 0$, we can state the transformation $\zeta : z \to \zeta$, which maps the impeller conformally on the unit circle, as

$$\left(\frac{z}{z_2}\right)^n = \left(\frac{\zeta - \zeta_0}{\zeta_2 - \zeta_0}\right) \left(\frac{\dfrac{1}{\zeta} - \bar{\zeta}_0}{\dfrac{1}{\zeta_2} - \bar{\zeta}_0}\right)^{\mathrm{e}^{2\mathrm{i}\beta}} \tag{1.6}$$

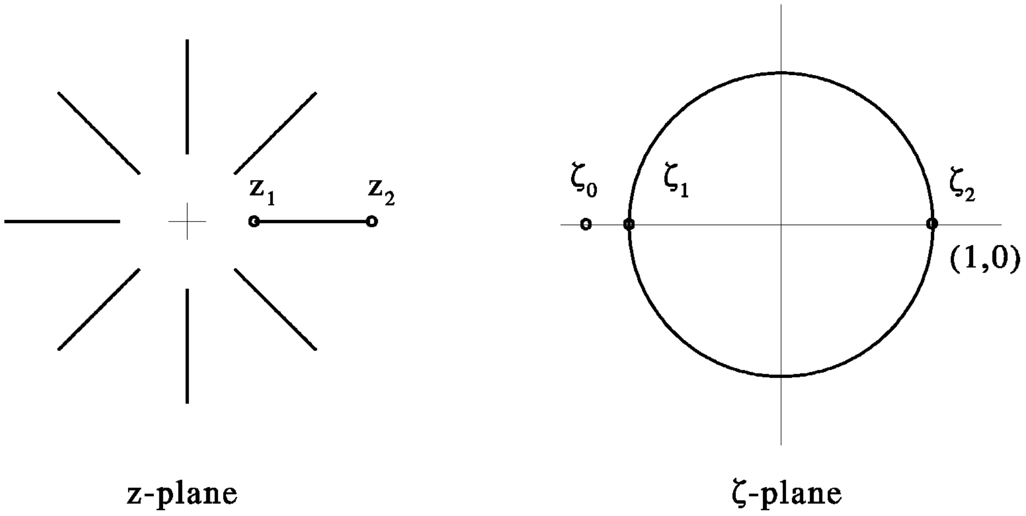

FIGURE 1.2. Mapping of eight straight radial blades.

in which $\zeta_0 = \zeta(0)$ and $\zeta_2 = \zeta(z_2)$, with z_2 being the complex representation of the outer blade tip in the physical plane, and where the overbar denotes the complex conjugate.

An alternative transformation which maps the impeller on the unit circle is due to Schulz (1928*a*,*b*). Schulz' transformation, employed also by Uchimaru & Kito (1931), may be written as

$$\left(\frac{z}{z_2}\right)^n = \left(\frac{\zeta-\zeta_0}{\zeta_2-\zeta_0}\,\frac{\dfrac{1}{\zeta}-\bar{\zeta}_0}{\dfrac{1}{\zeta_2}-\bar{\zeta}_0}\right)^{\mathrm{e}^{\mathrm{i}\beta}/\cos(\beta)} \tag{1.7}$$

This transformation partially resembles transformation (1.6) and, moreover, is relatively simple. Unfortunately, transformation (1.7) violates the conservation of flux and circulation, and therefore it is unsuited for solving the irrotational and solenoidal flow field; the physical nature of sources and vortices is affected illegally by transformation (1.7), that is sources and vortices are both transformed in vortex-sources. In fact, this is a rather logical consequence of Schulz' approach, because Schulz transforms a plane vortex-source to a source flow in the circle plane. Transformation (1.6) is therefore the proper one to use.

Mapping the impeller according to transformation (1.6) we still have a degree of freedom left, namely the exact location of the image ζ_0 of the origin ($z = 0$) of the physical plane. This image ζ_0 may either be taken freely, or it may be derived from a chosen image ζ_2. The latter will be done (separately) for both straight radial blades and logarithmic spiral blades.

1.3.1 *Mapping function for straight radial blades (figure* 1.2*)*

Putting $\beta = 0$, choosing the image of the outer blade tip in $\zeta_2 = 1$, and employing the fact that the blade tips are branch points of the transformation, which implies $|\mathrm{d}z/\mathrm{d}\zeta|_{\zeta_1,\zeta_2} = 0$, it follows from (1.6) that the inner blade tip is mapped in $\zeta_1 = -1$, and that the image of the origin ($z = 0$) lies somewhere on the negative real axis, say $\zeta_0 = -a$ with $a \in \mathbb{R}^+$, see also Betz (1964, pp. 123-131) or Spannhake (1925*a*, 1930). The mapping function (1.6)

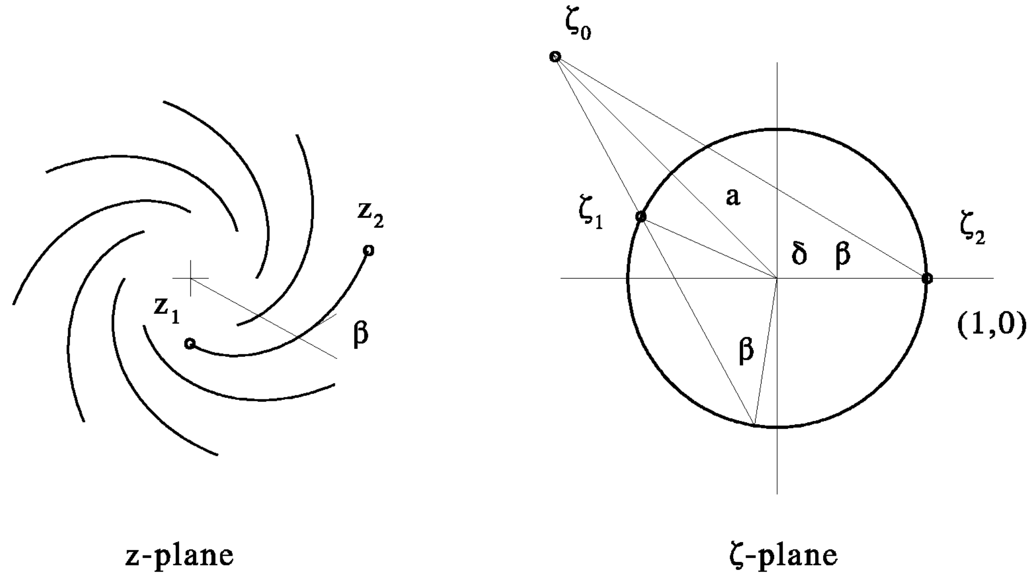

FIGURE 1.3. Mapping of eight logarithmic spiral blades with $\beta = \frac{1}{3}\pi$.

then becomes

$$\left(\frac{z}{z_2}\right)^n = \frac{(a+\zeta)(a+1/\zeta)}{(1+a)^2} \tag{1.8}$$

Next, defining the equivalent space–chord ratio

$$\mu = (r_1/r_2)^n \tag{1.9}$$

for straight radial blades, and taking into account that the physical plane is mapped outside the unit circle, so that $a > 1$, it follows that

$$a = (1+\mu^{\frac{1}{2}})/(1-\mu^{\frac{1}{2}}) \tag{1.10}$$

Then, for points on a blade, i.e. $\zeta = \mathrm{e}^{\mathrm{i}\theta}$ and $z = z(r) = r\mathrm{e}^{\mathrm{i}[\phi(r)]_j}$, the mapping function (1.8) becomes

$$\{R(\theta)\}^n = \frac{1+\mu}{2}\left(1 + \frac{1-\mu}{1+\mu}\cos(\theta)\right) \tag{1.11}$$

where we have introduced a dimensionless radius

$$R(\theta) = r(\theta)/r_2 \tag{1.12}$$

which will be used frequently henceforth.

1.3.2 *Mapping function for logarithmic spiral blades (figure* 1.3*)*

Putting $\zeta_0 = a\mathrm{e}^{\mathrm{i}\delta}$ in transformation (1.6), choosing again $\zeta_2 = 1$, and employing once more the fact that the blade tips are branch points of the transformation, it follows that, see also Acosta (1954) or Busemann (1928),

$$a = \sin(\beta)/\sin(\delta+\beta) \tag{1.13}$$

and that the argument (δ) of ζ_0 is given implicitly by

$$\mu_\beta = \left(-\frac{\sin(2\beta+\delta)}{\sin(\delta)}\right)^{2\cos(\beta)} \mathrm{e}^{-4(\pi-\beta-\delta)\sin(\beta)} \tag{1.14}$$

with

$$\mu_\beta = \mu^{1/\cos(\beta)} = (r_1/r_2)^{n/\cos(\beta)} \tag{1.15}$$

being the equivalent space–chord ratio for logarithmic spiral blades.

The mapping constants a and δ, as given by (1.13) and (1.14), are rather awkward to compute because of the implicit formulation. However, since $\mu_\beta \ll 1$ for most impellers found in practice (e.g. $r_1 = 37$ mm, $r_2 = 100$ mm, $\beta = \frac{1}{3}\pi$ and $n = 8$ blades gives $\mu_\beta \approx 1.2 \times 10^{-7}$) we may employ a simple *asymptotic* approximation. Physically, this approximation embodies a high blade length to (equivalent) blade pitch ratio (i.e. high solidity).

From (1.14) it follows that $\delta \sim \pi - 2\beta$ as $\mu_\beta \to 0$, taking into account that $a \geq 1$ in (1.13). Hence we put

$$\delta = \pi - 2\beta + \varepsilon \tag{1.16}$$

in which $\varepsilon \sim 0$ as $\mu_\beta \to 0$. Then substituting (1.16) in (1.13) and (1.14) we obtain

$$a \sim 1 + \varepsilon \mathrm{cotan}(\beta) \tag{1.17}$$

where

$$\varepsilon \sim (\mu_\beta)^{1/(2\cos(\beta))} \sin(2\beta) \mathrm{e}^{2\beta\tan(\beta)} \tag{1.18}$$

as $\mu_\beta \to 0$.

Equations (1.16), (1.17), and (1.18) provide a simple algorithm to compute the mapping constants, a and δ, asymptotically as $\mu_\beta \to 0$.

Lastly, as a special and highly representative case, the limiting value $\mu_\beta \to 0$ will be considered; here we will confine ourselves to the mapping of points located on a blade, which are represented by (1.2) or (1.3). For these points transformation (1.6) may be stated alternatively as, see also Busemann (1928),

$$\{R(\theta)\}^{n/\cos(\beta)} = \omega\bar{\omega} = |\omega|^2 \tag{1.19}$$

in which

$$\omega = \omega(\theta) = \left(\frac{\zeta - \zeta_0}{1 - \zeta_0}\right)^{\mathrm{e}^{-\mathrm{i}\beta}} = \left(\frac{\mathrm{e}^{\mathrm{i}\theta} - a\mathrm{e}^{\mathrm{i}\delta}}{1 - a\mathrm{e}^{\mathrm{i}\delta}}\right)^{\mathrm{e}^{-\mathrm{i}\beta}} \tag{1.20}$$

Then, with $a \sim 1$ and $\delta \sim \pi - 2\beta$ as $\mu_\beta \to 0$ mapping function (1.19) becomes

$$R(\theta) \sim \left(\frac{\cos(\beta + \frac{1}{2}\theta)}{\cos(\beta)}\right)^{2\cos^2(\beta)/n} \mathrm{e}^{\frac{1}{2}\theta\sin(2\beta)/n} \tag{1.21}$$

as $\mu_\beta \to 0$, which is valid for $-\pi - 2\beta \leq \theta \leq \pi - 2\beta$ and $0 \leq \beta \leq \frac{1}{2}\pi$. Equation (1.21), like (1.11) being appropriate for straight radial blades, formulates the mapping of points located on logarithmic spiral blades explicitly. Consequently, it is possible to obtain solutions in closed form for the flow problem considered. In particular, the fluid velocity along impeller blades can be solved elegantly in closed form.

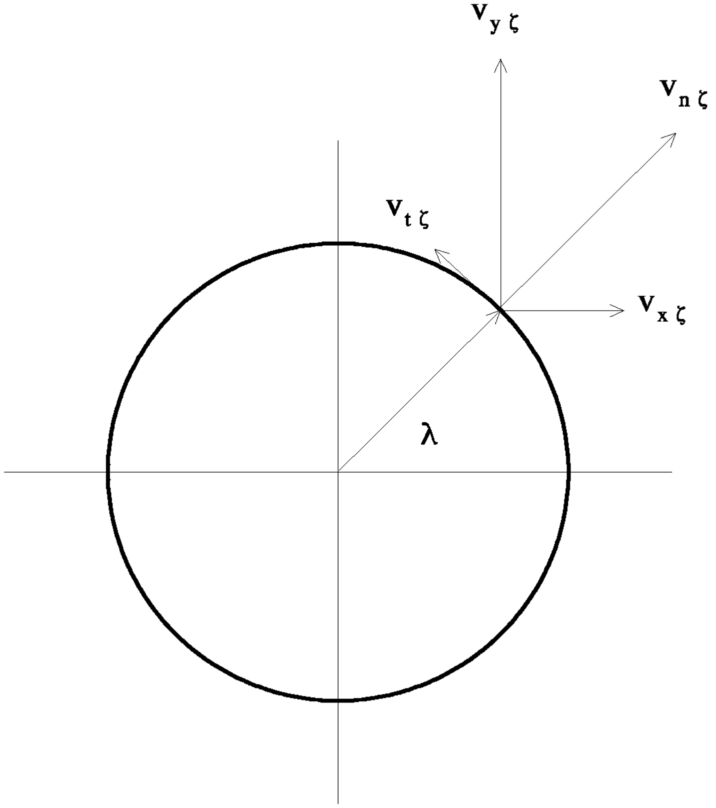

FIGURE 1.4. Fluid velocities along the unit circle in the circle plane.

1.4 Flow along the blades

We now turn to the description of the tangential flow along the blades; that is, for each of the sub-flows that we mentioned before, the contribution to the tangential velocity will be derived from the corresponding description in the circle plane or ζ-plane. This tangential flow along the blades is of particular interest, since important impeller characteristics, such as developed head (§ 1.7) and delivered work (§ 1.8), can be obtained directly from it. (N.B. a full description, with the aid of solutions in closed form, of the complete flow between the blades is most unlikely to be found because of its complexity.)

1.4.1 *Displacement flow*

With reference to figure 1.4 it follows that the fluid velocity tangential at the blades, due to the displacement flow, is given by Poisson's (principal value) integral, see for instance Betz (1964, p. 167) or Moretti (1964, pp. 280-281)

$$v_{t\zeta}^{\Omega}(\theta) = \frac{1}{2\pi}\int_{\delta-2\pi}^{\delta} v_{n\zeta}^{\Omega}(\lambda)\mathrm{cotan}(\tfrac{1}{2}\theta - \tfrac{1}{2}\lambda)\mathrm{d}\lambda \tag{1.22}$$

in which the subscripts n and t denote the normal and tangential parts respectively, and where ζ refers to the ζ-plane; the subscript Ω is added to denote the displacement flow.

The normal velocity $v_{n\zeta}^{\Omega}$ in (1.22) follows from the transformation

$$v_{n\zeta}^{\Omega} = v_{nz}^{\Omega}\left|\frac{\mathrm{d}z}{\mathrm{d}\zeta}\right| \tag{1.23}$$

in which the normal velocity v_{nz}^{Ω} is prescribed by the physical fact that, at the blades, the relative fluid velocity normal to the blades equals zero. By this boundary condition it follows that

$$v_{nz}^{\Omega} = (\boldsymbol{\Omega} \times \boldsymbol{r}) \cdot \boldsymbol{n} \tag{1.24}$$

where $\boldsymbol{\Omega}$ is the angular speed of the impeller, $\boldsymbol{r}$ is the position vector for blade-located points, and $\boldsymbol{n}$ is the unit normal of the blade(s). In two dimensions and for equiangular blades (1.24) yields

$$v_{nz}^{\Omega} = (\pm)\, \Omega r \cos(\beta) \tag{1.25}$$

in which $\Omega = |\boldsymbol{\Omega}|$, $r = |\boldsymbol{r}|$, and where the sign $(\pm)$ depends on the side of the blade, that is, $(+)$ for upper and $(-)$ for lower blades surfaces, due to the changing of $\boldsymbol{n}$.

By some geometrical manipulations it further follows that the derivative of the mapping for points located on equiangular blades may be written as

$$\left|\frac{\mathrm{d}z}{\mathrm{d}\zeta}\right| = (\mp)\, \frac{1}{\cos(\beta)} \frac{\mathrm{d}r}{\mathrm{d}\theta} \tag{1.26}$$

the sign $(\mp)$ again depending on the side of the blade. Substituting this result and (1.25) in (1.23) we get, employing the dimensionless radius $R(\theta) = r(\theta)/r_2$,

$$v_{n\zeta}^{\Omega}(\theta) = -\Omega r_2^2 R(\theta) \frac{\mathrm{d}R}{\mathrm{d}\theta} \tag{1.27}$$

Then, substituting (1.27) in (1.22) we obtain that the fluid velocity along the unit circle, due to the revolution of the impeller, is given by

$$v_{t\zeta}^{\Omega}(\theta) = -\frac{\Omega r_2^2}{2\pi} \int_{\delta-2\pi}^{\delta} R(\lambda) \frac{\mathrm{d}R}{\mathrm{d}\lambda} \mathrm{cotan}(\tfrac{1}{2}\theta - \tfrac{1}{2}\lambda) \mathrm{d}\lambda \tag{1.28}$$

The transformation

$$v_{tz} = v_{t\zeta} \frac{\cos(\beta)}{r_2} \left|\frac{\mathrm{d}R}{\mathrm{d}\theta}\right|^{-1} \tag{1.29}$$

then gives the corresponding (tangential) fluid velocity in the physical plane.

1.4.2 *Source flow*

Placing a fluid source of strength Q/n in the ζ-plane at $\zeta = \zeta_0$, which corresponds with a fluid source of strength Q located at the centre of the z-plane, yields the potential

$$f_Q(\zeta) = \frac{Q}{2\pi n} \ln(\zeta - \zeta_0) \tag{1.30}$$

Then, by applying the circle theorem of Milne-Thomson (1958), we impose the boundary condition that the unit circle has to be a streamline, and thus obtain from (1.30)

$$f_Q^*(\zeta) = \frac{Q}{2\pi n} \left(\ln(\zeta - \zeta_0) + \ln\left(\frac{1}{\zeta} - \bar{\zeta}_0\right) \right) \tag{1.31}$$

where the asterisk is added for clarity. Next taking the derivative of (1.31) with respect to ζ, substituting $\zeta = \mathrm{e}^{\mathrm{i}\theta}$, and $\zeta_0 = a\mathrm{e}^{\mathrm{i}\delta}$, and using the identity

$$v_{x\zeta}(\theta) - \mathrm{i}v_{y\zeta}(\theta) = \mathrm{e}^{-\mathrm{i}\theta}\left(v_{n\zeta}(\theta) - \mathrm{i}v_{t\zeta}(\theta)\right) \tag{1.32}$$

we get the normal and tangential parts of the fluid velocity along the unit circle due to the source, i.e.

$$v^Q_{n\zeta}(\theta) = 0 \tag{1.33}$$

$$v^Q_{t\zeta}(\theta) = \frac{Q}{\pi n}\,\frac{a\sin(\theta-\delta)}{1+a^2-2a\cos(\theta-\delta)} \tag{1.34}$$

Equation (1.33) confirms that the boundary condition is imposed properly. The tangential velocity (v^Q_{tz}) in the physical plane again follows from transformation (1.29).

1.4.3 *Vortex flow*

Placing a rectilinear vortex of strength Γ_1/n in the ζ-plane at $\zeta = \zeta_0$ yields the potential

$$f_\Gamma(\zeta) = \frac{\Gamma_1}{2\pi \mathrm{i} n}\ln(\zeta - \zeta_0) \tag{1.35}$$

Applying the circle theorem, (1.35) gives

$$f^*_\Gamma(\zeta) = \frac{\Gamma_1}{2\pi \mathrm{i} n}\left(\ln(\zeta-\zeta_0) - \ln\left(\frac{1}{\zeta} - \bar{\zeta}_0\right)\right) \tag{1.36}$$

Then taking the derivative of (1.36) with respect to ζ, substituting $\zeta = \mathrm{e}^{\mathrm{i}\theta}$ and $\zeta_0 = a\mathrm{e}^{\mathrm{i}\delta}$, and using identity (1.32) we find that the normal and tangential parts of the fluid velocity along the unit circle due to the vortex are given by

$$v^\Gamma_{n\zeta}(\theta) = 0 \tag{1.37}$$

$$v^\Gamma_{t\zeta}(\theta) = \frac{\Gamma_1}{\pi n}\,\frac{1-a\cos(\theta-\delta)}{1+a^2-2a\cos(\theta-\delta)} \tag{1.38}$$

Once more it is seen that the boundary condition is imposed properly. The tangential fluid velocity (v^Γ_{tz}) in the physical plane again follows from transformation (1.29).

1.4.4 *Kutta condition or Zhukovski's hypothesis*

The last sub-flow to be discussed is related to the Kutta condition, also known as Zhukovski's hypothesis, which implies the elimination of the singular behaviour of the fluid velocity at the trailing edge of a blade. This is done by superposing a rectilinear vortex of strength Γ_b at the origin of the ζ-plane. This additional flow satisfies both the potential equation and the boundary condition that the unit circle is a streamline; the potential reads

$$f_K(\zeta) = \frac{\Gamma_b}{2\pi}\ln(\zeta) \tag{1.39}$$

in which $\mathit{\Gamma}_b$ represents the blade circulation, which is (to be) determined by the Kutta condition, and where K refers to the Kutta condition.

Taking the derivative of (1.39) with respect to ζ, substituting $\zeta = \mathrm{e}^{\mathrm{i}\theta}$, and using identity (1.32), gives the normal and tangential parts of the fluid velocity along the unit circle due to the additional vortex $\mathit{\Gamma}_b$, i.e.

$$v_{n\zeta}^{K}(\theta) = 0 \tag{1.40}$$

$$v_{t\zeta}^{K}(\theta) = \mathit{\Gamma}_b/2\pi \tag{1.41}$$

Now by simply requiring a zero (overall) fluid velocity at the trailing edge in the ζ-plane we impose the Kutta condition. This method will be valid if the decrease of the fluid velocity exceeds the increase of the derivative $(\mathrm{d}\zeta/\mathrm{d}z)$ of the mapping near the trailing edge.

When imposing the Kutta condition we have to distinguish pumps from (radial inward-flow) turbines because the trailing edges of radial pump impellers lie at the outer radius whereas inward-flow radial turbine impellers have trailing edges at the inner radius.

Imposing the Kutta condition at the outer tip (i.e. $\theta = 0$) yields the relation

$$v_{t\zeta}^{\mathit{\Omega}}(0) + v_{t\zeta}^{Q}(0) + v_{t\zeta}^{\mathit{\Gamma}}(0) + v_{t\zeta}^{K} = 0 \tag{1.42}$$

Substituting (1.41) in (1.42) we obtain that the blade circulation for *pump* impellers ($\mathit{\Gamma}_{bp}$) is given by

$$\mathit{\Gamma}_{bp} = -2\pi\left(v_{t\zeta}^{\mathit{\Omega}}(0) + v_{t\zeta}^{Q}(0) + v_{t\zeta}^{\mathit{\Gamma}}(0)\right) \tag{1.43}$$

Imposing the Kutta condition at the inner tip ($\theta = \theta_1$) we analogously obtain for the blade circulation ($\mathit{\Gamma}_{bt}$) of *turbine* impellers

$$\mathit{\Gamma}_{bt} = -2\pi\left(v_{t\zeta}^{\mathit{\Omega}}(\theta_1) + v_{t\zeta}^{Q}(\theta_1) + v_{t\zeta}^{\mathit{\Gamma}}(\theta_1)\right) \tag{1.44}$$

It should be recognised that when turbines are considered, the inner circulation $\mathit{\Gamma}_1$ is not prescribed, as it is for pumps, but instead the outer circulation $\mathit{\Gamma}_2$ is dictated. Both circulations are simply related by

$$\mathit{\Gamma}_2 = \mathit{\Gamma}_1 + \sum_{j=1}^{n} \mathit{\Gamma}_b^j \tag{1.45}$$

where we have omitted the subscripts p (for pump) and t (for turbine) since (1.45) is universally valid. Alternatively, recalling that we are dealing with isolated impellers having blade-to-blade-equivalent blade circulations due to the periodicity of the flow, (1.45) may also be stated as

$$\mathit{\Gamma}_2 = \mathit{\Gamma}_1 + n\mathit{\Gamma}_b \tag{1.46}$$

1.4.5 *Condition of shockless entry*

After imposing the Kutta condition still another singularity remains, namely the one at the leading edge of the blades. Analogous to the imposition of the Kutta condition this singularity can be eliminated; in this case either by a proper choice of a prerotation or by correctly selecting the point of operation. This is generally known as (imposing) the condition of shockless entry. This condition is strictly an operating condition, whereas the Kutta condition is a physical fact. From a mathematical point of view, however, both conditions are alike.

When imposing the condition of shockless entry a distinction has again to be made between radial pump impellers and inward-flow radial turbine impellers because of the transposition of the leading edge.

For pump impellers, i.e. the inner tip ($\theta = \theta_1$) as leading edge, the condition of shockless entry yields the relation

$$v_{t\zeta}^{\Omega}(\theta_1) + v_{t\zeta}^{Q}(\theta_1) + v_{t\zeta}^{\Gamma}(\theta_1) + v_{t\zeta}^{K} = 0 \tag{1.47}$$

Substituting (1.41) in (1.47) and using (1.43) then gives

$$v_{t\zeta}^{\Omega}(\theta_1) - v_{t\zeta}^{\Omega}(0) + v_{t\zeta}^{Q}(\theta_1) - v_{t\zeta}^{Q}(0) + v_{t\zeta}^{\Gamma}(\theta_1) - v_{t\zeta}^{\Gamma}(0) = 0 \tag{1.48}$$

Equation (1.48) fully determines the (required) prerotation or prewhirl Γ_{1s} of the flow entering pump impellers, or the point of operation to be taken, so that shockless entry is obtained.

For turbine impellers, i.e. the outer tip ($\theta = 0$) as leading edge, the condition of shockless entry yields the relation

$$v_{t\zeta}^{\Omega}(0) + v_{t\zeta}^{Q}(0) + v_{t\zeta}^{\Gamma}(0) + v_{t\zeta}^{K} = 0 \tag{1.49}$$

Substituting (1.41) in (1.49), and using (1.44) we obtain (1.48) again. From this equation we indirectly determine the shockless prerotation Γ_{2s} for turbine impellers. First Γ_1 is solved and thereupon the prerotation Γ_{2s} is obtained using (1.45).

1.5 Solutions in closed form for radially bladed pump and turbine impellers

In this section our attention will be confined to the case of straight radial blades. Solutions in closed form for both pump and turbine impellers will be presented, having outlined the universal solutions first.

Putting $\beta = 0$, $\delta = \pi$, and using (1.10) and (1.11) we obtain from (1.28), (1.34), and (1.38)

$$v_{t\zeta}^{\Omega}(\theta) = \frac{K}{2\pi n}\int_{-\pi}^{\pi}\left(1 + \frac{1-\mu}{1+\mu}\cos(\lambda)\right)^{-1+2/n}\sin(\lambda)\mathrm{cotan}(\tfrac{1}{2}\theta - \tfrac{1}{2}\lambda)\mathrm{d}\lambda \tag{1.50}$$

$$v_{t\zeta}^{Q}(\theta) = -\frac{Q}{2\pi n}\,\frac{\sin(\theta)}{\cos(\theta) + (1+\mu)/(1-\mu)} \tag{1.51}$$

$$v_{t\zeta}^{\Gamma}(\theta) = \frac{\Gamma_1}{2\pi n}\,\frac{\cos(\theta) + (1-\mu^{\frac{1}{2}})/(1+\mu^{\frac{1}{2}})}{\cos(\theta) + (1+\mu)/(1-\mu)} \tag{1.52}$$

in which

$$K = \frac{1-\mu}{1+\mu}\left(\tfrac{1}{2}(1+\mu)\right)^{2/n}\Omega r_2^2 \tag{1.53}$$

Equations (1.51) and (1.52) are both simple expressions that need no further explanation. Equation (1.50), however, deserves some further attention. (Details of the mathematical manipulations involved can be found in Visser 1991.) First, substituting the trigonometric identity

$$\mathrm{cotan}(\tfrac{1}{2}\theta - \tfrac{1}{2}\lambda) = \frac{\sin(\lambda) + \sin(\theta)}{\cos(\lambda) - \cos(\theta)} \tag{1.54}$$

and taking into account that the trigonometric function

$$\left(1+\frac{1-\mu}{1+\mu}\cos(\lambda)\right)^{-1+2/n}\frac{\sin(\lambda)\sin(\theta)}{\cos(\lambda)-\cos(\theta)} \tag{1.55}$$

is an odd function of λ, we may write (1.50) as

$$v^{\Omega}_{t\zeta}(\theta)=\frac{K}{2\pi n}\fint_{-\pi}^{\pi}\left(1+\frac{1-\mu}{1+\mu}\cos(\lambda)\right)^{-1+2/n}\frac{\sin^2(\lambda)}{\cos(\lambda)-\cos(\theta)}\mathrm{d}\lambda \tag{1.56}$$

Then employing some elementary trigonometric manipulations we can rephrase (1.56) as

$$v^{\Omega}_{t\zeta}(\theta)=\frac{K}{2\pi n}\left(\sin^2(\theta)I(\theta)+(1-\cos(\theta))\,I_1-I_0\right) \tag{1.57}$$

in which

$$I(\theta)=\fint_{-\pi}^{\pi}\left(1+\frac{1-\mu}{1+\mu}\cos(\lambda)\right)^{-1+2/n}\frac{\mathrm{d}\lambda}{\cos(\lambda)-\cos(\theta)} \tag{1.58}$$

$$I_0=\int_{-\pi}^{\pi}\left(1+\frac{1-\mu}{1+\mu}\cos(\lambda)\right)^{-1+2/n}(1+\cos(\lambda))\,\mathrm{d}\lambda \tag{1.59}$$

$$I_1=\int_{-\pi}^{\pi}\left(1+\frac{1-\mu}{1+\mu}\cos(\lambda)\right)^{-1+2/n}\mathrm{d}\lambda \tag{1.60}$$

Equation (1.57) is a mathematically convenient simplification, as will be demonstrated shortly hereafter. The integrals I_0 and I_1 can both be expressed elegantly by a rather familiar special function, namely the (Gauss) hypergeometric function or series. The equivalents of the integrals (1.59) and (1.60) read (see also Gradshteyn & Ryzhik 1980, pp. 389, 384)

$$I_0=2\pi\left(\tfrac{1}{2}(1+\mu)\right)^{1-2/n}F\left(\tfrac{1}{2},1-\frac{2}{n};2;1-\mu\right) \tag{1.61}$$

$$I_1=2^{6/n}\pi(1+\mu)^{1-2/n}(1+\mu^{\frac{1}{2}})^{-4/n}(\mu^{\frac{1}{2}})^{-1+4/n}F\left(\frac{2}{n},\frac{2}{n};1;\left(\frac{1-\mu^{\frac{1}{2}}}{1+\mu^{\frac{1}{2}}}\right)^2\right) \tag{1.62}$$

where $F(-)={}_2F_1(-)$ represents the (Gauss) hypergeometric function; see for instance Whittaker & Watson (1927).

To evaluate the integral $I(\theta)$ we expand the leading part of integral (1.58) in a Fourier cosine series. The Fourier expansion reads

$$\left(1+\frac{1-\mu}{1+\mu}\cos(\lambda)\right)^{-1+2/n}=\tfrac{1}{2}A_0+\sum_{k=1}^{\infty}A_k\cos(k\lambda) \tag{1.63}$$

where the coefficients of the series are defined by

$$A_k=\frac{2}{\pi}\int_{0}^{\pi}\left(1+\frac{1-\mu}{1+\mu}\cos(\tau)\right)^{-1+2/n}\cos(k\tau)\mathrm{d}\tau \tag{1.64}$$

Then substituting (1.63) in (1.58), and using the following principal value integral (Milne-Thomson 1958, p. 80) well-known in aerodynamics:

$$\fint_{-\pi}^{\pi} \frac{\cos(k\lambda)}{\cos(\lambda)-\cos(\theta)}\mathrm{d}\lambda = \frac{2\pi}{\sin(\theta)}\sin(k\theta) \tag{1.65}$$

we obtain

$$I(\theta) = \frac{2\pi}{\sin(\theta)}\sum_{k=1}^{\infty} A_k \sin(k\theta) \tag{1.66}$$

Furthermore, the Fourier coefficients (1.64) can be expressed by the hypergeometric function. It follows that (see also Gradshteyn & Ryzhik 1980, p. 384)

$$A_k = 2^{6/n}(1+\mu)^{1-2/n}(1+\mu^{\frac{1}{2}})^{-4/n}(\mu^{\frac{1}{2}})^{-1+4/n}a_k \tag{1.67}$$

where

$$a_k = \frac{1}{k!}\left(\frac{1-\mu^{\frac{1}{2}}}{1+\mu^{\frac{1}{2}}}\right)^{k} F\left(\frac{2}{n}, k+\frac{2}{n}; k+1; \left(\frac{1-\mu^{\frac{1}{2}}}{1+\mu^{\frac{1}{2}}}\right)^{2}\right)\prod_{m=1}^{k}\left(-m+\frac{2}{n}\right) \tag{1.68}$$

From which we notice that

$$\begin{aligned} n=1: &\quad a_1 = -\left(\frac{1-\mu^{\frac{1}{2}}}{1+\mu^{\frac{1}{2}}}\right)\left(1-\left(\frac{1-\mu^{\frac{1}{2}}}{1+\mu^{\frac{1}{2}}}\right)^{2}\right)^{-3}; \quad a_k = 0 \;\forall\; k \geq 2 \\ n=2: &\quad a_k = 0 \end{aligned} \tag{1.69}$$

Finally, substituting (1.61), (1.62) and (1.66) in (1.57), and using (1.67) we obtain

$$\begin{aligned} v^{\Omega}_{t\zeta}(\theta) = {} & -\Omega r_2^2\frac{1-\mu}{2n}F\left(\tfrac{1}{2}, 1-\frac{2}{n}; 2; 1-\mu\right) + \Omega r_1^2\frac{1-\mu}{n\mu^{\frac{1}{2}}}\left(\frac{2}{1+\mu^{\frac{1}{2}}}\right)^{4/n} \\ & \times\left\{\sin(\theta)\sum_{k=1}^{\infty}a_k\sin(k\theta) + \sin^2(\tfrac{1}{2}\theta)F\left(\frac{2}{n}, \frac{2}{n}; 1; \left(\frac{1-\mu^{\frac{1}{2}}}{1+\mu^{\frac{1}{2}}}\right)^{2}\right)\right\} \end{aligned} \tag{1.70}$$

Equation (1.70) gives the solution in closed form for the fluid velocity, tangential at the unit circle in the ζ-plane, due to the rotation of the impeller. Summing the individual contributions (1.51), (1.52), and (1.70) we get the the overall velocity in the ζ-plane. The corresponding velocity in the physical plane is thereupon readily obtained by transformation (1.29), which becomes for straight radial blades (i.e. $\beta = 0$)

$$\frac{v_{tz}}{v_{t\zeta}} = \frac{2n}{(1-\mu)r_2}\frac{\{R(\theta)\}^{n-1}}{|\sin(\theta)|} \tag{1.71}$$

where $R(\theta)$ is given by (1.11).

Computing the fluid velocity according to (1.70) further requires an indication of the (truncation) error of the partial sum of the Fourier series, so that the number of Fourier coefficients necessary for obtaining satisfactory significance can be obtained. This may be done by comparing the truncation error with a geometric series, in the following manner.

First we put

$$S(\theta) = \sum_{k=1}^{\infty} a_k \sin(k\theta) = S_p(\theta) + T_p(\theta) \tag{1.72}$$

where $S_p(\theta)$ is the partial sum and $T_p(\theta)$ is the truncation error, both after summing the first p terms of the series. For the truncation error it then follows that

$$|T_p(\theta)| \leq \sum_{k=p+1}^{\infty} |a_k| \tag{1.73}$$

Next we obtain from (1.68) that

$$|a_k| \leq \left(\frac{1-\mu^{\frac{1}{2}}}{1+\mu^{\frac{1}{2}}}\right)^k \frac{\Gamma(1-4/n)}{\{\Gamma(1-2/n)\}^2} \qquad (n > 4) \tag{1.74}$$

which is easily verified knowing that

$$\left|\prod_{m=1}^{k}\left(-m+\frac{2}{n}\right)\right| = \frac{\Gamma(k+1-2/n)}{\Gamma(1-2/n)} \tag{1.75}$$

and

$$\begin{aligned} 1 \leq F\left(\frac{2}{n}, k+\frac{2}{n}; k+1; \left(\frac{1-\mu^{\frac{1}{2}}}{1+\mu^{\frac{1}{2}}}\right)^2\right) &\leq F\left(\frac{2}{n}, k+\frac{2}{n}; k+1; 1\right) \\ &= \frac{\Gamma(k+1)\Gamma(1-4/n)}{\Gamma(k+1-2/n)\Gamma(1-2/n)} \qquad (n > 4) \end{aligned} \tag{1.76}$$

For the truncation error we then get

$$|T_p(\theta)| < T_p = \frac{\Gamma(1-4/n)}{\{\Gamma(1-2/n)\}^2} \sum_{k=p+1}^{\infty} L^k = \frac{\Gamma(1-4/n)}{\{\Gamma(1-2/n)\}^2} \frac{L^{p+1}}{1-L} \tag{1.77}$$

in which $L = (1-\mu^{\frac{1}{2}})/(1+\mu^{\frac{1}{2}})$, so that

$$S(\theta) = S_p(\theta) \pm \frac{\Gamma(1-4/n)}{\{\Gamma(1-2/n)\}^2} \frac{L^{p+1}}{1-L} \tag{1.78}$$

This way we find that $T_{99} \approx 0.75$, $T_{499} \approx 2 \times 10^{-7}$, and $T_{999} \approx 10^{-15}$ for $n = 8$ blades and $r_1/r_2 = 0.37$. This particular choice of n and r_1/r_2 will be used throughout the next sections to illustrate the respective results.

In conclusion, we note that (d'Alembert's rule)

$$L = \lim_{k\to\infty}\left|\frac{A_{k+1}}{A_k}\right| = \lim_{k\to\infty}\left|\frac{a_{k+1}}{a_k}\right| = \frac{1-\mu^{\frac{1}{2}}}{1+\mu^{\frac{1}{2}}} \tag{1.79}$$

which is always less than 1 ($\mu > 0$), so the Fourier series will converge uniformly. We further notice that the rate of convergence of the series decreases as μ becomes small, that is when $\mu \ll 1$.

1.5.1 *Solutions for pump impellers*

From (1.43), (1.51), (1.52), and (1.70) we readily obtain that the blade circulation for pump impellers equipped with straight radial blades is given by

$$n\mathit{\Gamma}_{bp} = \sigma_{p\mathit{\Omega}} 2\pi \mathit{\Omega} r_2^2 - \sigma_{p\mathit{\Gamma}} \mathit{\Gamma}_1 \tag{1.80}$$

where

$$\sigma_{p\mathit{\Omega}} = \tfrac{1}{2}(1-\mu) F\left(\tfrac{1}{2}, 1-\frac{2}{n}; 2; 1-\mu\right) \tag{1.81}$$

$$\sigma_{p\mathit{\Gamma}} = 1-\mu^{\frac{1}{2}} \tag{1.82}$$

The dimensionless factors $\sigma_{p\mathit{\Omega}}$ and $\sigma_{p\mathit{\Gamma}}$ are generally known as slip factors. The respective subscripts employed, refer to pump impellers (p), displacement flow ($\mathit{\Omega}$) and vortex flow ($\mathit{\Gamma}$). By definition slip factors are always positive and less than 1. They express that the flow is influenced imperfectly due to the finite number of blades; the fluid is said to slip. (The slip itself is quantified by $1-\sigma$.)

Slip factor $\sigma_{p\mathit{\Omega}}$ is commonly mentioned in many text-books or papers on turbomachinery. It represents the rotational slip of the flow due to imperfect guidance of the blades. Slip factor $\sigma_{p\mathit{\Gamma}}$, however, is hardly ever found in the (turbomachinery) literature. It represents the slip of the flow leaving pump impellers due to the prerotation or prewhirl at impeller entrance. Both slip factors as well as the concept of slip will be further discussed in § 1.7.

Next summing (1.41), (1.51), (1.52), and (1.70), and using (1.80), we obtain the overall velocity along the unit circle in the ζ-plane for the pump impeller:

$$\begin{aligned} v_{t\zeta}(\theta) = &-\frac{\sin(\theta)}{\cos(\theta)+(1+\mu)/(1-\mu)}\,\frac{Q}{2\pi n} - \mu^{\frac{1}{2}}\frac{1-\cos(\theta)}{\cos(\theta)+(1+\mu)/(1-\mu)}\,\frac{\mathit{\Gamma}_1}{2\pi n} \\ &+ \mathit{\Omega} r_1^2 \frac{1-\mu}{n\mu^{\frac{1}{2}}}\left(\frac{2}{1+\mu^{\frac{1}{2}}}\right)^{4/n}\left\{\sin(\theta)\sum_{k=1}^{\infty} a_k \sin(k\theta) + \sin^2(\tfrac{1}{2}\theta) F\left(\frac{2}{n}, \frac{2}{n}; 1; \left(\frac{1-\mu^{\frac{1}{2}}}{1+\mu^{\frac{1}{2}}}\right)^2\right)\right\} \end{aligned} \tag{1.83}$$

Then employing transformation (1.71), and using the auxiliary relations (straight radial blades only) $v_{tz}^{+} = -w_r$ and $v_{tz}^{-} = +w_r$, where the superscripts (+) and (−) refer to the upper and lower blade surfaces respectively, we get

$$\begin{aligned} w_{rp} = &\frac{Q}{2\pi r} + \mu^{\frac{1}{2}} \tan(\tfrac{1}{2}\theta)\frac{\mathit{\Gamma}_1}{2\pi r} - \{R(\theta)\}^{n-1}\frac{2\mathit{\Omega} r_1^2}{r_2 \mu^{\frac{1}{2}}}\left(\frac{2}{1+\mu^{\frac{1}{2}}}\right)^{4/n} \\ &\times\left\{\sum_{k=1}^{\infty} a_k \sin(k\theta) + \tfrac{1}{2}\tan(\tfrac{1}{2}\theta) F\left(\frac{2}{n}, \frac{2}{n}; 1; \left(\frac{1-\mu^{\frac{1}{2}}}{1+\mu^{\frac{1}{2}}}\right)^2\right)\right\} \end{aligned} \tag{1.84}$$

in which w_{rp} is the outward-directed, relative, *radial* fluid velocity at the blades of the *pump* impeller, and $r(\theta) = r_2 R(\theta)$ as given by (1.11). For convenience we may further rephrase (1.84) in a dimensionless form as

$$R(\theta)\frac{w_{rp}}{\Omega r_2} = \Phi + \mu^{\frac{1}{2}+2/n}\tan(\tfrac{1}{2}\theta)\Upsilon_1 - 2\left\{R(\theta)\right\}^n \mu^{-\frac{1}{2}+2/n}\left(\frac{2}{1+\mu^{\frac{1}{2}}}\right)^{4/n}$$
$$\times\left\{\sum_{k=1}^{\infty} a_k \sin(k\theta) + \tfrac{1}{2}\tan(\tfrac{1}{2}\theta)F\left(\frac{2}{n},\frac{2}{n};1;\left(\frac{1-\mu^{\frac{1}{2}}}{1+\mu^{\frac{1}{2}}}\right)^2\right)\right\} \tag{1.85}$$

where we have introduced a flow rate coefficient $\Phi = Q/(2\pi\Omega r_2^2)$, and a vortex or prewhirl coefficient $\Upsilon_1 = \Gamma_1/(2\pi\Omega r_1^2)$; both coefficients Φ and Υ_1 may be chosen at will, though the following points should be noted.

Firstly, the flow rate coefficient Φ, i.e. the throughput in proportion to the rotational speed, should be large enough so that the relative fluid velocity along the impeller blades will be strictly positive, that is $w_{rp} \geq 0$. In that case we will not need to take into account the occurrence of reverse flow (i.e. $w_{rp} < 0$), which may have a negative influence on the performance of pump impellers.

Secondly, the vortex coefficient Υ_1 should preferably be chosen such that a shockless entry is obtained, so that impact losses are reduced to a minimum. From (1.48), (1.51), (1.52), and (1.70), putting $\theta_1 = \pi$, it follows that the prewhirl (Γ_{1s}) required to obtain shockless entry equals

$$\Gamma_{1s} = \tau_p 2\pi\Omega r_1^2 \tag{1.86}$$

or, in dimensionless form,

$$\Upsilon_{1s} = \tau_p \tag{1.87}$$

where we have introduced the prerotation factor τ_p for *pump* impellers, which reads (for straight radial blades)

$$\tau_p = \left(\frac{2}{1+\mu^{\frac{1}{2}}}\right)^{4/n} F\left(\frac{2}{n},\frac{2}{n};1;\left(\frac{1-\mu^{\frac{1}{2}}}{1+\mu^{\frac{1}{2}}}\right)^2\right) \tag{1.88}$$

Like the slip factor the prerotation factor is also dimensionless, but larger than 1.

Both the flow rate coefficient minimally required to avoid reverse flow, and the prerotation (factor) required for shockless entry will be discussed in greater detail in § 1.7.

To illustrate (1.85) we have plotted in figure 1.5 the dimensionless fluid velocity $w_{rp}/(\Omega r_2)$ for zero and minimum (i.e. $\Phi = \Phi_m$) throughput, both with zero prerotation and shockless entry, for pump impellers with eight straight radial blades and inlet-to-outlet radius ratio $r_1/r_2 = 0.37$. For convenience we here have introduced a dimensionless blade coordinate $s \in [0,1]$, defined by $s = (r - r_1)/(r_2 - r_1) = (R(\theta) - r_1/r_2)/(1 - r_1/r_2)$. The Fourier series in (1.85) has been evaluated for this particular case by summing a thousand terms.

Furthermore, we have plotted in figure 1.6 the asymptotic solution for the displacement flow velocity along straight radial blades as $\mu \to 0$. This solution, i.e. the asymptotic expansion of (1.85), reads

$$R(\theta)\frac{w_{rp}}{\Omega r_2} \sim \Phi - 2^{1-4/n}\Gamma\left(1+\frac{4}{n}\right)\sum_{k=1}^{\infty}\frac{\sin(k\theta)}{\Gamma(1+k+2/n)\Gamma(1-k+2/n)} \tag{1.89}$$

as $\mu \to 0$, in which $\Gamma(-)$ represents the well-known (complete) gamma function, and where $R(\theta) \sim \cos^{2/n}(\tfrac{1}{2}\theta)$ as $\mu \to 0$.

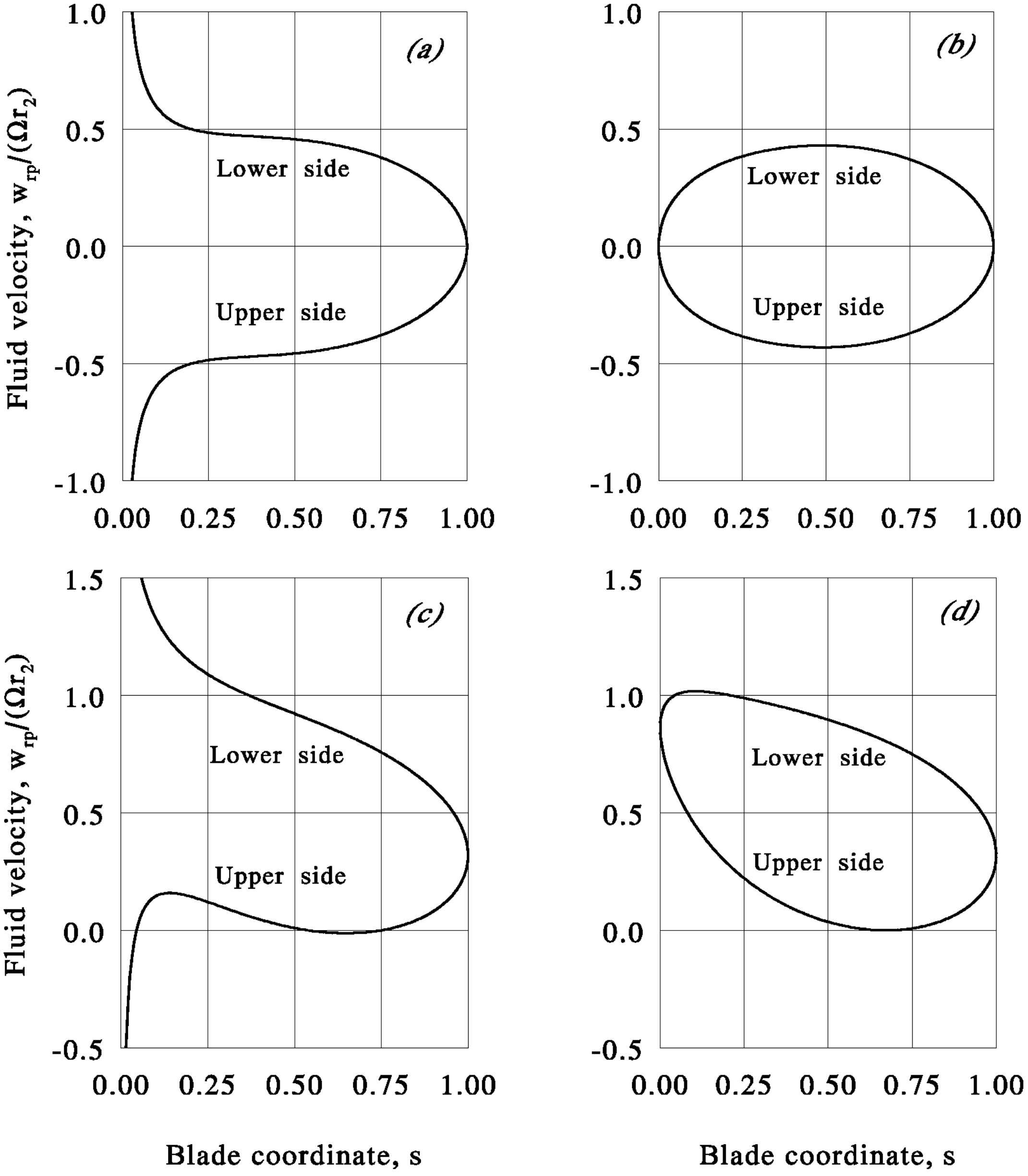

FIGURE 1.5. Exact solution of fluid velocities along straight radial blades of eight-bladed pump impellers with inlet-to-outlet radius ratio of 0.37. (*a*) Zero volume flow rate and zero prerotation; (*b*) zero volume flow rate and shockless entry; (*c*) minimum volume flow rate and zero prerotation; (*d*) minimum volume flow rate shockless entry ($\Phi_m = 0.319$; $\Upsilon_{1s} = 0.214$).

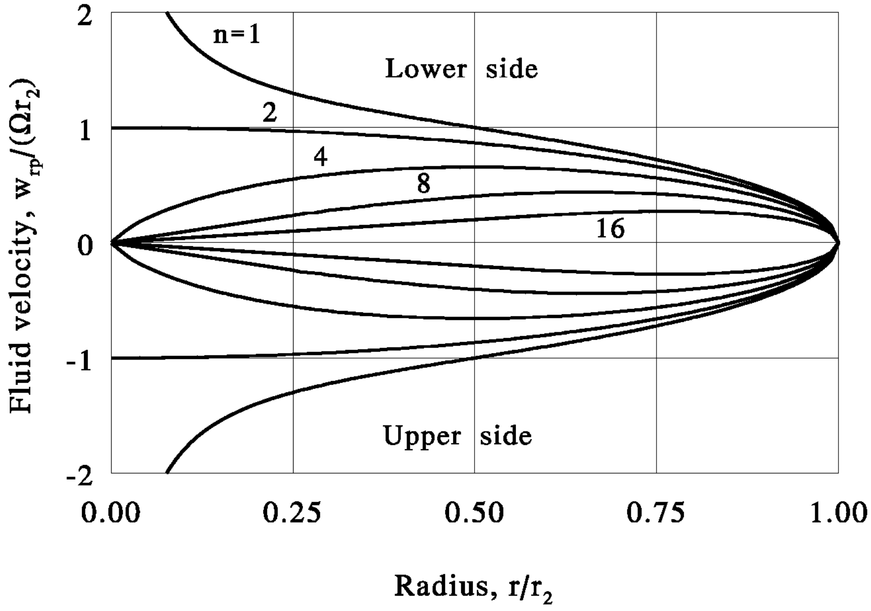

FIGURE 1.6. Displacement-flow fluid velocity along straight radial blades as $\mu \rightarrow 0$.

Expansion (1.89) may be obtained from (1.57) by employing

$$\sin^2(\theta)I(\theta) + (1 - \cos(\theta))\, I_1 \sim \fint_{-\pi}^{\pi} (1 + \cos(\lambda))^{2/n} \frac{\mathrm{d}\lambda}{\cos(\lambda) - \sin(\theta)} \tag{1.90}$$

as $\mu \rightarrow 0$, and expanding the integral in a Fourier cosine series as done before. This will lead to a Fourier series with coefficients given by the beta function, which can be expressed alternatively by gamma functions, as is done in (1.89).

Figure 1.6 clearly demonstrates that the displacement flow velocity decreases as the number of blades increases. Moreover, since $1/(\Gamma(1-k)) = 0 \; \forall \; k \in I\!N^+$, it is seen from (1.89) that

$$R(\theta)\frac{w_{rp}}{\Omega r_2} \sim \Phi \tag{1.91}$$

as $n \rightarrow \infty$, complying fully with one-dimensional Eulerian flow theory. Also, note that the series in (1.89) terminates for $n = 1$ and $n = 2$ after two terms and one term respectively, yielding truncation-error free solutions.

Furthermore, it is seen from (1.89) that, for $\Phi = 0$,

$$\lim_{R \rightarrow 0} \left.\frac{w_{rp}}{\Omega r_2}\right|_{\Phi=0} \sim \begin{cases} \pm\infty & \text{when} \quad n = 1 \\ \pm 1 & \text{when} \quad n = 2 \\ 0 & \text{when} \quad n > 2 \end{cases} \tag{1.92}$$

as $\mu \rightarrow 0$, which can also be observed from figure 1.6. But, nonetheless, we still have for all blade numbers, for $\Phi \neq 0$,

$$\lim_{R \rightarrow 0} \frac{w_{rp}}{\Omega r_2} \sim +\infty \tag{1.93}$$

as $\mu \rightarrow 0$.

1.5.2 *Solutions for turbine impellers*

From (1.44), (1.51), (1.52), and (1.70), putting $\theta = \pi$ and using (1.46) we obtain that the blade circulation for turbine impellers fitted out with straight radial blades reads

$$n\varGamma_{bt} = \sigma_{t\varGamma}\varGamma_2 - \sigma_{t\varOmega}2\pi\varOmega r_1^2 \tag{1.94}$$

where the slip factors introduced are

$$\sigma_{t\varGamma} = 1 - \mu^{\frac{1}{2}} \tag{1.95}$$

$$\sigma_{t\varOmega} = (1-\mu)\left(\frac{2}{1+\mu^{\frac{1}{2}}}\right)^{4/n} F\left(\frac{2}{n},\frac{2}{n};1;\left(\frac{1-\mu^{\frac{1}{2}}}{1+\mu^{\frac{1}{2}}}\right)^2\right) - \tfrac{1}{2}(1-\mu)\mu^{\frac{1}{2}-2/n}F\left(\tfrac{1}{2},1-\frac{2}{n};2;1-\mu\right) \tag{1.96}$$

Note that $\sigma_{t\varGamma} = \sigma_{p\varGamma}$ and $\sigma_{t\varOmega} = (1-\mu)\tau_p - \mu^{\frac{1}{2}-2/n}\sigma_{p\varOmega}$.

Next summing (1.41), (1.51), (1.52), and (1.70), and using (1.94), we get the overall fluid velocity in the ζ-plane:

$$\begin{aligned} v_{t\zeta}(\theta) = &-\frac{\sin(\theta)}{\cos(\theta)+(1+\mu)/(1-\mu)}\frac{Q}{2\pi n} + \frac{1}{\mu^{\frac{1}{2}}}\frac{1+\cos(\theta)}{\cos(\theta)+(1+\mu)/(1-\mu)}\frac{\varGamma_1}{2\pi n} \\ &+ \varOmega r_1^2\frac{1-\mu}{n\mu^{\frac{1}{2}}}\left(\frac{2}{1+\mu^{\frac{1}{2}}}\right)^{4/n}\left\{\sin(\theta)\sum_{k=1}^{\infty}a_k\sin(k\theta) - \cos^2(\tfrac{1}{2}\theta)F\left(\frac{2}{n},\frac{2}{n};1;\left(\frac{1-\mu^{\frac{1}{2}}}{1+\mu^{\frac{1}{2}}}\right)^2\right)\right\} \end{aligned} \tag{1.97}$$

Then using transformation (1.71) we obtain, analogously to the solution for pump impellers, that the *radial* fluid velocity w_{rt} at the blades of radially bladed *turbine* impellers is given by

$$\begin{aligned} w_{rt} = &\frac{Q}{2\pi r} - \frac{\operatorname{cotan}(\frac{1}{2}\theta)}{\mu^{\frac{1}{2}}}\frac{\varGamma_1}{2\pi r} - \{R(\theta)\}^{n-1}\frac{2\varOmega r_1^2}{r_2\mu^{\frac{1}{2}}}\left(\frac{2}{1+\mu^{\frac{1}{2}}}\right)^{4/n} \\ &\times\left\{\sum_{k=1}^{\infty}a_k\sin(k\theta) - \tfrac{1}{2}\operatorname{cotan}(\tfrac{1}{2}\theta)F\left(\frac{2}{n},\frac{2}{n};1;\left(\frac{1-\mu^{\frac{1}{2}}}{1+\mu^{\frac{1}{2}}}\right)^2\right)\right\} \end{aligned} \tag{1.98}$$

In dimensionless form this yields

$$\begin{aligned} R(\theta)\frac{w_{rt}}{\varOmega r_2} = &\varPhi - \mu^{-\frac{1}{2}+2/n}\operatorname{cotan}(\tfrac{1}{2}\theta)\varUpsilon_1 - 2\{R(\theta)\}^n\mu^{-\frac{1}{2}+2/n}\left(\frac{2}{1+\mu^{\frac{1}{2}}}\right)^{4/n} \\ &\times\left\{\sum_{k=1}^{\infty}a_k\sin(k\theta) - \tfrac{1}{2}\operatorname{cotan}(\tfrac{1}{2}\theta)F\left(\frac{2}{n},\frac{2}{n};1;\left(\frac{1-\mu^{\frac{1}{2}}}{1+\mu^{\frac{1}{2}}}\right)^2\right)\right\} \end{aligned} \tag{1.99}$$

The vortex strength ($\varGamma_1$ in (1.98) and $\varUpsilon_1$ in (1.99)) is prescribed by

$$\varGamma_1 = (1-\sigma_{t\varGamma})\varGamma_2 + \sigma_{t\varOmega}2\pi\varOmega r_1^2 \tag{1.100}$$

which readily follows from (1.46) and (1.94); using dimensionless groups (1.100) becomes

$$\varUpsilon_1 = \sigma_{t\varOmega} + (1-\sigma_{t\varGamma})\mu^{-2/n}\varUpsilon_2 \tag{1.101}$$

where $\Upsilon_2 = \Gamma_2/(2\pi\Omega r_2^2)$.

Substituting (1.101) in (1.99) we further get, using (1.95),

$$R(\theta)\frac{w_{rt}}{\Omega r_2} = \Phi - \operatorname{cotan}(\tfrac{1}{2}\theta)(\Upsilon_2 + \mu^{-\frac{1}{2}+2/n}\sigma_{t\Omega}) - 2\left\{R(\theta)\right\}^n \mu^{-\frac{1}{2}+2/n}\left(\frac{2}{1+\mu^{\frac{1}{2}}}\right)^{4/n}$$
$$\times\left\{\sum_{k=1}^{\infty} a_k \sin(k\theta) - \tfrac{1}{2}\operatorname{cotan}(\tfrac{1}{2}\theta)F\left(\frac{2}{n},\frac{2}{n};1;\left(\frac{1-\mu^{\frac{1}{2}}}{1+\mu^{\frac{1}{2}}}\right)^2\right)\right\} \tag{1.102}$$

The prerotation or prewhirl (Γ_{2s}) required for shockless entry follows from (1.46), (1.48), (1.51), (1.52), and (1.70). It reads

$$\Gamma_{2s} = \tau_t 2\pi\Omega r_2^2 \tag{1.103}$$

or, using dimensionless groups,

$$\Upsilon_{2s} = \tau_t \tag{1.104}$$

where the (turbine) prerotation factor is given by

$$\tau_t = \mu^{\frac{1}{2}+2/n}\left(\frac{2}{1+\mu^{\frac{1}{2}}}\right)^{4/n} F\left(\frac{2}{n},\frac{2}{n};1;\left(\frac{1-\mu^{\frac{1}{2}}}{1+\mu^{\frac{1}{2}}}\right)^2\right) + \tfrac{1}{2}(1-\mu)F\left(\tfrac{1}{2},1-\frac{2}{n};2;1-\mu\right) \tag{1.105}$$

This prerotation factor will be further outlined in § 1.8, there we will also discuss the minimally required throughput, that is, the minimum flow coefficient (Φ_m), for turbine impellers. Incidentally, note that $\tau_t = \mu^{\frac{1}{2}+2/n}\tau_p + \sigma_{p\Omega}$.

To complete this section, we will demonstrate similarity between the flow fields for pump and turbine impellers. Both from (1.85), which is valid for pump impellers, and (1.99), which is valid for turbine impellers, it follows that the relative fluid velocity w_r along straight radial blades of either pump or turbine impellers operating under the condition of shockless entry, i.e. $\Upsilon_1 = \tau_p$ and $\Upsilon_2 = \tau_t$ for pump and turbine impellers respectively, is given in closed form by

$$R(\theta)\frac{w_{rt}}{\Omega r_2} = \Phi - \mu^{-\frac{1}{2}+2/n}\left(\frac{2}{1+\mu^{\frac{1}{2}}}\right)^{4/n}$$
$$\times\left\{2\{R(\theta)\}^n\sum_{k=1}^{\infty} a_k \sin(k\theta) + \tfrac{1}{2}(1-\mu)\sin(\theta)F\left(\frac{2}{n},\frac{2}{n};1;\left(\frac{1-\mu^{\frac{1}{2}}}{1+\mu^{\frac{1}{2}}}\right)^2\right)\right\} \tag{1.106}$$

where the blade radius ratio, $R(\theta)$, and the Fourier coefficients, a_k, are as given before by (1.11) and (1.68) respectively.

Note from (1.106) that at the blade tips (i.e. $\theta = 0$ and $\theta = \pi$) we have that $R(\theta)w_r/(\Omega r_2) = \Phi$; the disturbance due to the rotation of the impeller vanishes completely at the blades tips (for the case of straight radial blades).

Finally, to illustrate (1.102) we have plotted in figure 1.7 the dimensionless fluid velocity $w_{rt}/(\Omega r_2)$ for three distinct values of the prerotation, namely 90% of the value required for shockless entry, the value appropriate for shockless entry itself, and 110% of the value corresponding to shockless entry, all with the same volume flow rate (namely $\Phi = -0.319$).

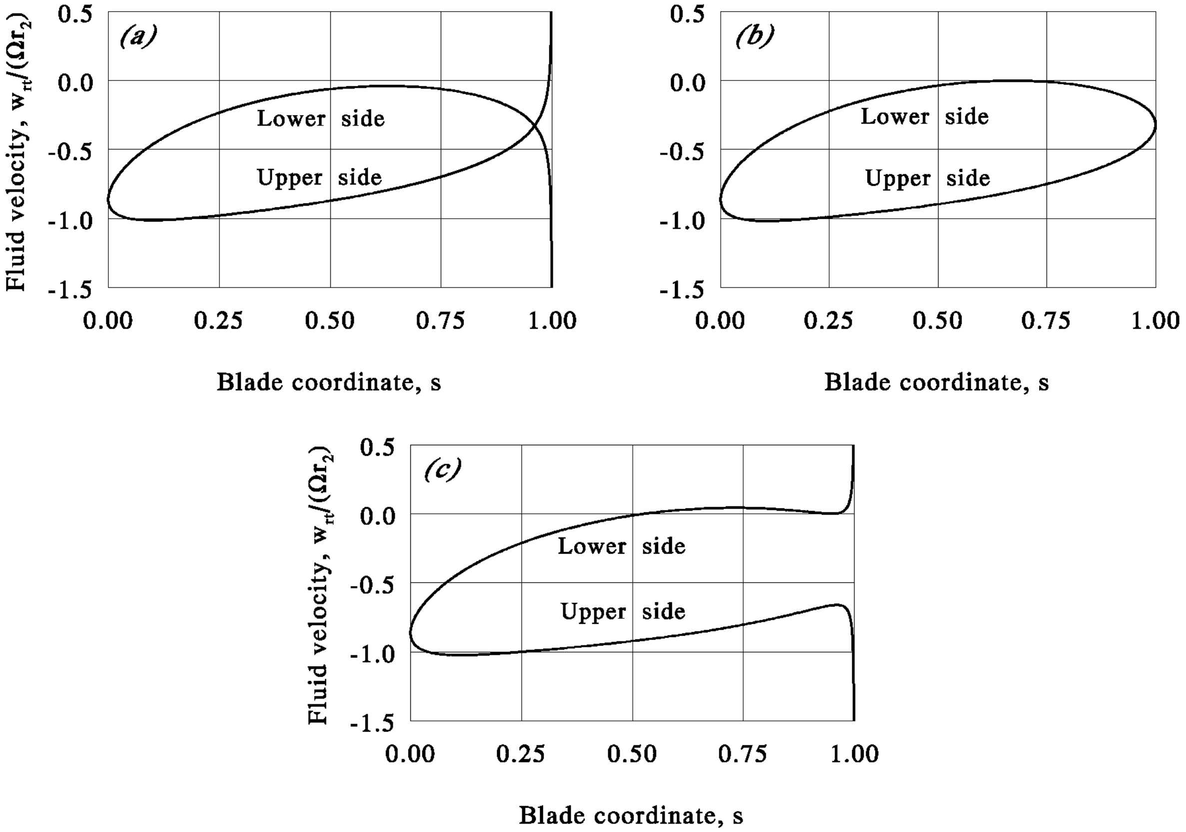

FIGURE 1.7. Exact solution of fluid velocities along straight radial blades of eight-bladed turbine impellers with inlet-to-outlet radius ratio of 0.37 ($\Phi = -0.319$; $\Upsilon_{2s} = 0.765$). (*a*) Low prerotation ($\Upsilon_2 = 0.9\Upsilon_{2s}$); (*b*) shockless prerotation ($\Upsilon_2 = \Upsilon_{2s}$); (*c*) high prerotation ($\Upsilon_2 = 1.1\Upsilon_{2s}$).

1.6 Asymptotic solutions for logarithmically bladed pump impellers

In this section pump impellers only will be considered, mainly because solutions in closed form have not (yet) been obtained for turbine impellers that are fitted out with (logarithmically) curved blades. This is not of major importance since most radial turbine impellers found in practice have straight radial blades – discussed in detail in the previous section – or are closely represented by these blades, in particular at the entrance section. In fact, blade curvature in radial turbomachines is more commonly applied to pumps and fans.

1.6.1 *Solutions from method of conformal mapping*

The solutions presented here give an account of the fluid velocity tangential at the blades of pump impellers equipped with logarithmic spiral blades having a high blade length to (equivalent) blade pitch ratio; that is, for the case in which the approximation $\mu_\beta = (r_1/r_2)^{n/\cos(\beta)} \to 0$ is justified.

With $\delta \sim \pi - 2\beta$ as $\mu_\beta \to 0$, and using (1.21) we first obtain from (1.28), (1.34) and (1.38)

$$v_{t\zeta}^{\Omega}(\theta) \sim \frac{M}{2\pi n}\int_{-\pi-2\beta}^{\pi-2\beta}\Big(\cos(\beta+\tfrac{1}{2}\lambda)\Big)^{-1+4\cos^2(\beta)/n} \mathrm{e}^{\lambda\sin(2\beta)/n}\sin(\tfrac{1}{2}\lambda)\mathrm{cotan}(\tfrac{1}{2}\theta-\tfrac{1}{2}\lambda)\mathrm{d}\lambda \quad (1.107)$$

$$v_{t\zeta}^{Q}(\theta) \sim -\frac{Q}{2\pi n}\tan(\beta + \tfrac{1}{2}\theta) \tag{1.108}$$

$$v_{t\zeta}^{\varGamma}(\theta) \sim \frac{\varGamma_1}{2\pi n} \tag{1.109}$$

as $\mu_\beta \to 0$, where

$$M = \varOmega r_2^2 \left(\cos(\beta)\right)^{1-4\cos^2(\beta)/n} \tag{1.110}$$

Expansions (1.108) and (1.109) are both simple expressions that need no further explanation. Relation (1.107) will be evaluated somewhat further since we are interested in solutions in closed form.

Substituting the trigonometric identity

$$\sin(\tfrac{1}{2}\lambda)\mathrm{cotan}(\tfrac{1}{2}\theta - \tfrac{1}{2}\lambda) = \frac{2\sin(\tfrac{1}{2}\theta)\sin(\tfrac{1}{2}\theta + \tfrac{1}{2}\lambda)}{\cos(\lambda) - \cos(\theta)} - \cos(\tfrac{1}{2}\lambda) \tag{1.111}$$

in (1.107) gives

$$v_{t\zeta}^{\varOmega}(\theta) \sim \frac{M}{2\pi n}\Big(2\sin(\tfrac{1}{2}\theta)J(\theta) - J_0\Big) \tag{1.112}$$

as $\mu_\beta \to 0$, in which

$$J(\theta) = \int_{-\pi-2\beta}^{\pi-2\beta} \Big(\cos(\beta + \tfrac{1}{2}\lambda)\Big)^{-1+4\cos^2(\beta)/n} \mathrm{e}^{\lambda\sin(2\beta)/n}\frac{\sin(\tfrac{1}{2}\theta + \tfrac{1}{2}\lambda)}{\cos(\lambda) - \cos(\theta)}\mathrm{d}\lambda \tag{1.113}$$

$$J_0 = \int_{-\pi-2\beta}^{\pi-2\beta} \Big(\cos(\beta + \tfrac{1}{2}\lambda)\Big)^{-1+4\cos^2(\beta)/n} \mathrm{e}^{\lambda\sin(2\beta)/n}\cos(\tfrac{1}{2}\lambda)\mathrm{d}\lambda \tag{1.114}$$

Next using the transformations $y = \lambda + 2\beta$ and $\alpha = \beta + \frac{1}{2}\lambda$, the integrals $J(\theta)$ and J_0 can be written as

$$J(\theta) = \mathrm{e}^{-2\beta\sin(2\beta)/n}\int_{-\pi}^{\pi} \Big(\cos(\tfrac{1}{2}y)\Big)^{-1+4\cos^2(\beta)/n} \mathrm{e}^{y\sin(2\beta)/n}\frac{\sin(\tfrac{1}{2}\theta + \tfrac{1}{2}y + \beta)}{\cos(y) - \cos(\theta + 2\beta)}\mathrm{d}y \tag{1.115}$$

$$J_0 = 2\mathrm{e}^{-2\beta\sin(2\beta)/n}\int_{-\pi/2}^{\pi/2} (\cos(\alpha))^{-1+4\cos^2(\beta)/n} \mathrm{e}^{2\alpha\sin(2\beta)/n}\cos(\alpha - \beta)\mathrm{d}\alpha \tag{1.116}$$

Since the latter integral is rather simple to evaluate we will work out (1.116) first; after that we will take a closer look at (1.115).

Substituting the trigonometric identity $\cos(\alpha - \beta) = \cos(\alpha)\cos(\beta) + \sin(\alpha)\sin(\beta)$ in (1.116) and thereupon integrating by parts we obtain

$$J_0 = \frac{2\mathrm{e}^{-2\beta\sin(2\beta)/n}}{\cos(\beta)}\int_{-\pi/2}^{\pi/2} (\cos(\alpha))^{4\cos^2(\beta)/n} \mathrm{e}^{2\alpha\sin(2\beta)/n}\mathrm{d}\alpha \tag{1.117}$$

This result can be stated equivalently by the beta function (see also Gradshteyn & Ryzhik 1980 p. 476) as

$$J_0 = \frac{2\pi\mathrm{e}^{-2\beta\sin(2\beta)/n}}{2^{4\cos^2(\beta)/n}\cos(\beta)\left(1 + 4\cos^2(\beta)/n\right)B(\chi, \overline{\chi})} \tag{1.118}$$

in which $B(-)$ is the beta function (see for instance Abramowitz & Stegun 1972), and where

$$\chi = 1 + \frac{2\cos^2(\beta)}{n} + \mathrm{i}\frac{\sin(2\beta)}{n} \tag{1.119}$$

Note that χ is a complex number; $B(\chi,\bar{\chi})$, however, is strictly real valued.

Having evaluated J_0 we now take a closer look at $J(\theta)$. First we rephrase (1.115) as

$$J(\theta) = \mathrm{e}^{-2\beta\sin(2\beta)/n}\left(\sin(\beta+\tfrac{1}{2}\theta)J_1(\theta)+\cos(\beta+\tfrac{1}{2}\theta)J_2(\theta)\right) \tag{1.120}$$

where

$$J_1(\theta) = \int_{-\pi}^{\pi}\left(\cos(\tfrac{1}{2}y)\right)^{4\cos^2(\beta)/n}\mathrm{e}^{y\sin(2\beta)/n}\frac{\mathrm{d}y}{\cos(y)-\cos(\theta+2\beta)} \tag{1.121}$$

$$J_2(\theta) = \int_{-\pi}^{\pi}\left(\cos(\tfrac{1}{2}y)\right)^{-1+4\cos^2(\beta)/n}\mathrm{e}^{y\sin(2\beta)/n}\frac{\sin(\frac{1}{2}y)}{\cos(y)-\cos(\theta+2\beta)}\mathrm{d}y \tag{1.122}$$

Then expanding the leading part of the integral (1.121) in a Fourier series, i.e.

$$\left(\cos(\tfrac{1}{2}y)\right)^{4\cos^2(\beta)/n}\mathrm{e}^{y\sin(2\beta)/n} = \tfrac{1}{2}B_0+\sum_{k=1}^{\infty}B_k\cos(ky)+\sum_{k=1}^{\infty}C_k\sin(ky) \tag{1.123}$$

where

$$B_k = \frac{1}{\pi}\int_{-\pi}^{\pi}\left(\cos(\tfrac{1}{2}\tau)\right)^{4\cos^2(\beta)/n}\mathrm{e}^{\tau\sin(2\beta)/n}\cos(k\tau)\mathrm{d}\tau \tag{1.124}$$

$$C_k = \frac{1}{\pi}\int_{-\pi}^{\pi}\left(\cos(\tfrac{1}{2}\tau)\right)^{4\cos^2(\beta)/n}\mathrm{e}^{\tau\sin(2\beta)/n}\sin(k\tau)\mathrm{d}\tau \tag{1.125}$$

and using (1.65) we obtain

$$J_1(\theta) = \frac{2\pi}{\sin(\theta+2\beta)}\sum_{k=1}^{\infty}B_k\sin(k\theta+2k\beta) \tag{1.126}$$

Next, to evaluate the $J_2(\theta)$, we consider the derivative of (1.123) with respect to y It reads

$$-\frac{2\cos^2(\beta)}{n}\left(\cos(\tfrac{1}{2}y)\right)^{-1+4\cos^2(\beta)/n}e^{y\sin(2\beta)/n}\sin(\tfrac{1}{2}y)+\frac{\sin(2\beta)}{n}\left(cos(\tfrac{1}{2}y)\right)^{4\cos^2(\beta)/n}e^{y\sin(2\beta)/n}$$

$$=\sum_{k=1}^{\infty}-kB_k\sin(ky)+\sum_{k=1}^{\infty}kC_k\cos(ky) \tag{1.127}$$

From (1.127) it then follows that

$$-\frac{2\cos^2(\beta)}{n}J_2(\theta)+\frac{\sin(2\beta)}{n}J_1(\theta) = \sum_{k=1}^{\infty}kC_k\int_{-\pi}^{\pi}\frac{\cos(ky)}{\cos(y)-\cos(\theta+2\beta)}\mathrm{d}y \tag{1.128}$$

which gives, again using (1.65),

$$J_2(\theta) = \tan(\beta)J_1(\theta)-\frac{\pi n}{\cos^2(\beta)\sin(\theta+2\beta)}\sum_{k=1}^{\infty}kC_k\sin(k\theta+2k\beta) \tag{1.129}$$

or, substituting (1.126),

$$J_2(\theta) = \frac{2\pi}{\cos(\beta)\sin(\theta+2\beta)}\left\{\sin(\beta)\sum_{k=1}^{\infty}B_k\sin(k\theta+2k\beta)-\frac{n}{2\cos(\beta)}\sum_{k=1}^{\infty}kC_k\sin(k\theta+2k\beta)\right\} \tag{1.130}$$

Substituting this result together with (1.126) in (1.120) we get

$$J(\theta) = \frac{\pi \mathrm{e}^{-2\beta \sin(2\beta)/n}}{\cos(\beta)\sin(\beta + \frac{1}{2}\theta)}$$

$$\times \left\{ \frac{\sin(2\beta + \frac{1}{2}\theta)}{\cos(\beta + \frac{1}{2}\theta)} \sum_{k=1}^{\infty} B_k \sin(k\theta + 2k\beta) - \frac{n}{2\cos(\beta)} \sum_{k=1}^{\infty} kC_k \sin(k\theta + 2k\beta) \right\} \tag{1.131}$$

The Fourier coefficients B_k and C_k in this equation, which are defined by (1.124) and (1.125), can be worked out somewhat further, simplifying their computation considerably.

Combining the Fourier coefficients to the complex number $B_k + \mathrm{i}C_k$ yields

$$B_k + \mathrm{i}C_k = \frac{1}{\pi} \int_{-\pi}^{\pi} \left(\cos(\tfrac{1}{2}\tau)\right)^{4\cos^2(\beta)/n} \mathrm{e}^{(\sin(2\beta)/n + \mathrm{i}k)\tau} \mathrm{d}\tau \tag{1.132}$$

This result can be expressed alternatively by the beta function, which gives (see also Gradshteyn & Ryzhik 1980 p. 476)

$$B_k + \mathrm{i}C_k = \frac{2^{1-4\cos^2(\beta)/n}}{(1 + 4\cos^2(\beta)/n)\, B(\chi_1^{(k)}, \chi_2^{(k)})} \tag{1.133}$$

in which

$$\chi_1^{(k)} = 1 + k + \frac{2\cos^2(\beta)}{n} - \mathrm{i}\frac{\sin(2\beta)}{n} \tag{1.134}$$

$$\chi_2^{(k)} = 1 - k + \frac{2\cos^2(\beta)}{n} + \mathrm{i}\frac{\sin(2\beta)}{n} \tag{1.135}$$

Then, substituting (1.110), (1.118), and (1.120) in (1.112) we obtain

$$v_{t\zeta}^{\Omega}(\theta) \sim \frac{\Omega r_2^2}{n} (\cos(\beta))^{-4\cos^2(\beta)/n} \mathrm{e}^{-2\beta\sin(2\beta)/n} \left(\frac{\sin(\frac{1}{2}\theta)}{\sin(\beta + \frac{1}{2}\theta)} \right.$$

$$\times \left\{ \frac{sin(2\beta + \frac{1}{2}\theta)}{\cos(\beta + \frac{1}{2}\theta)} \sum_{k=1}^{\infty} B_k \sin(k\theta + 2k\beta) - \frac{n}{2\cos(\beta)} \sum_{k=1}^{\infty} kC_k \sin(k\theta + 2k\beta) \right\}$$

$$\left. - \frac{1}{2^{4\cos^2(\beta)/n} (1 + 4\cos^2(\beta)/n)\, B(\chi, \bar{\chi})} \right) \tag{1.136}$$

as $\mu_\beta \to 0$, with χ according to (1.119) and where the Fourier coefficients B_k and C_k are conveniently given as the real and the imaginary parts of the right-hand side of (1.133).

Equation (1.136) gives the solution in closed form for the fluid velocity tangential at the unit circle in the ζ-plane, due to displacement, for logarithmically bladed impellers with a high solidity. Summing the individual contributions (1.108), (1.109), and (1.136) we obtain the overall velocity along the unit circle in the ζ-plane. Employing thereupon transformation (1.29) we get the fluid velocity in the physical plane. For the case of logarithmic spiral blades with a high solidity, this transformation becomes

$$\frac{v_{tz}}{v_{t\zeta}} \sim \frac{n\cos(\beta + \frac{1}{2}\theta)}{R(\theta) r_2} \frac{1}{|\sin(\frac{1}{2}\theta)|} \tag{1.137}$$

as $\mu_\beta \to 0$, with $R(\theta)$ being given by (1.21).

Next, substituting (1.108), (1.109), and (1.136) in (1.41) we obtain that the blade circulation of high-solidity logarithmically-bladed pump impellers is given by

$$n\mathit{\Gamma}_{bp} \sim \sigma_{p\mathit{\Omega}} 2\pi \mathit{\Omega} r_2^2 + Q\tan(\beta) - \mathit{\Gamma}_1 \tag{1.138}$$

as $\mu_\beta \to 0$, in which the slip factor reads

$$\sigma_{p\mathit{\Omega}} \sim \frac{\mathrm{e}^{-2\beta\sin(2\beta)/n}}{(1+4\cos^2(\beta)/n)\,(2\cos(\beta))^{4\cos^2(\beta)/n}\,B(\chi,\bar{\chi})} \tag{1.139}$$

as $\mu_\beta \to 0$; this slip factor will be further discussed in § 1.7.

The exact formulation, that is the non-asymptotic counterpart, of (1.138) reads (see also Visser 1991)

$$n\mathit{\Gamma}_{bp} = \sigma_{p\mathit{\Omega}} 2\pi \mathit{\Omega} r_2^2 + \sigma_{pQ} Q\tan(\beta) - \sigma_{p\mathit{\Gamma}}\mathit{\Gamma}_1 \tag{1.140}$$

where (for logarithmically bladed pump impellers)

$$\sigma_{p\mathit{\Omega}} = -\frac{n v_{t\zeta}^{\mathit{\Omega}}(0)}{\mathit{\Omega} r_2^2} = \frac{n}{2\pi}\int_{\delta-2\pi}^{\delta} R(\lambda)\frac{\mathrm{d}R}{\mathrm{d}\lambda}\frac{\sin(\lambda)}{\cos(\lambda)-1}\mathrm{d}\lambda \tag{1.141}$$

$$\sigma_{pQ} = -\frac{2\pi n v_{t\zeta}^{Q}(0)}{Q\tan(\beta)} = \frac{2a\sin(\delta)\mathrm{cotan}(\beta)}{1-2a\cos(\delta)+a^2} \tag{1.142}$$

$$\sigma_{p\mathit{\Gamma}} = \frac{2\pi n v_{t\zeta}^{\mathit{\Gamma}}(0)}{\mathit{\Gamma}_1} = \frac{2(1-a\cos(\delta)}{1-2a\cos(\delta)+a^2} \tag{1.143}$$

Relation (1.140), in fact, results from the superposition of the individual contributions of the respective subflows. Regarding the source and vortex (sub)flows it is further seen (recalling (1.13)) that $\sigma_{pQ} = \sigma_{p\mathit{\Gamma}}$. Furthermore, with reference to (1.16), (1.17), and (1.18) it follows from (1.142) and (1.143) that

$$\sigma_{pQ} = \sigma_{p\mathit{\Gamma}} \sim 1 - (\mu_\beta)^{1/(2\cos(\beta))}\,\mathrm{e}^{2\beta\tan(\beta)} \tag{1.144}$$

as $\mu_\beta \to 0$, which shows that σ_{pQ} and $\sigma_{p\mathit{\Gamma}}$ are very close to 1 for practical cases (e.g. $n = 5$ blades, $r_1/r_2 = 0.4$, and $\beta = \frac{1}{3}\pi$ gives $\sigma_{pQ} = \sigma_{p\mathit{\Gamma}} \approx 0.996$). Therefore, it will usually suffice to take only $\sigma_{p\mathit{\Omega}}$ into account.

Finally, summing (1.41), (1.108), (1.109), and (1.136), and using (1.138), we obtain the overall fluid velocity tangential at the unit circle in the ζ-plane for logarithmically bladed pump impellers:

$$\begin{aligned} v_{t\zeta}(\theta) \sim &-\frac{Q\sin(\frac{1}{2}\theta)}{2\pi n\cos(\beta)\cos(\beta+\frac{1}{2}\theta)} + \frac{\mathit{\Omega} r_2^2}{n}(\cos(\beta))^{-4\cos^2(\beta)/n}\,\mathrm{e}^{-2\beta\sin(2\beta)/n}\frac{\sin(\frac{1}{2}\theta)}{\sin(\beta+\frac{1}{2}\theta)} \\ &\times\left\{\frac{sin(2\beta+\frac{1}{2}\theta)}{\cos(\beta+\frac{1}{2}\theta)}\sum_{k=1}^{\infty}B_k\sin(k\theta+2k\beta) - \frac{n}{2\cos(\beta)}\sum_{k=1}^{\infty}kC_k\sin(k\theta+2k\beta)\right\} \end{aligned} \tag{1.145}$$

as $\mu_\beta \to 0$. Note that in this equation the contribution of the vortex has vanished completely. This, however, is not surprising since we are dealing with pump impellers fitted out with blades rising from the centre.

Then employing transformation (1.137), bearing in mind that $r = r(\theta) = r_2 R(\theta)$, and using the auxiliary relations $v_{tz}^{+} = -v_s$ and $v_{tz}^{-} = +v_s$, we obtain from (1.145) that

$$v_s(\theta) \sim \frac{Q}{2\pi r\cos(\beta)} - \frac{\Omega r_2^2}{r}\left(\cos(\beta)\right)^{-4\cos^2(\beta)/n} \mathrm{e}^{-2\beta\sin(2\beta)/n} \mathrm{cotan}(\beta + \tfrac{1}{2}\theta)$$

$$\times \left\{ \frac{sin(2\beta + \frac{1}{2}\theta)}{\cos(\beta + \frac{1}{2}\theta)} \sum_{k=1}^{\infty} B_k \sin(k\theta + 2k\beta) - \frac{n}{2\cos(\beta)} \sum_{k=1}^{\infty} kC_k \sin(k\theta + 2k\beta) \right\} \qquad (1.146)$$

as $\mu_\beta \to 0$, where v_s is the *absolute* fluid velocity tangential at the blades, directed outwards. The corresponding *relative* fluid velocity w_s follows from the transformation $w_s = v_s - \Omega r\sin(\beta)$. This way we obtain, employing a dimensionless notation,

$$R(\theta)\frac{w_s}{\Omega r_2} \sim \frac{\Phi}{\cos(\beta)} - \{R(\theta)\}^2 \sin(\beta) - \left(\cos(\beta)\right)^{-4\cos^2(\beta)/n} \mathrm{e}^{-2\beta\sin(2\beta)/n} \mathrm{cotan}(\beta + \tfrac{1}{2}\theta)$$

$$\times \left\{ \frac{sin(2\beta + \frac{1}{2}\theta)}{\cos(\beta + \frac{1}{2}\theta)} \sum_{k=1}^{\infty} B_k \sin(k\theta + 2k\beta) - \frac{n}{2\cos(\beta)} \sum_{k=1}^{\infty} kC_k \sin(k\theta + 2k\beta) \right\} \qquad (1.147)$$

as $\mu_\beta \to 0$, in which Φ is the flow rate coefficient and $R(\theta)$ is the dimensionless radius, as introduced before. Note that (1.147) readily reduces to (1.89) for the case of straight radial blades (i.e. $\beta = 0$).

Based on (1.147) we have plotted in figure 1.8 the relative fluid velocity (w_s) due to the rotational speed, that is at zero throughput (i.e. $\Phi = 0$), for several eight-bladed pump impeller configurations. The graphs of this figure are appropriate for both backwardly (i.e. $\Omega < 0$) and forwardly (i.e. $\Omega > 0$) curved blades. The figure clearly shows that the displacement flow velocity diminishes as the blade angle increases. This, and other features, will be discussed further in § 1.7.

1.6.2 *Solutions from the asymptotic expansion of the Poisson equation*

In addition to the previous subsection, we shall discuss here the asymptotic behaviour of the solution for the relative fluid velocity – obtained from the asymptotic expansion of the Poisson equation – which enables blade-to-blade computation of impeller passage flows. In particular, this leads to a predominant expression for (hydrodynamic) blade loading, which is not only convenient in use but also more accurate than (most of the) relations generally known (see for instance Cumpsty 1989 for a general discussion on blade loading).

The results presented are appropriate for logarithmic spiral blades and hold asymptotically in a region well away form the blade tips, that is for points located well inside the blade passage at a radius r with $(1 + 2\pi\cos(\beta)/n)r_1 \ll r \ll (1 - 2\pi\cos(\beta)/n)r_2$. The analysis differs from the one outlined in the previous subsection, in that it focusses attention on the spanwise passage velocity rather than on the fluid velocity tangential at the blades (yielding a solution that matches up with the one previously discussed, as will be demonstrated).

In order to obtain the descriptions (in closed form) for the passage flow (i.e. the spanwise relative fluid velocity) we will evaluate the Laplacian of the stream function for the relative flow. Unlike the absolute flow, this flow is stationary for the case of a free (i.e. unbounded) impeller, and, hence, it is easier to describe than the absolute flow, which is periodical.

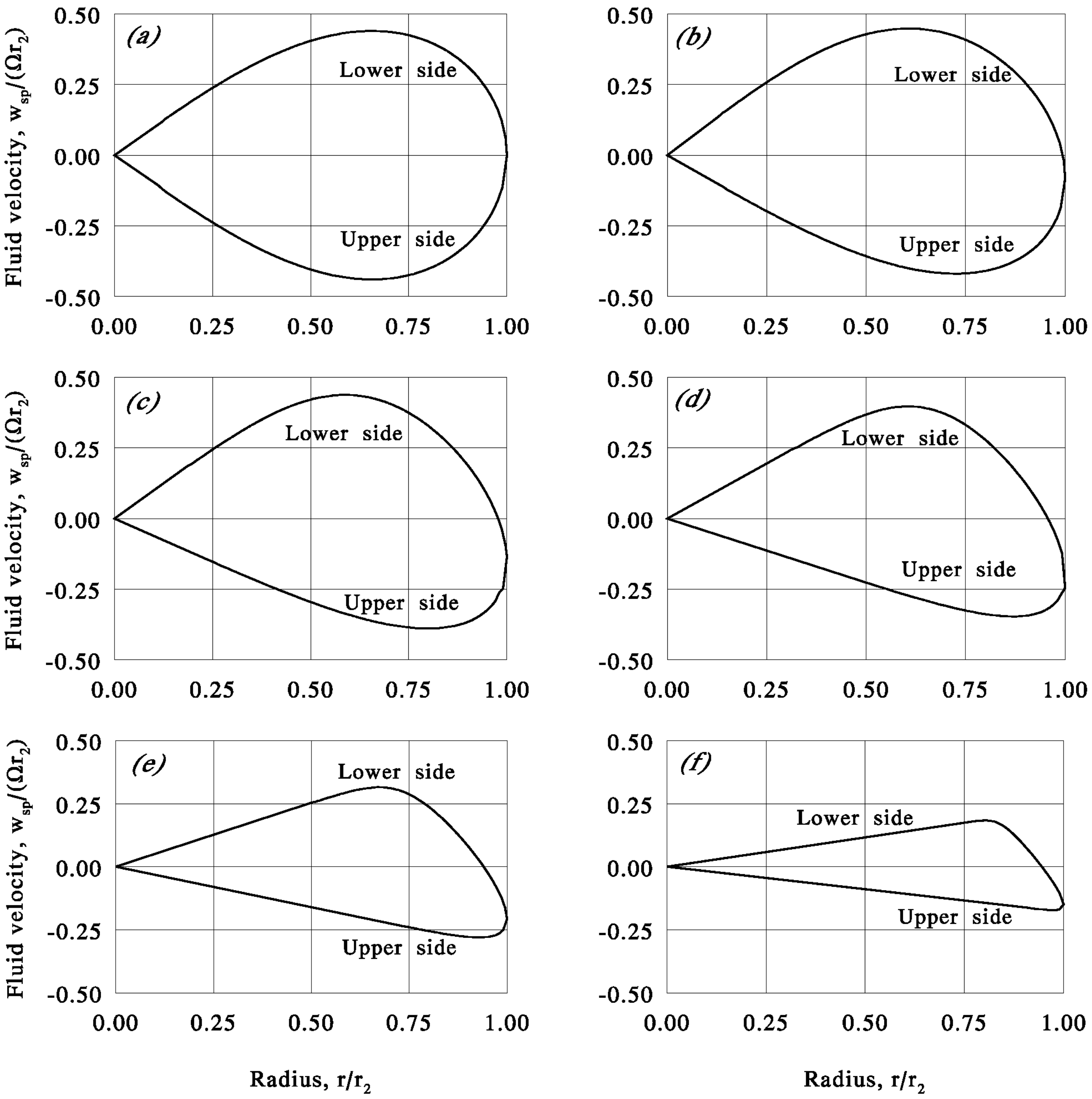

FIGURE 1.8. Displacement flow velocity along logarithmically curved blades of eight-bladed impellers as $\mu_\beta \to 0$. (*a*) $\beta = 0$; (*b*) $\beta = 15°$; (*c*) $\beta = 30°$; (*d*) $\beta = 45°$; (*e*) $\beta = 60°$; (*f*) $\beta = 75°$.

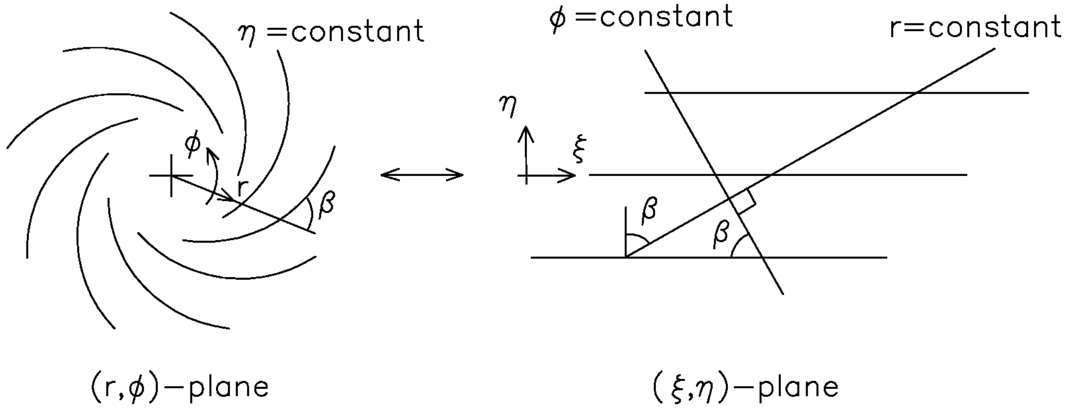

FIGURE 1.9. Logarithmic transformation.

However, considering the flow in a (free) impeller in a frame of reference rotating with the impeller itself, introduces an axial component of relative vorticity equal to -2Ω, which, in turn, is reflected in the equation governing the relative flow. Denoting the relative stream function by κ, it is found that (see also Kucharski 1918, p. 73 or Vavra 1960, p. 226)

$$\nabla^2\kappa = 2\Omega \tag{1.148}$$

To solve (1.148) we introduce the logarithmic transformation

$$\xi = \cos(\beta)\ln\left(\frac{r}{r_2}\right) + \phi\sin(\beta) \tag{1.149}$$

$$\eta = -\sin(\beta)\ln\left(\frac{r}{r_2}\right) + \phi\cos(\beta) \tag{1.150}$$

By this transformation (see also figure 1.9), logarithmic spiral blades are conveniently described by η = constant, as can be readily verified by substitution of (1.2) in (1.150). In particular, we obtain from (1.149) and(1.150) after substituting (1.2) that the j^{th}-blade is described in the (ξ,η)-plane by

$$[\xi(r)]_j = \frac{1}{\cos(\beta)}\ln\left(\frac{r}{r_2}\right) + \left(\phi_{o1} + 2\pi\frac{j-1}{n}\right)\sin(\beta) \tag{1.151}$$

$$[\eta]_j = \left(\phi_{o1} + 2\pi\frac{j-1}{n}\right)\cos(\beta) \tag{1.152}$$

Utilising the transformation we find that we may write (1.148) alternatively as

$$\frac{\partial^2\kappa}{\partial\xi^2} + \frac{\partial^2\kappa}{\partial\eta^2} = 2\Omega r_2^2 \mathrm{e}^{2\xi\cos(\beta)-2\eta\sin(\beta)} \tag{1.153}$$

Then employing scale coordinates ($\tilde{\xi}$,$\tilde{\eta}$) $\in$ [0,1], defined by

$$\tilde{\xi} = \frac{\xi - \xi_1}{\xi_2 - \xi_1} \tag{1.154}$$

$$\tilde{\eta} = \frac{\eta - \eta_1}{\eta_2 - \eta_1} \tag{1.155}$$

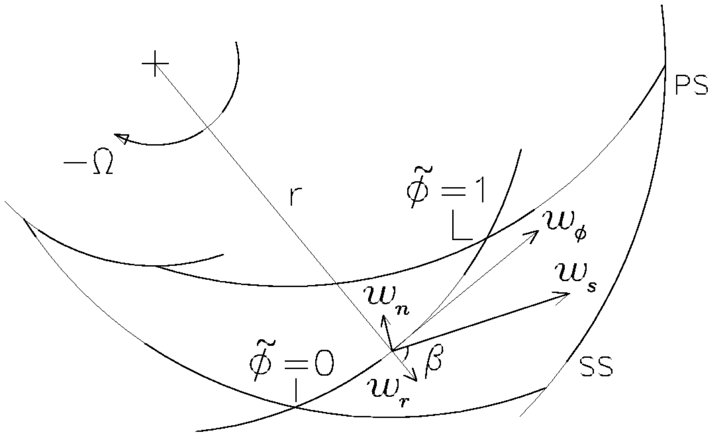

FIGURE 1.10. Passage velocities.

with $\xi_1 = [\xi(r_1)]_j$, $\xi_2 = [\xi(r_2)]_j$, $\eta_1 = [\eta]_j$ and $\eta_2 = [\eta]_{j+1}$, yielding

$$\xi = \xi_1 + \frac{\tilde{\xi}}{\cos(\beta)} \ln\left(\frac{r_2}{r_1}\right) \tag{1.156}$$

$$\eta = \eta_1 + \frac{2\pi\cos(\beta)}{n}\tilde{\eta} \tag{1.157}$$

we may shape (1.153) in a dimensionless form as

$$\left(\frac{n}{2\pi\cos(\beta)}\right)^2 \left\{ \left(-\frac{2\pi\cos(\beta)}{\ln(\mu_\beta)}\right)^2 \frac{\partial^2\tilde{\kappa}}{\partial\tilde{\xi}^2} + \frac{\partial^2\tilde{\kappa}}{\partial\tilde{\eta}^2} \right\} = 2\tilde{\Omega}\frac{\mathrm{e}^{2\xi_1\cos(\beta)+2\tilde{\xi}\ln(r_2/r_1)}}{\mathrm{e}^{2\eta_1\sin(\beta)+2\pi\tilde{\eta}\sin(2\beta)}} \tag{1.158}$$

where we additionally have put $\kappa = \tilde{\kappa}\Omega_0 r_2^2$ and $\Omega = \tilde{\Omega}\Omega_0$.

From (1.158) it is readily seen that the assumption of a high solidity[†] will lead to (restoring physical dimensions)

$$\frac{\partial^2\kappa}{\partial\eta^2} \sim 2\Omega r_2^2 \mathrm{e}^{2\xi\cos(\beta)-2\eta\sin(\beta)} \tag{1.159}$$

as $\mu_\beta \to 0$. This equation is easily solved, which results after some rearranging in

$$\kappa(\xi,\eta) \sim \kappa_1 + \frac{Q}{2\pi\cos(\beta)}(\eta-\eta_1) + \frac{\Omega r_2^2\mathrm{e}^{2\xi\cos(\beta)}}{2\sin^2(\beta)}\left(\mathrm{e}^{-2\eta\sin(\beta)} - \mathrm{e}^{-2\eta_1\sin(\beta)}\right)$$

$$+ \frac{n\Omega r_2^2\mathrm{e}^{2\xi\cos(\beta)}}{4\pi\sin^2(\beta)\cos(\beta)}(\eta-\eta_1)\left(\mathrm{e}^{-2\eta_1\sin(\beta)} - \mathrm{e}^{-2\eta_2\sin(\beta)}\right) \tag{1.160}$$

as $\mu_\beta \to 0$, in which we have incorporated (boundary conditions) $\kappa(\xi,\eta_1) = \kappa_1 (= \text{constant})$ and $\kappa(\xi,\eta_2) - \kappa(\xi,\eta_1) = \kappa_2 - \kappa_1 = Q/n$.

Equation (1.160) describes the asymptotic behaviour of the stream function for the relative flow between two consecutive logarithmic spiral blades in a region well away from

---

[†] For logarithmic spiral blades it is found that the solidity, say s, equals $s = \int_{r_1}^{r_2} \frac{\mathrm{d(chord)}}{\mathrm{pitch}} = -\frac{\ln(\mu_\beta)}{2\pi\cos(\beta)}$.

the blade tips. From this stream function we next may obtain the streamwise passage velocity

$$w_s = w_r \cos(\beta) + w_\phi \sin(\beta) \tag{1.161}$$

and the normal component, or cross-passage fluid velocity,

$$w_n = -w_r \sin(\beta) + w_\phi \cos(\beta) \tag{1.162}$$

by

$$w_s = \frac{1}{r}\frac{\partial \kappa}{\partial \eta} \tag{1.163}$$

$$w_n = -\frac{1}{r}\frac{\partial \kappa}{\partial \xi} \tag{1.164}$$

which is easily derived employing transformation (1.149)–(1.150) and using the (common) definitions of w_r and w_ϕ, i.e. $w_r = \frac{1}{r}\frac{\partial \kappa}{\partial \phi}$ and $w_\phi = -\frac{\partial \kappa}{\partial r}$.

Evaluating (1.163) and (1.164) and rearranging slightly, we find that the fluid velocities (see also figure 1.10) are given by

$$w_s(r,\lambda) \sim \frac{Q}{2\pi r \cos(\beta)} + \frac{\Omega r}{\sin(\beta)}\left(\frac{\sinh(t)}{t}\mathrm{e}^{\lambda \sin(2\beta) - t} - 1\right) \tag{1.165}$$

$$w_n(r,\lambda) \sim -\frac{\Omega r \cos(\beta)}{\sin^2(\beta)}\left(1 - e^{\lambda \sin(2\beta)} + \frac{n\lambda}{\pi}\sinh(t)\mathrm{e}^{\lambda \sin(2\beta) - t}\right) \tag{1.166}$$

as $\mu_\beta \to 0$, in which $\lambda = (\eta - \eta_1)/\cos(\beta)$, $t = \pi \sin(2\beta)/n$, and where we have used the fact that $\eta_2 - \eta_1 = 2\pi \cos(\beta)/n$ as well as $r = r_2 \mathrm{e}^{\xi \cos(\beta) - \eta \sin(\beta)}$.

To illustrate the asymptotic solution for the passage flow we have plotted in figure 1.11 the displacement (i.e. zero throughput) velocities for the case of five, nine, and fifteen 60°, logarithmic spiral blades. Clearly we detect a negative streamwise velocity contribution along the pressure side of the blades due to the revolution of the impeller. This is commonly interpreted as being the result of a relative eddy located between consecutive blades, which, basically, originates from the irrotationality of the absolute flow; the relative flow, as mentioned before, possesses a vorticity equal to -2Ω. The cross-passage fluid velocity is seen to be significantly smaller than the streamwise component—particularly when the throughput velocity $(Q/(2\pi r \cos(\beta))$ is superposed, which should preferably be such that $w_s \geq 0 \; \forall \lambda \in [0, 2\pi/n]$.

Finally, focussing attention on the flow along the blades (i.e. $\lambda = 0$ and $\lambda = 2\pi/n$) we obtain, employing a dimensionless notation as before,

$$\frac{w_s^+}{\Omega r_2} \sim \frac{\Phi}{R\cos(\beta)} + \frac{R}{\sin(\beta)}\left(\frac{\sinh(t)}{t}\mathrm{e}^{-t} - 1\right) \tag{1.167}$$

$$\frac{w_n^+}{\Omega r_2} \sim 0 \tag{1.168}$$

for the upper (+) blade surfaces, and

$$\frac{w_s^-}{\Omega r_2} \sim \frac{\Phi}{R\cos(\beta)} + \frac{R}{\sin(\beta)}\left(\frac{\sinh(t)}{t}\mathrm{e}^{t} - 1\right) \tag{1.169}$$

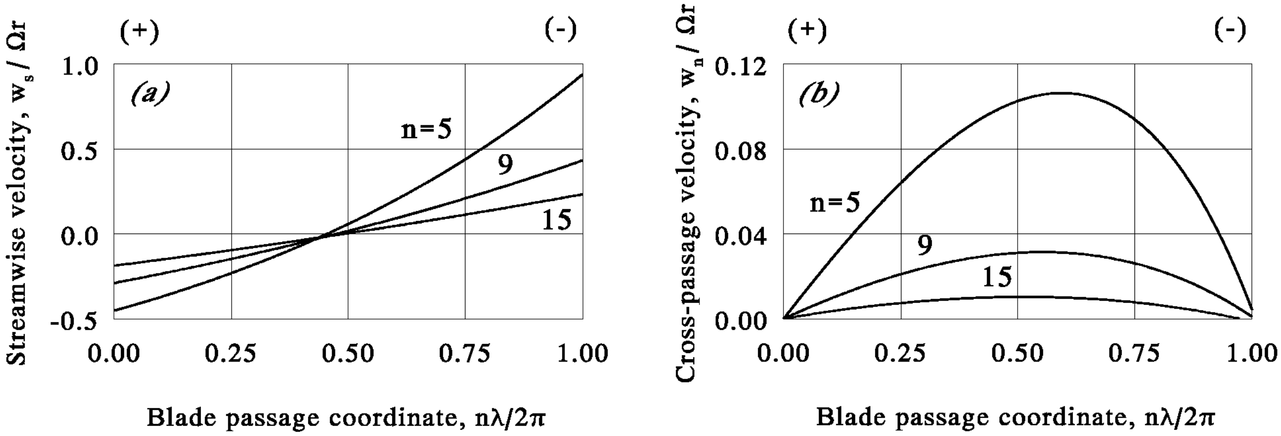

FIGURE 1.11. Zero-throughput (displacement) velocities according to (1.165) and (1.166), (*a*) and (*b*) respectively, for five, nine, and fifteen 60°, logarithmic spiral blades.

$$\frac{w_n^-}{\Omega r_2} \sim 0 \tag{1.170}$$

for the lower $(-)$ blade surfaces as $\mu_\beta \to 0$.

Solutions (1.167) and (1.169) agree perfectly with solution (1.147) for $r \ll r_2$ (i.e. $R \ll 1$), which solution was illustrated in figure 1.8; the latter being, in fact, the solution for the limiting case $r_1 \to 0$. Furthermore, we see that the normal wall velocities properly comply with the boundary conditions $(w_n|_{\lambda=0} = w_n|_{\lambda=2\pi/n} = 0)$.

From (1.167) and (1.169) we further obtain, restoring physical dimensions,

$$w_s^+ \sim \frac{Q}{2\pi r \cos(\beta)} - \frac{2\pi \Omega r \cos(\beta)}{n} \tag{1.171}$$

$$w_s^- \sim \frac{Q}{2\pi r \cos(\beta)} + \frac{2\pi \Omega r \cos(\beta)}{n} \tag{1.172}$$

as $n \to 0$ (i.e. $t \to 0$). This result displays even more clearly that there is a negative contribution to the streamwise velocity due to the rotational speed. It also clearly shows that the magnitude of this negative contribution is influenced by the number of blades and the blade curvature. Moreover, it enables a swift quantification of the relative influence of the number of blades and the blade curvature (e.g. changing the blade angle from 0° to 60° will evidently have (approximately) the same effect as quadrupling the number of (radial) blades).

Lastly, we may formulate an expression for the blade loading. This is an important impeller design parameter, which is often expressed as the difference in the fluid velocities on the suction and pressured side of a blade at the same radius. Alternatively, the loading may also be thought of in terms of the pressure difference (§ 1.7).

Expressing the blade loading as the difference in the (tangential) fluid velocity, we directly obtain from (1.167) and (1.169) an asymptotic approximation, i.e.

$$\frac{w_s^- - w_s^+}{\Omega r_2} \sim \frac{2R \sinh^2(t)}{t \sin(\beta)} \tag{1.173}$$

as $\mu_\beta \to 0$, with t as given before. This expansion enables swift (asymptotic) computation of the blade loading in a region well away from the blade tips. For the limiting case of

$t \to 0$ we further note that we may write

$$\frac{w_s^- - w_s^+}{\Omega r_2} \sim \frac{4\pi R \cos(\beta)}{n} \tag{1.174}$$

which is an expression for the blade loading that is often encountered in turbomachinery literature. It readily shows that the blade loading is affected favourably by increasing the number of blades and the blade curvature. More details on the blade loading will be given in § 1.7. In particular, the loading in terms of the pressure difference will be outlined there.

1.7 Analytical expressions for impeller design parameters: Pump Impellers

The solutions given in the previous sections enable the derivation of analytical expressions for parameters which govern the performance of radial-flow pump impellers. (Turbine impellers will be discussed in § 1.8.) Parameters concerned are: prerotation and condition of shockless entry, delivered head, minimum volume flow rate to avoid reverse flow between the blades, pressure distribution along the blades (i.e. blade loading), and dimensions required for impeller housing. Results for each of these items are discussed below. The findings presented provide an improvement and extension to the design formulae commonly applied (at the preliminary design stage) in the engineering of radial-flow pumps and fans; such formulae (still) being largely based on the application of one-dimensional Eulerian flow theory.

1.7.1 *Prerotation and condition of shockless entry*

By giving the inlet flow the appropriate prerotation or prewhirl we have the possibility of realizing shockless entry, for each operation point individually, so that impact losses can be minimized. Alternatively, for *backward-leaning blades*, shockless entry can be achieved by properly selecting the flow rate to angular speed ratio, i.e. the (volume) flow rate coefficient Φ. At this point, however, attention will primarily be confined to impellers fitted out with straight radial blades, since only for this type of impeller have solutions in closed form been given with respect to the condition of shockless entry. For logarithmic spiral blades we will merely discuss a simple approximation that relates flow rate and angular speed at shock-less entry.

To start the discussion of the subject, we first bring back to mind (1.86) and (1.88). These equations enable exact evaluation of the prerotation (Γ_{1s}) required to obtain shockless entry for pump impellers equipped with straight radial blades. Most impellers in practice, however, do not require exact evaluation since they are characterized by $\mu \ll 1$, so that we may approximate asymptotically.

Expanding the prerotation factor (1.88) asymptotically, we get

$$\tau_p \sim 2^{4/n}(1 - 4\mu^{\frac{1}{2}}/n)F(2/n, 2/n; 1; 1 - 4\mu^{\frac{1}{2}}) \tag{1.175}$$

as $\mu^{\frac{1}{2}} \to 0$, or

$$\tau_p \sim 2^{4/n} \frac{\Gamma(1 - 4/n)}{\{\Gamma(1 - 2/n)\}^2} \tag{1.176}$$

as $\mu^{\frac{1}{2}} \to 0$, provided that $n > 4$.

The exact value (1.88) and asymptotic expansion (1.176) of the prerotation factor are illustrated in figures 1.12(*a*) and 1.12(*b*) respectively. Note that the prerotation factor is always larger than the Eulerian value of unity, and also that when the number of blades becomes infinitely large the prerotation factor becomes unity.

Unfortunately, the above-given formulae strictly relate to the case(s) of straight radial blades, whereas most practical pump designs have curved blades. Therefore, we will extend the results obtained thus far, so that we will be able to predict the prerotation for curved blades as well. To that end we will give an approximation for the prerotation (factor), appropriate for logarithmic spiral blades, since exact solutions in closed form with respect to the condition of shockless entry are not available.

The prerotation or prewhirl required at shockless entry for logarithmically bladed pump impellers reads (see also Visser 1991)

$$\varGamma_{1s} = \tau_\beta 2\pi\varOmega r_1^2 + Q\tan(\beta) \tag{1.177}$$

which readily follows form the superposition of the individual contributions of the displacement flow and source flow. From this equation we obtain that it is possible to obtain zero-prerotation shockless entry when the volume flow rate coefficient ($\varPhi$) of *backwardly curved impellers* (!) equals

$$\varPhi_s = -\tau_\beta \left(\frac{r_1}{r_2}\right)^2 \text{cotan}(\beta) \tag{1.178}$$

For all other values of $\varPhi$ (i.e. $\varPhi \neq \varPhi_s$) a prewhirl will be required to obtain shockless entry.

To compute either the prerotation ($\varGamma_{1s}$) required or the appropriate volume flow rate ($\varPhi_s$) we see that we need to know τ_β, which, in general, is a function of the blade curvature and the number of blades. A simple expression that proved to be of proper use reads

$$\tau_\beta = 1 + (\tau_p - 1)cos(\beta) \tag{1.179}$$

This relation states that $1 \leq \tau_\beta \leq \tau_p$. (For an infinite number of blades τ_β becomes equal to unity, and for straight radial blades (i.e $\beta = 0$) we get $\tau_\beta = \tau_0 = \tau_p$.)

The prediction of τ_β according to (1.179) is not exact, but it will give a reasonable indication of the actual value. Numerical tests, i.e. potential flow calculations in logarithmically bladed impellers by means of the finite element method, have corroborated the validity of the approximation (particularly the cases of high solidity).

Lastly, it is noted that, in general, the prerotation for pump impellers (not necessarily the shockless one) is bounded, that is there is a maximum value to be given to the prewhirl. This arises from the fact that $n\varGamma_{bp}$ (representing, in fact, the mechanical work transferred to the fluid) has to be positive. With reference to (1.138) this implies the condition

$$\varGamma_1 < \frac{\sigma_{p\varOmega}}{\sigma_{p\varGamma}} 2\pi\varOmega r_2^2 + \frac{\sigma_{pQ}}{\sigma_{p\varGamma}} Q\tan(\beta) \tag{1.180}$$

otherwise the machine is working neutral or as a turbine.

1.7.2 *Developed head and slip factors*

We start this subsection by recollecting Euler's turbine equation. For a circular cascade or isolated (unbounded) impeller this may be written conveniently as (see for instance Betz

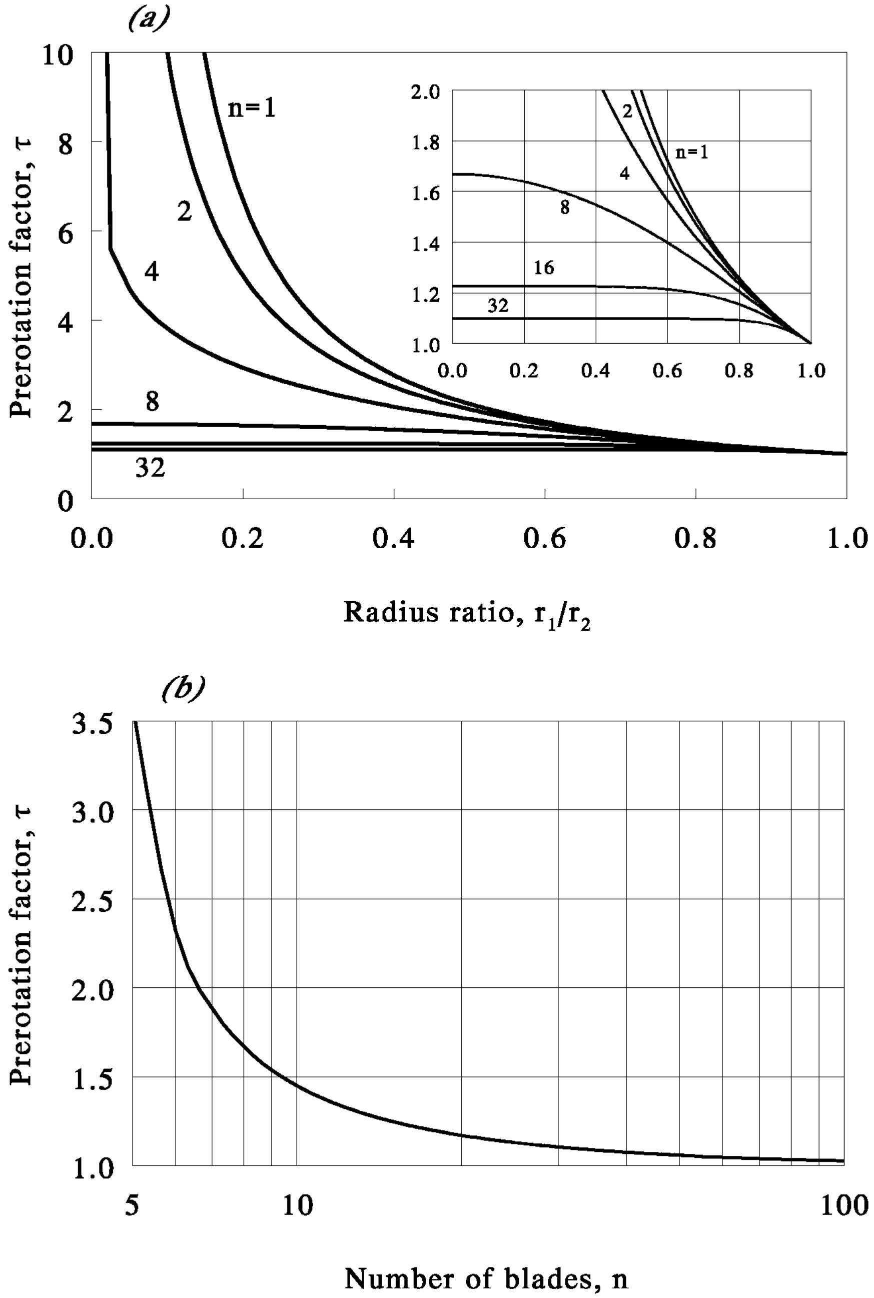

FIGURE 1.12. Prerotation factor for pump impellers fitted out with straight radial blades: (*a*) exact value; (*b*) asymptotic solution as $\mu^{\frac{1}{2}} \to 0$.

1966, p.84)

$$M = \rho Q \frac{\Gamma_2 - \Gamma_1}{2\pi} \tag{1.181}$$

in which M is torque, or moment, exerted on the impeller and ρ is fluid density. With $\Gamma_2 - \Gamma_1 = n\Gamma_{bp}$ this then gives

$$M = \frac{\rho Q n \Gamma_{bp}}{2\pi} \tag{1.182}$$

for radial flow impellers.

Next assuming 100% efficiency (or isentropic flow), so that the mechanical work ($M\Omega$) is transferred perfectly to the fluid, we obtain from the law of conservation of energy that the theoretically developed head (H_{th}) equals

$$H_{th} = \frac{n\Gamma_{bp}\Omega}{2\pi g} \tag{1.183}$$

where g is the acceleration due to gravity.

Then substituting (1.80) in (1.183) we get for radially bladed pump impellers

$$gH_{th} = \sigma_{p\Omega}(\Omega r_2)^2 - \frac{\sigma_{p\Gamma}\Gamma_1\Omega}{2\pi} \tag{1.184}$$

or, using dimensionless groups,

$$\Psi_{th} = \sigma_{p\Omega} - (r_1/r_2)^2\sigma_{p\Gamma}\Upsilon_1 \tag{1.185}$$

in which a head coefficient is introduced, defined by $\Psi_{th} = gH_{th}/(\Omega r_2)^2$; the volume flow rate coefficient (Φ), vortex coefficient (Υ_1), and slip factors are as given before.

Likewise, substituting (1.138) in (1.183) we obtain for pump impellers fitted out with logarithmic spiral blades

$$gH_{th} \sim \sigma_{p\Omega}(\Omega r_2)^2 + \frac{Q\tan(\beta) - \Gamma_1}{2\pi}\Omega \tag{1.186}$$

or, in dimensionless form,

$$\Psi_{th} \sim \sigma_{p\Omega} + \Phi\tan(\beta) - (r_1/r_2)^2\Upsilon_1 \tag{1.187}$$

as $\mu_\beta \rightarrow 0$.

Above-given formulae clearly illustrate the importance of slip factors. Based on (1.81), (1.82), and (1.139) we have plotted the respective slip factor in figure 1.13 for several numbers of blades and various blade angles. It shows that increasing the blade angle, as well as the number of blades, will give slip factors closer to the Eulerian value of unity. Consequently, this yields a larger (theoretical) head, as can be seen from the formulae given.

The graph plotted in figure 1.13(a) has been given before by Schulz (1928a, b) and Spannhake (1930), who both derived a solution similar to (1.82). Graphs similar to those of figures 1.13(b) and 1.13(c) have also been presented formerly, namely by Busemann (1928), who, however, obtained his results by numerical integration, considering a limited number of values for n and β only, whereas figures 1.13(b) and 1.13(c) are based on expressions in closed form, namely (1.81) and (1.139), enabling direct evaluation for each value of n and β.

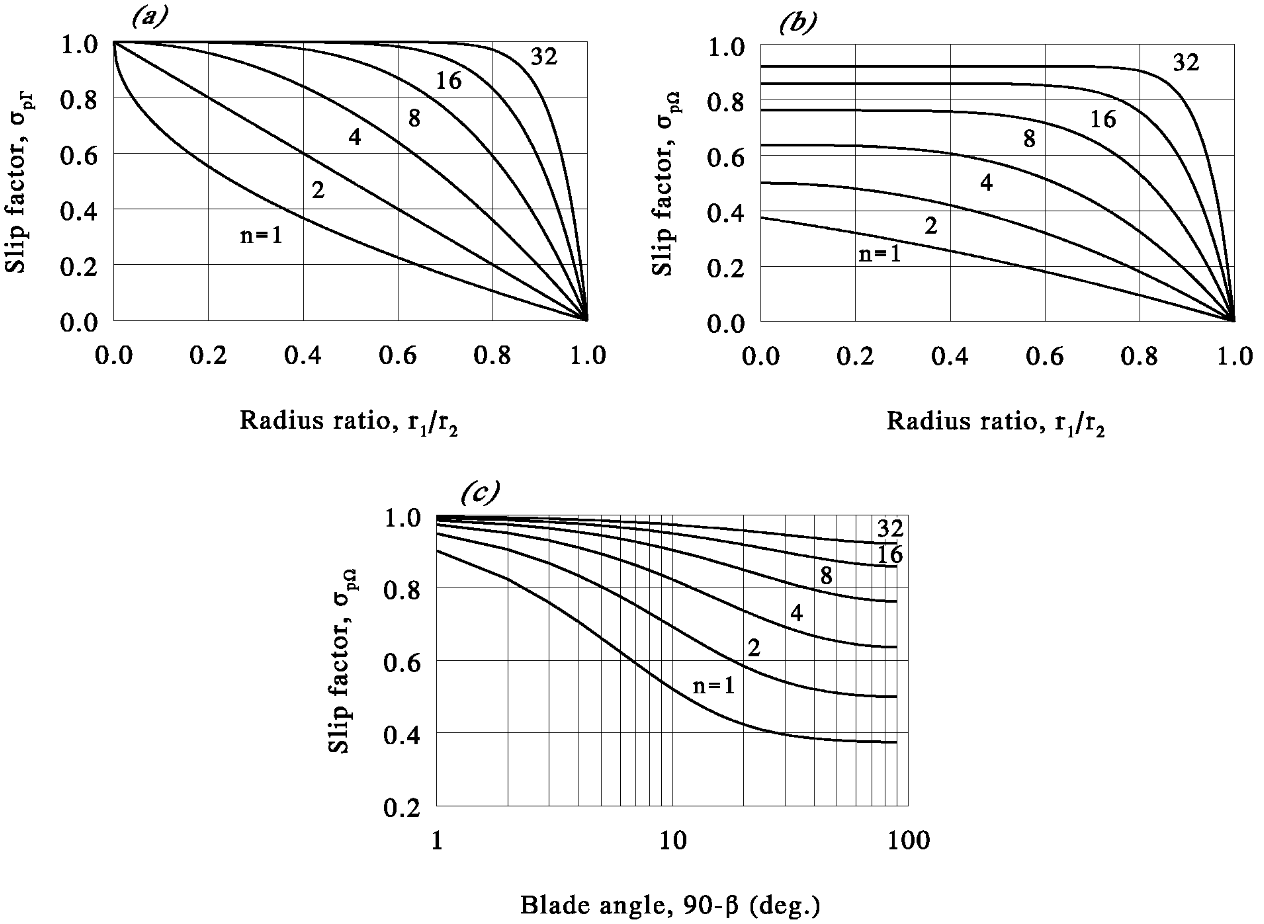

FIGURE 1.13. Slip factors for pump impellers: (a) $\sigma_{p\Gamma}$ for straight radial blades; (b) $\sigma_{p\Omega}$ for straight radial blades; (c) $\sigma_{p\Omega}$ for logarithmic spiral blades as $\mu_\beta \rightarrow 0$.

To illustrate (1.187) we have further plotted in figure 1.14 the head coefficient versus the volume flow rate coefficient for 60°, logarithmically bladed pump impellers with eight blades, receiving zero prerotation. In this figure we have also plotted the Eulerian head and the actual head as found form measurements (Elholm, Ayder & Braembussche 1992). The figure clearly shows the limiting effect of finite blade numbers. In particular, it shows that the theoretical head lies notably below the Eulerian head. The remaining difference between the theoretical and the actual head is due to friction losses, impact losses at impeller entrance, tip clearance, and off-design operation. The latter loss originates from the fact that the volute does not fit the impeller properly at off-design operation (§ 1.7.4). The impact losses can simply be reduced by giving the flow entering the impeller the correct prerotation or prewhirl, so that a shockless entry will be obtained.

Additionally, with reference to (1.187) we note that a critical value for the throughput in proportion to the angular speed (i.e. the volume flow rate coefficient Φ) can be determined, above which a centrifugal pump with backward-leaning blades (i.e. $\Omega < 0$) will not work as such, but as a turbine instead. This situation might occur if the suction or intake reservoir is located way above the discharge reservoir. For practical cases (i.e. $\sigma_{pQ} \sim 0$), assuming zero prewhirl, we obtain the critical value $\Phi_{crit} \sim \sigma_{p\Omega}\mathrm{cotan}(\beta)$ as $\mu_\beta \rightarrow 0$. (So, for instance, $n = 8$ blades and $\beta = 60°$ yields the condition $-\Phi < 0.46$.)

Lastly, completing the discussion of the subject, it should be noted that besides slip factors, like the ones just mentioned, another dimensionless group is often also seen in the

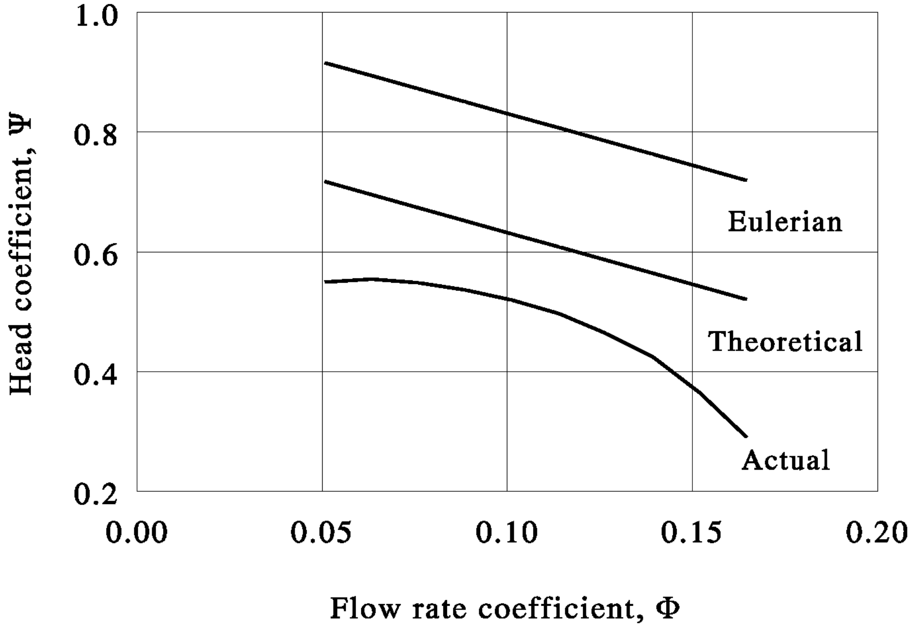

FIGURE 1.14. Head characteristic for 60°, logarithmically bladed pump with eight blades, having 100 mm outer radius, and receiving zero prerotation.

engineering of pumps and fans, namely the head reduction factor (HRF). This parameter is commonly defined as the ratio between the theoretical head and the Eulerian head. With (1.185) and (1.187) this gives for straight radial blades (i.e. HRF_{o}) and logarithmic spiral blades (i.e. HRF_β) respectively

$$HRF_{\mathrm{o}} = \frac{\sigma_{p\Omega} - (r_1/r_2)^2 \sigma_{p\Gamma} \Upsilon_1}{1 - (r_1/r_2)^2 \Upsilon_1} \tag{1.188}$$

and

$$HRF_\beta \sim \frac{\sigma_{p\Omega} + \Phi \tan(\beta) - (r_1/r_2)^2 \Upsilon_1}{1 + \Phi \tan(\beta) - (r_1/r_2)^2 \Upsilon_1} \tag{1.189}$$

as $\mu_\beta \to 0$.

Equation (1.189) indicates clearly that the head reduction factor is strongly flow-rate dependent, contrary to the concept of slip factors (which depend only on the geometric design of impellers); hence it is better to use slip factors. Note that the head reduction factor will be equal to the slip factor $\sigma_{p\Omega}$ in the special event of straight radial blades and zero prerotation, i.e. $\beta = 0$ and $\Upsilon_1 = 0$.

Furthermore, referring to (1.119), it is noted that

$$\left(\frac{\mathrm{Im}\{\chi\}}{\mathrm{Re}\{\chi\}}\right)^2 = \left(\frac{\sin(2\beta)/n}{1 + 2\cos^2(\beta)/n}\right)^2 \sim 0 \tag{1.190}$$

as $n \to \infty$, and, consequently, $B(\chi, \bar{\chi}) \sim B(\mathrm{Re}\{\chi\}, \mathrm{Re}\{\chi\}) = \{\Gamma(\mathrm{Re}\{\chi\})\}^2 / \Gamma(2\mathrm{Re}\{\chi\})$ as $n \to \infty$. Hence, the evaluation of $\sigma_{p\Omega}$ as given by (1.139) can then be simplified to

$$\sigma_{p\Omega} \sim \frac{1}{\pi^{\frac{1}{2}}} \mathrm{e}^{-2\beta \sin(2\beta)/n} \left(\cos(\beta)\right)^{-4\cos^2(\beta)/n} \frac{\Gamma(\frac{1}{2} + 2\cos^2(\beta)/n)}{\Gamma(1 + 2\cos^2(\beta)/n)} \tag{1.191}$$

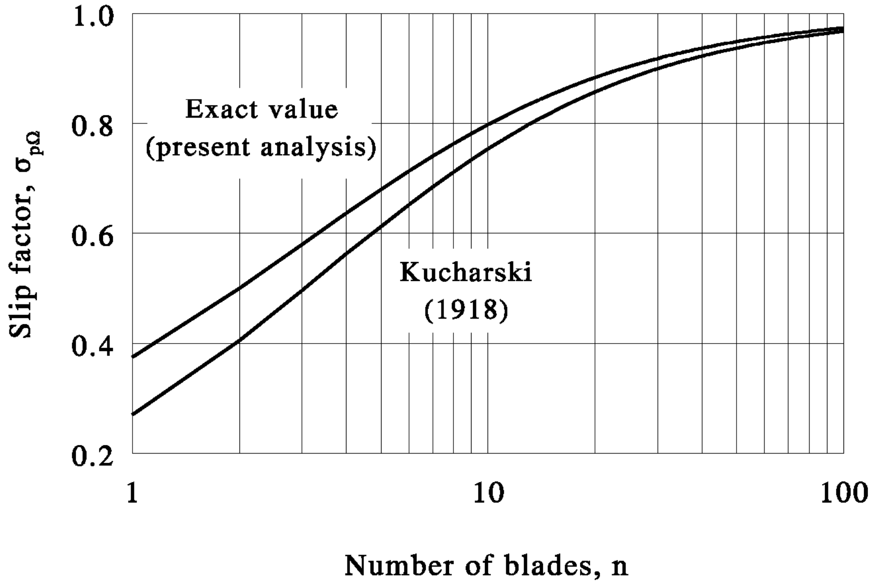

FIGURE 1.15. Slip factor $\sigma_{p\Omega}$ for pump impellers fitted out with straight radial blades as $\mu \to 0$, together with that according to Kucharski (1918).

as $n \to \infty$. Moreover, in the special case of straight radial blades (i.e. $\beta = 0$) (1.190) holds exactly, and, hence

$$\sigma_{p\Omega} \sim \frac{1}{\pi^{\frac{1}{2}}} \frac{\Gamma(\frac{1}{2} + 2/n)}{\Gamma(1 + 2/n)} \tag{1.192}$$

as $\mu \to 0$, for straight radial blades.

The asymptotic solution (1.192) is plotted in figure 1.15. In this figure we have also plotted the slip factor $\sigma_{p\Omega}$ according to Kucharski (1918), who has been the only one thus far to formulate solutions in closed form analytically (for $\sigma_{p\Omega}$). To that end Kucharski imposed that circular streamlines connected the trailing edges at zero throughput; a simple but remarkably good assumption.

Finally, it should be recognised that not only the references mentioned here, namely Kucharski (1918), Busemann (1928), Schulz (1928*a*, *b*) and Spannhake (1930), have explored the concept of slip occurring in radial impellers. A few others, partially reviewed by Wiesner (1967), have given approximate descriptions for rotational slip; their formulae, however, being mostly based on empiricism.

1.7.3 *Minimum volume flow rate coefficient*

Together with slip factors mentioned before, we might also have to take into account another, equally important, design parameter, namely the minimum volume flow rate coefficient Φ_m. This coefficient gives indirectly the lowest allowable throughput, so that there will be no reverse flow between impeller blades. Such reverse flow, expected to have a negative influence on pump performance, arises from the relative vorticity of the flow field, which is related directly to the displacement flow (§ 1.6.2).

From the respective conditions $w_r \geq 0$ and $w_s \geq 0$ for all radii, it follows that minimum volume flow rate coefficients for impellers with constant axial depth can be computed from

$$\Phi_m = \mathrm{MAX(MIN)}\left\{\frac{w^{\Omega}_{r(s)}}{\Omega r_2} R\cos(\beta)\right\} \tag{1.193}$$

This way we obtain from (1.106) and (1.147)

$$\begin{aligned}\Phi_m\left(n, \frac{r_1}{r_2}\right) &= \underset{-\pi<\theta<\pi}{\mathrm{MAX}}\ \mu^{-\frac{1}{2}+2/n}\left(\frac{2}{1+\mu^{\frac{1}{2}}}\right)^{4/n} \\ &\times\left\{2\{R(\theta)\}^n\sum_{k=1}^{\infty} a_k\sin(k\theta) + \tfrac{1}{2}(1-\mu)\sin(\theta)F\left(\frac{2}{n}, \frac{2}{n}; 1; \left(\frac{1-\mu^{\frac{1}{2}}}{1+\mu^{\frac{1}{2}}}\right)^2\right)\right\}\end{aligned} \tag{1.194}$$

for straight radial blades, and

$$\begin{aligned}\Phi_m(n, \beta) &\sim \underset{-\pi-2\beta<\theta<\pi-2\beta}{\mathrm{MAX(MIN)}}\ \tfrac{1}{2}\{R(\theta)\}^2\sin(2\beta) - (\cos(\beta))^{1-4\cos^2(\beta)/n}\,\mathrm{e}^{-2\beta\sin(2\beta)/n} \\ &\times\mathrm{cotan}(\beta+\tfrac{1}{2}\theta)\left\{\frac{\sin(2\beta+\frac{1}{2}\theta)}{\cos(\beta+\frac{1}{2}\theta)}\sum_{k=1}^{\infty}B_k\sin(k\theta+2k\beta) - \frac{n}{2\cos(\beta)}\sum_{k=1}^{\infty}kC_k\sin(k\theta+2k\beta)\right\}\end{aligned} \tag{1.195}$$

as $\mu_\beta \to 0$, for logarithmic spiral blades, where MAX(MIN) has to be interpreted as MAX if $\Omega > 0$ and as MIN if $\Omega < 0$; the respective dimensionless radii, $R(\theta)$, are given by (1.11) and (1.21) for straight radial and logarithmic spiral blades respectively.

Additionally, putting $\beta = 0$ we readily obtain form (1.195)

$$\Phi_m(n) \sim \underset{-\pi<\theta<\pi}{\mathrm{MAX(MIN)}}\ 2^{1-4/n}\Gamma(1+4/n)\sum_{k=1}^{\infty}\frac{\sin(k\theta)}{\Gamma(1+k+2/n)\Gamma(1-k+2/n)} \tag{1.196}$$

as $\mu \to 0$, for straight radial blades, which may also be derived directly using (1.89).

The outcome of (1.195) and (1.196) is presented graphically in figure 1.16, where figure 1.16(*b*) also shows the minimum volume flow rate coefficient as derived by Kucharski (1918). The figure clearly shows the positive effect of curvature; increasing the blade angle and the number of blades will give lower-valued minimum volume flow rate coefficients. Logically, the graphs of figure 1.16 can be used either to determine the lowest allowable throughput or the minimum number of blades and the blade angle required, so that reverse flow is avoided.

The results given above are appropriate for radial impellers with constant axial depth (say, b). Numerous impellers in practice, however, have a non-constant – with increasing radius declining – axial depth (i.e. $\mathrm{d}b/\mathrm{d}r < 0$), so that a gentle flow deceleration in the impeller passages can be achieved. For these non-constant axial depth cases, minimum volume flow rate coefficients may be derived from the preceding results too, in the following manner.

In general, to avoid reverse flow, we have (to fulfil) the condition

$$w^Q \geq w^{\Omega} \tag{1.197}$$

With $w^Q = Q_v/(2\pi rb)$ and $\Phi = Q_v/(2\pi\Omega r_2^2 b_2)$, where Q_v is the volume flow rate and b_2 is the axial depth at impeller discharge, this becomes

$$\frac{\Phi}{\cos(\beta)}\frac{b_2 r_2}{br} \geq \frac{w^{\Omega}}{\Omega r_2} \tag{1.198}$$

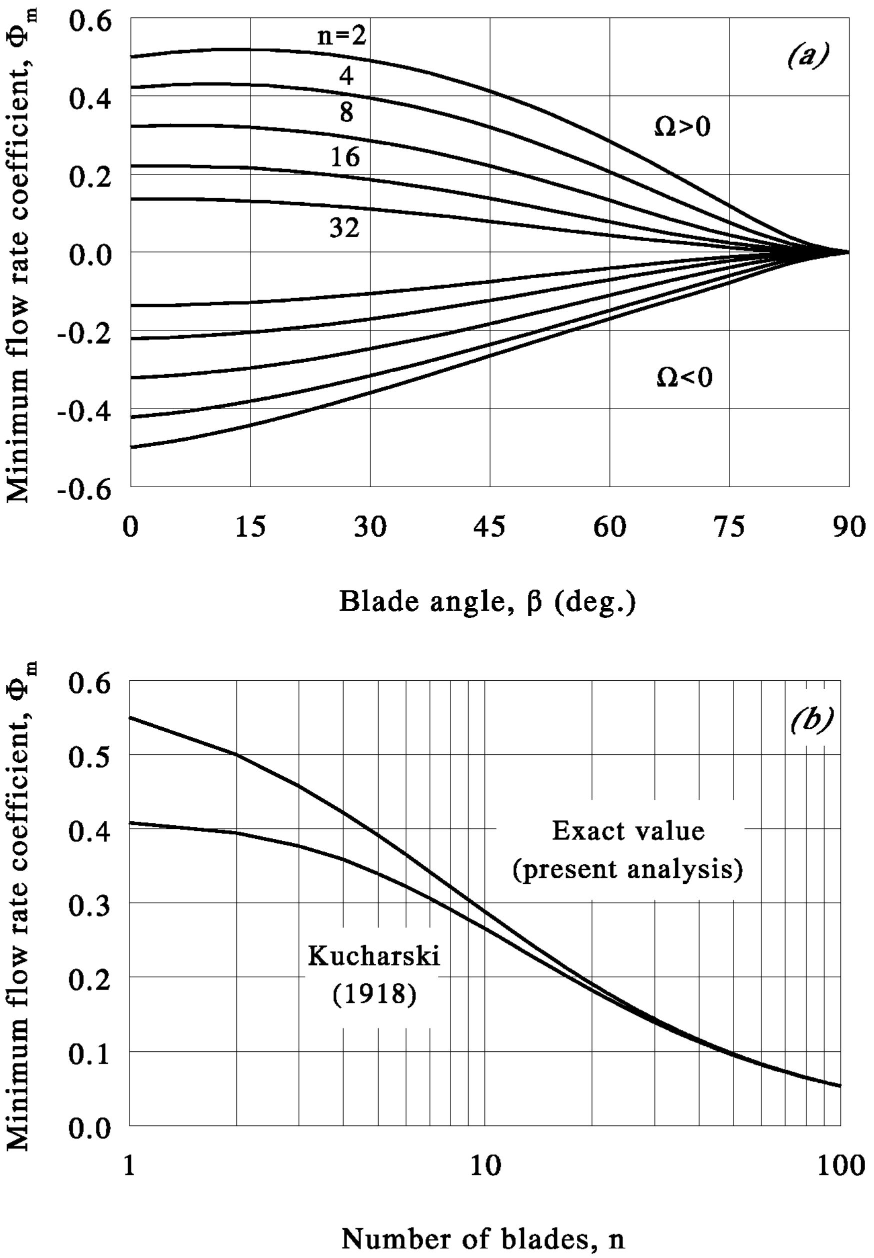

FIGURE 1.16. Minimum volume flow rate coefficient for pump impellers as $\mu_\beta \to 0$: (*a*) logarithmic spiral blades; (*b*) straight radial blades.

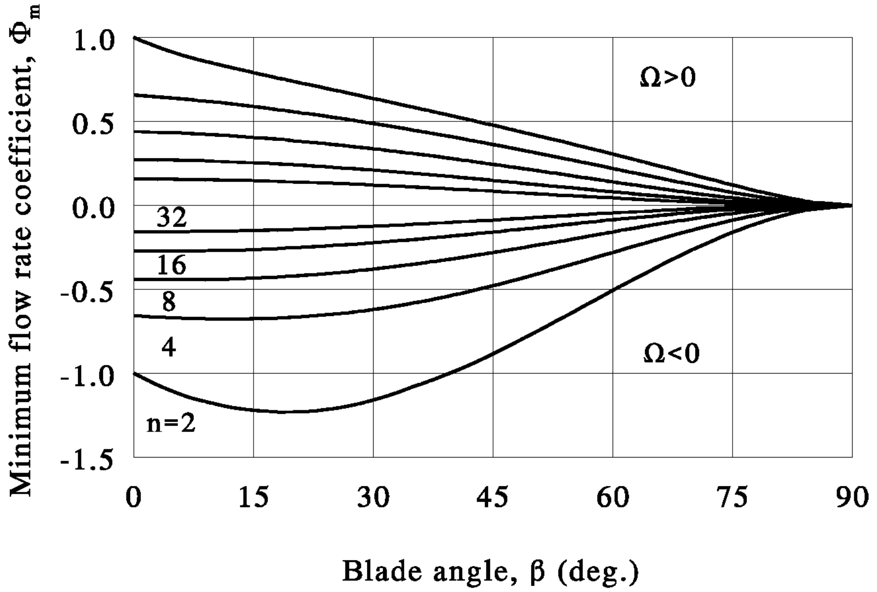

FIGURE 1.17. Minimum volume flow rate coefficient for pump impellers with non-constant, $\mathrm{d}(br)/\mathrm{d}r = 0$, axial depth as $\mu_\beta \to 0$.

For constant axial depth (i.e. $b = b_2$) this condition readily yields (1.193). For non-constant axial depth the outcome strongly depends on $b = b(r)$, and a general result is therefore hard to produce. However, a highly representative case of non-constant axial depth is br = constant, yielding constant throughput velocity w^Q. This particular case will be discussed in some further detail.

For br = constant we first obtain from (1.198) that

$$\Phi_m = \mathrm{MAX(MIN)}\left\{\frac{w^\Omega}{\Omega r_2}\cos(\beta)\right\} \tag{1.199}$$

Then, to compute Φ_m we may approximate by employing the formula for the displacement flow given before (i.e. the one appropriate for strict two-dimensional flow) since the displacement flow velocity (w^Ω) in the case of non-constant axial depth is nearly equal to the constant axial depth value. The declining axial depth primarily influences the throughput velocity w^Q. (This has also been corroborated by several numerical tests, that is finite element method based impeller passage flow calculations). The expression that we then find reads

$$\begin{aligned}\Phi_m(n,\beta) \sim \underset{-\pi-2\beta<\theta<\pi-2\beta}{\mathrm{MAX(MIN)}}\ & \tfrac{1}{2}R(\theta)\sin(2\beta) - \{R(\theta)\}^{-1}(\cos(\beta))^{1-4\cos^2(\beta)/n}\,\mathrm{e}^{-2\beta\sin(2\beta)/n} \\ \times \operatorname{cotan}(\beta+\tfrac{1}{2}\theta) & \left\{\frac{\sin(2\beta+\frac{1}{2}\theta)}{\cos(\beta+\frac{1}{2}\theta)}\sum_{k=1}^{\infty}B_k\sin(k\theta+2k\beta) - \frac{n}{2\cos(\beta)}\sum_{k=1}^{\infty}kC_k\sin(k\theta+2k\beta)\right\}\end{aligned} \tag{1.200}$$

as $\mu_\beta \to 0$.

The outcome of (1.200) is plotted in figure 1.17. Again we clearly observe the positive effect of increasing the number of blades and the blade curvature. The graph, like the one of figure 1.16 being appropriate for the case of constant axial depth impellers, can be used either to determine the minimum allowable throughput or to compute the minimum number of blades and the blade curvature required to avoid reverse flow, for radial impeller

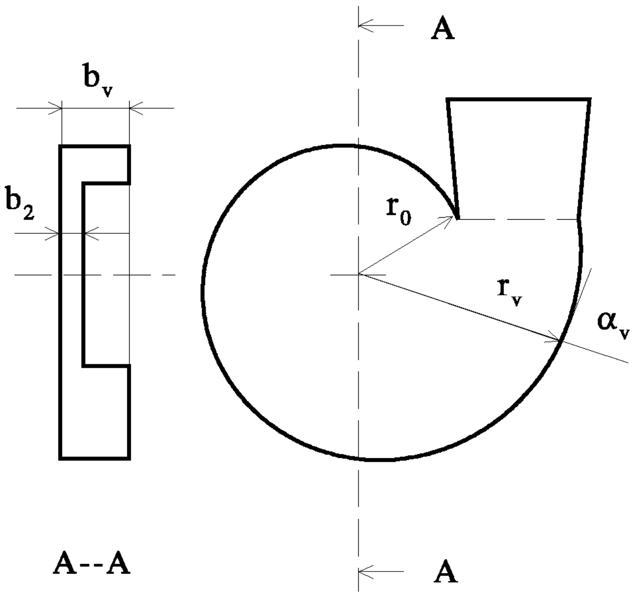

FIGURE 1.18. Logarithmically curved volute.

with non-constant (that is, br = constant) axial depth.

1.7.4 *Choice of volute*

The findings obtained so far for isolated (unbounded) impellers allow us also to make suggestions about volutes housing pump impellers. To that end we will adapt so-called logarithmically curved volutes, the curvature of which is, like a logarithmic spiral blade, simply described by (see also figure 1.18)

$$r(\phi) = r_0 \mathrm{e}^{(\phi-\phi_0)/\tan(\alpha_v)} \tag{1.201}$$

or

$$\phi(r) = \phi_0 + \tan(\alpha_v)\ln(r/r_2) \tag{1.202}$$

where α_v is the volute angle, ϕ_0 is an offset angle, and $r_0 = r(\phi_0)$.

To determine the volute angle α_v we employ the fact that a flow discharged from an unbounded impeller has logarithmic spiral streamlines. In consequence, we may compute the volute angle from the circulation/flux ratio of the discharge flow. With reference to figure 1.18 it thus follows that

$$\tan(\alpha_v) = b_v \mathit{\Gamma}_2/(b_2 Q) \tag{1.203}$$

where b_v/b_2 is the depth ratio of the volute.

Next, using (1.46) and substituting respectively (1.80) and (1.138), we obtain from (1.203), employing a dimensionless notation

$$\tan(\alpha_v) = \frac{\sigma_{p\Omega} - (1-\sigma_{p\Gamma})\Upsilon_1}{\Phi}\frac{b_v}{b_2} \tag{1.204}$$

for straight radial blades, and

$$\tan(\alpha_v) \sim \left(\frac{\sigma_{p\Omega}}{\Phi} + \tan(\beta)\right)\frac{b_v}{b_2} \tag{1.205}$$

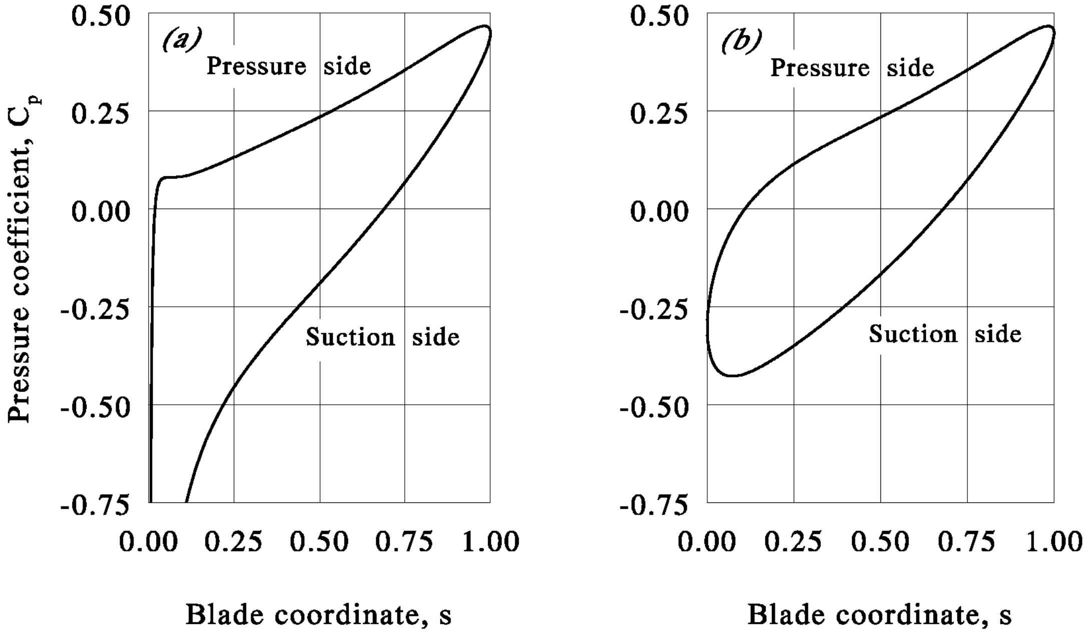

FIGURE 1.19. Pressure distribution along straight radial blades of eight-bladed impellers with inlet-to-outlet radius ratio of 0.37 ($\Phi_m = 0.319$; $\Upsilon_{1s} = 0.214$): (a) minimum volume flow rate and zero prerotation; (b) minimum volume flow rate and shockless entry.

as $\mu_\beta \rightarrow 0$, for logarithmic spiral blades.

Relations (1.204) and (1.205) provide simple means to compute appropriate volute angles α_v. The depth ratio b_v/b_2 gives the possibility of constructing small volutes, since at unit depth ratio, i.e. $b_v/b_2 = 1$, most volutes would become excessively large. Alternatively, to avoid large volutes, it is possible to use more than one exhaust, since Φ will be reduced inversely proportionally to the number of exhausts (say n_{ex}, so that $\Phi \propto 1/n_{ex}$). In addition, increasing the number of exhausts also improves the symmetry and periodicity of the volute flow.

Furthermore, (1.204) and (1.205) distinctly show that a particular volute will be suited for one operating point only, and, moreover, that the influence of a finite number of blades is incorporated through the appearance of slip factors. Consequently, volutes for finitely bladed impellers have to have larger volute angles than those designed according to one-dimensional Eulerian flow theory, where no account is taken of the occurrence of slip and, hence, circumferential fluid velocities are taken too large.

1.7.5 *Pressure distribution along impeller blades*

In the engineering of turbomachinery the pressure distribution along impeller blades plays a significant role. In particular, forces exerted on impellers, blade loading (in terms of a pressure difference), and cavitation are of interest.

The pressure distribution along the blades of radial impellers can be computed swiftly from the velocity distribution, using Bernoulli's theorem for steady two-dimensional fluid motions with respect to rotating axes; provided of course that the conditions of steadiness and two-dimensional flow are fulfilled. Neglecting body forces, the theorem may be stated

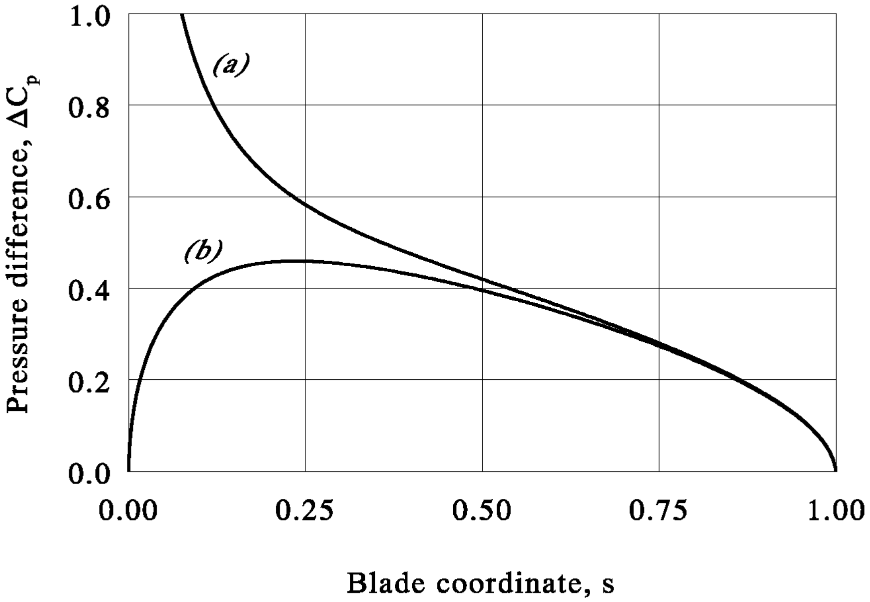

FIGURE 1.20. Pressure difference over straight radial blades of eight-bladed impellers with inlet-to-outlet radius ratio of 0.37 ($\Phi_m = 0.319$; $\Upsilon_{1s} = 0.214$): (a) minimum volume flow rate and zero prerotation; (b) minimum volume flow rate and shockless entry.

as (see for instance Batchelor 1967, p. 396, or Prandtl 1963, p. 347)

$$p/\rho + \tfrac{1}{2}w^2 - \tfrac{1}{2}(\Omega r)^2 = \text{constant} \tag{1.206}$$

in which p is the thermodynamic pressure and ρ is the fluid density.

Introducing dimensionless groups, (1.206) can be written alternatively as

$$C_p + \tfrac{1}{2}C_w^2 - \tfrac{1}{2}R^2 = \text{constant} \tag{1.207}$$

where $C_p = p/(\rho\Omega^2 r_2^2)$, $C_w = w/(\Omega r_2)$ and $R = r/r_2$.

Based on the velocity distributions of figures 1.5(c) and 1.5(d) we have plotted in figures 1.19(a) and 1.19(b) the pressure coefficient C_p versus the blade coordinate s, where we have put the (Bernoulli) constant equal to zero for convenience; the blade coordinate $s \in [0,1]$, employed before, is related to the dimensionless radius R by $R = s+(1-s)r_1/r_2$.

Figure 1.19 demonstrates that the blade loading is concentrated near the inner tip, that is the pressure difference ($\Delta C_p = C_p^+ - C_p^-$) over a blade has its maximum near the inner tip. This phenomenon is even better reflected in figure 1.20, where we have plotted the pressure difference as a function of the blade coordinate.

Also, to illustrate the positive influence of blade curvature with respect to the blade loading, we have computed the pressure distribution along logarithmic spiral blades, based on the velocity distribution of figure 1.8, with the respective minimum volume flow rate required superposed. The resulting pressure distributions and pressure differences are given in figures 1.21 and 1.22 respectively. The figures clearly indicate that blade curvature affects the blade loading favourably. Furthermore, we see that there is zero loading at the trailing edge, which is, of course, a logical consequence of the imposition of the Kutta condition. (This is also why the Kutta condition is occasionally addressed as the condition of no load.)

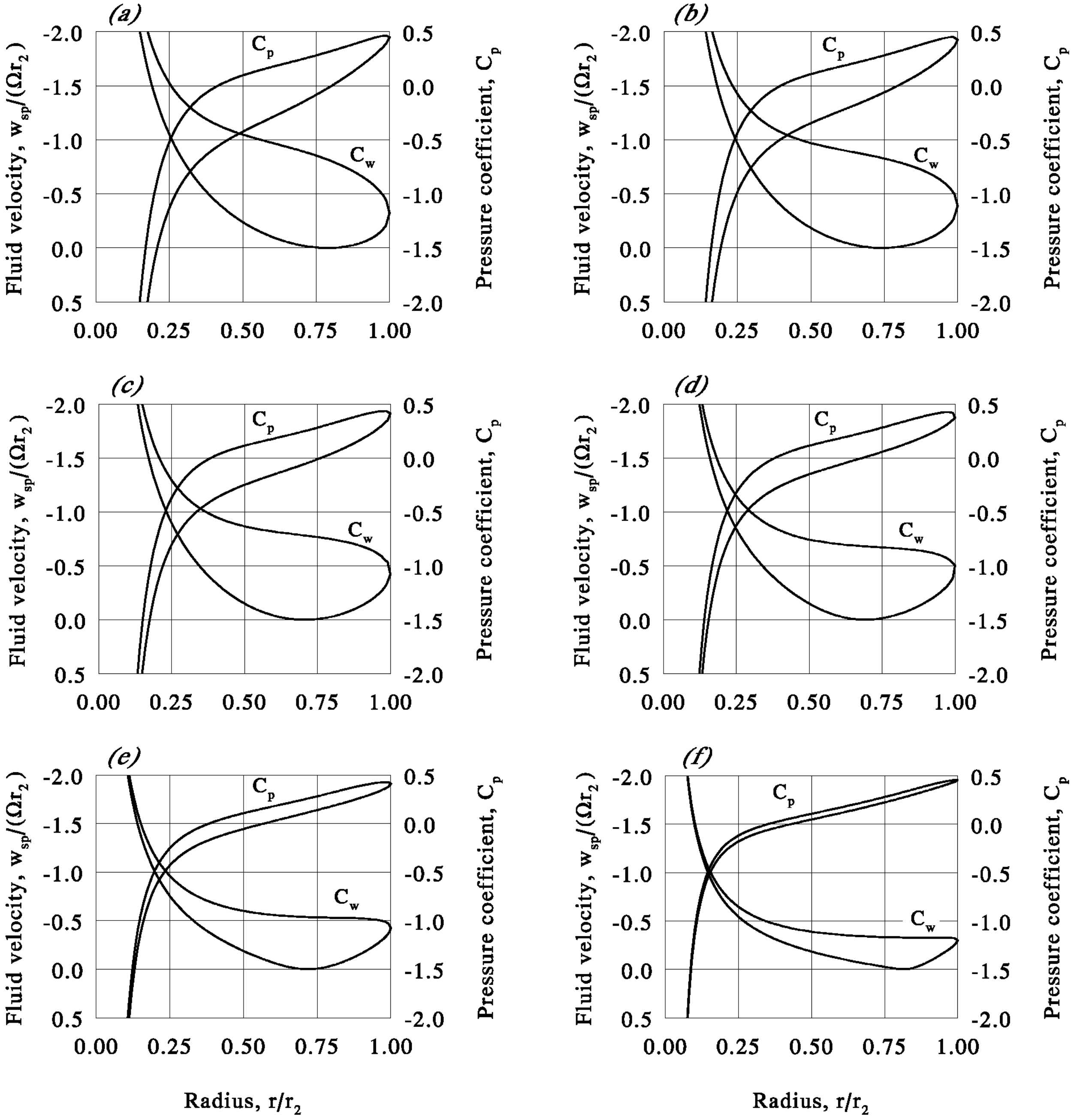

FIGURE 1.21. Pressure (C_p) and velocity (C_w) distribution at minimum volume flow rate, along backwardly curved ($\Omega < 0$) logarithmic spiral blades of eight-bladed impellers as $\mu_\beta \to 0$. (a) $\beta = 0$; (b) $\beta = 15°$; (c) $\beta = 30°$; (d) $\beta = 45°$; (e) $\beta = 60°$; (f) $\beta = 75°$.

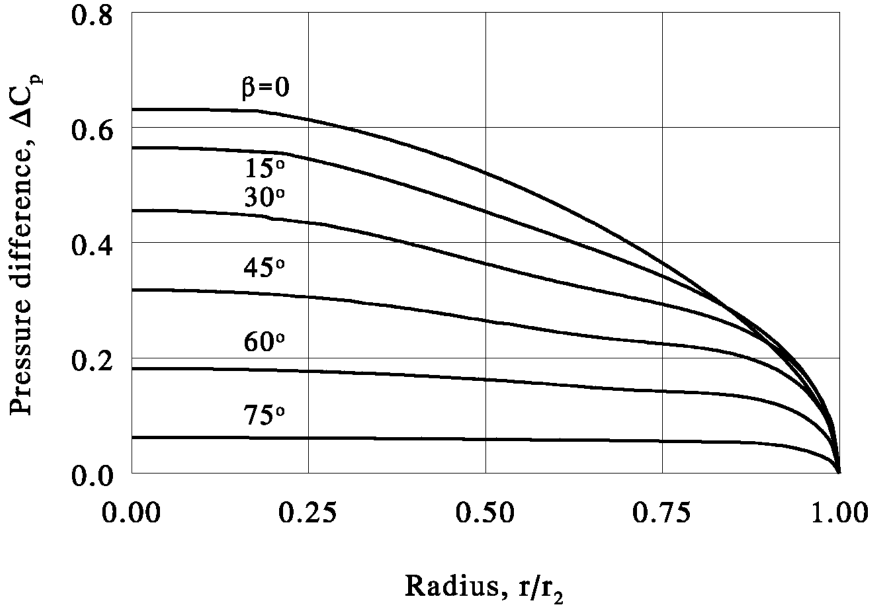

FIGURE 1.22. Pressure difference at minimum volume flow, over backwardly curved ($\Omega < 0$) logarithmic spiral blades of eight-bladed impellers as $\mu_\beta \to 0$.

1.8 Analytical expressions for impeller design parameters: Turbine Impellers

Besides analytical expressions for parameters that govern the performance of radial-flow pumps (§ 1.7), we are also in the position to derive relations appropriate for radial inward-flow turbines. Successively, we will focuss attention on: delivered work and condition of shockless entry, minimum volume flow rate to avoid reverse flow between the blades, and dimensions required for impeller housing.

.

1.8.1 *Delivered work and condition of shockless entry*

Employing Euler's turbine equation, e.g. (1.181), it readily follows that the amount of work (P_{th}) theoretically delivered by two-dimensional isolated (unbounded) hydraulic radial inward-flow turbine impellers is given by

$$P_{th} = \rho Q \Omega \frac{\Gamma_2}{2\pi} - \rho Q \Omega \frac{\Gamma_1}{2\pi} \qquad (1.208)$$

Here, the outer circulation Γ_2 represents the prerotation or prewhirl. This prewhirl strongly determines the work to be delivered by radial inward-flow turbine impellers. The inner circulation Γ_1, being related directly to the angular momentum of the fluid at blade inner radius, is merely to be seen as a residual or loss of energy. In practice, however, modern turbine impellers are designed in such a way that this loss of momentum is avoided. This is achieved by curving the impeller blades backwardly at the inner radius, or by deviating the flow axially at the impeller inner region and curving the blades appropriately. Although the current two-dimensional analysis is unsuited to specify the blade shapes required at the impeller inner region to accomplish this, in line with practice we set the second term in (1.208) equal to zero, so that

$$P_{th} = \rho Q \Omega \Gamma_2 / 2\pi \qquad (1.209)$$

Furthermore, to avoid impact losses, turbine impellers are usually operated at shockless entry. The prerotation or prewhirl Γ_{2s} then required is prescribed by (1.103), which yields, after substitution in (1.209), for the amount of work delivered at shockless entry

$$P_{th,s} = \tau_t \rho Q \Omega^2 r_2^2 \tag{1.210}$$

in which the prerotation factor (τ_t) is prescribed by (1.105), which can be expanded asymptotically for the limiting case of $\mu^{\frac{1}{2}} \to 0$, yielding

$$\tau_t \sim \frac{1}{\pi^{\frac{1}{2}}} \frac{\Gamma(\frac{1}{2} + 2/n)}{\Gamma(1 + 2/n)} \tag{1.211}$$

as $\mu^{\frac{1}{2}} \to 0$.

Equation (1.211) provides a simple expression to compute the prerotation required for shockless entry. Figure 1.23(*b*) shows this prerotation factor as function of the number of blades. The exact value according to (1.105) is plotted in figure 1.23(*a*). Differences between the exact value and asymptotic expansion (1.211) of τ_t, as depicted on the graphs of figure 1.23, reflect the influence of the centre configuration of turbine impellers on the prerotation required to obtain shockless entry at impeller entrance.

In practice, as stated before, blades of radial inward-flow turbine impellers are usually curved at the centre or (turbine) impeller discharge region. As long as this interior part is located in a region of radial extent r_1 such that μ is small, this section is not likely to have much influence on the condition of shockless entry, or on the flow in the impeller entrance region where the blades are actually straight. In that case (1.211) can be applied well to assess the condition of shockless entry.

Lastly, it is noted that the asymptotic expansion of the prerotation factor for shockless entry in radially bladed turbine impellers as given above resembles the slip factor $\sigma_{p\Omega}$ for radially bladed pump impellers as $\mu \to 0$. Likewise, for a finite number of blades it is smaller than unity, reflecting the remarkable fact – never before noticed (to the author's knowledge) – that for shockless entry the prewhirl of the flow should be less than the one-dimensional Eulerian value derived from the circumferential velocity at the outer blade radius.

1.8.2 *Minimum flow coefficient*

Since (1.194) and (1.196) are also valid for radially bladed turbine impellers, it directly follows that the minimum volume flow rate coefficient for radially bladed pump and turbine impellers will be identical. Hence, figure 1.16(*b*) is appropriate for both type of impellers as $\mu^{\frac{1}{2}} \to 0$. The only difference is that the turbines considered are characterised by radial inward flow, i.e. $Q < 0$, whereas pumps have radial outward flow, i.e. $Q > 0$.

When the throughput lies below the volume flow rate minimally required, both turbines and pumps will have reverse flow areas to the pressure side of the blades, located near the outer tip. Logically, this position results from the fact that the throughput velocity is inversely proportional to the radius.

Furthermore, reverse flow will also occur at the leading edge of the blades when the condition of shockless entry is not fulfilled. This is entirely due to the singular behaviour of the velocity profile near the leading edge; see also figures 1.7(*a*) and 1.7(*c*).

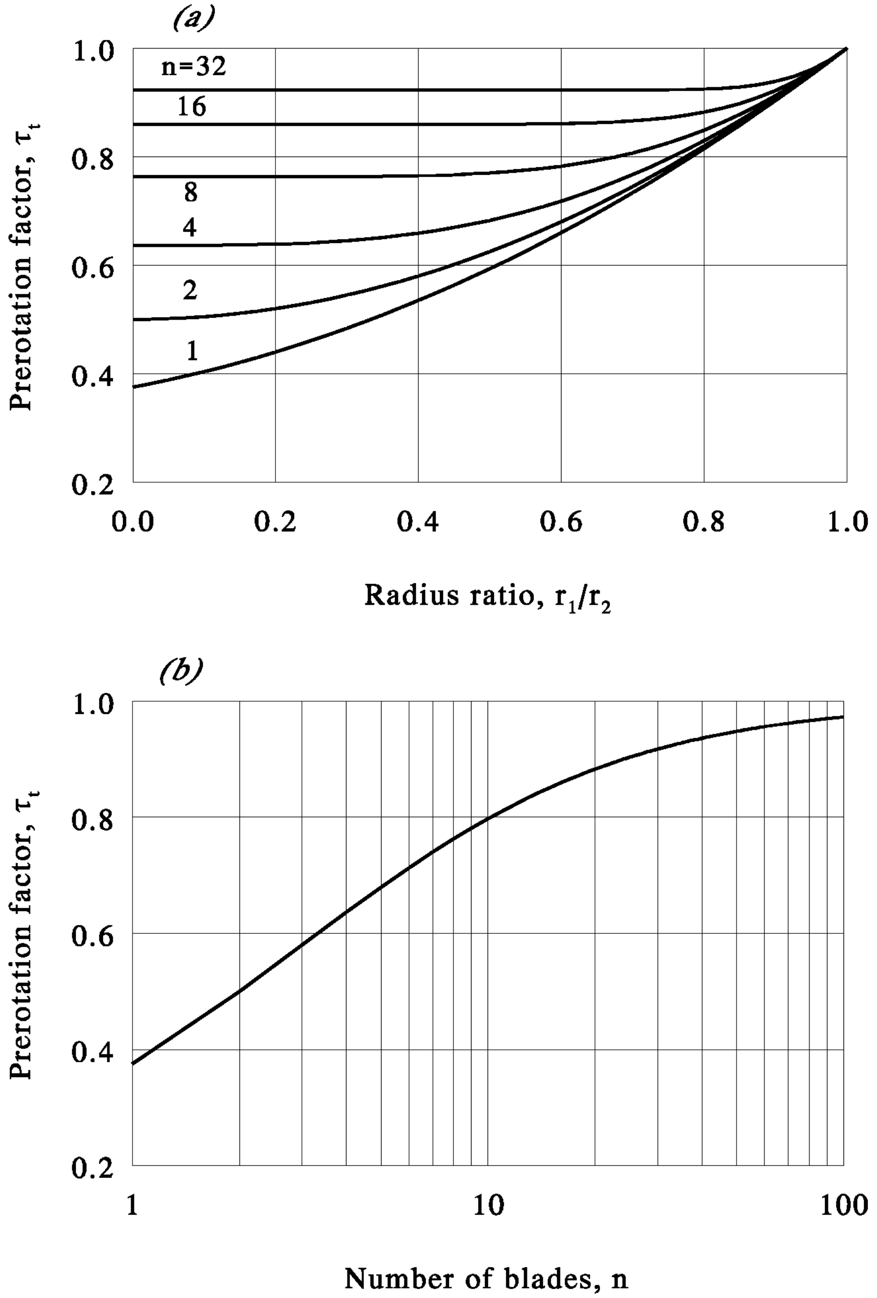

FIGURE 1.23. Prerotation factor for radially bladed turbine impellers: (*a*) exact value; (*b*) asymptotic solution as $\mu^{\frac{1}{2}} \to 0$. Note that the values for τ_t at $r_1/r_2 = 0$, given in (*a*), are equal to the values of τ_t in (*b*).

1.8.3 *Impeller housing*

Assuming a logarithmically spiralled housing, fitted with inlet guide vanes if so desired, we may adopt (1.203) to compute the dimensions of turbine impeller volutes. Employing dimensionless groups we then get (see also figure 1.18)

$$\tan(\alpha_v) = \frac{b_v \varUpsilon_2}{b_2 \varPhi} \tag{1.212}$$

At shockless entry, i.e. $\varUpsilon_2 = \tau_t$, which is usually desired, this becomes

$$\tan(\alpha_v) = \frac{b_v \tau_t}{b_2 \varPhi} \tag{1.213}$$

These relations provide a simple means to compute the curvature of radial inward-flow turbine impeller housings, so that the flow will be given the appropriate prerotation. Furthermore, it is clearly shown by both equations that a particular housing will fit one volume flow rate only—particularly since the prerotation factor τ_t is determined completely by the design of the impeller.

1.9 Concluding remarks

In the foregoing the irrotational and solenoidal flow in two-dimensionally modelled, radial-flow impellers fitted out with equiangular blades has been analysed in detail. The general approach, including some features of the method of conformal mapping, as well as some of the intermediate or partial results presented, agrees with the works of, notably, Kucharski (1918), Spannhake (1925*a*, *b*, 1930), Busemann (1928), Acosta (1954), and Sörensen (1927, 1941). However, by extending the mathematical analysis, a number of new and previously unpublished results have been derived. These include exact solutions for the velocity distribution along impeller blades of radially bladed pump and turbine impellers, and solutions which hold asymptotically for logarithmically bladed pump impellers as $(r_1/r_2)^{n/\cos(\beta)} \to 0$, where r_1 is the impeller inner radius, r_2 is the impeller outer radius, n is the number of blades, and β is the angle of blade curvature. The respective solutions have been formulated in closed form, involving Fourier series with Fourier coefficients given by the Gauss hypergeometric function and beta function respectively.

Based on the respective velocity distributions, new or improved expressions have been derived for parameters that are important for practical design of radial turbomachinery, and which reflect the two-dimensional nature of the flow field. In particular, expressions have been given for rotational slip of the flow discharged from radial impellers, as well as for (avoidance of) reverse flow between impeller blades and shockless flow at impeller entry, with the number of blades, blade curvature, and blade revolution as determinable variables. Furthermore, analytical extensions to classical one-dimensional Eulerian expressions for the developed head of pumps and delivered work of turbines have been given.

Apart from the applications to design, the results can also serve as a practical reference for complex two- and quasi-three-dimensional, time-dependent, numerical potential flow calculations (Badie 1993, van Essen 1995). Moreover, they provide a well-defined starting point for further investigation (chapter 2) of the real-fluid flow behaviour in radial-flow impellers, such as experimental observation of situations of near stagnation flow along the pressure side of impeller blades, as well as boundary layer calculations along the blade surfaces—on the basis of the potential-flow solutions given here for the core-flow tangential velocity distributions.

Chapter 2

Fluid flow in rotating low-specific-speed centrifugal-pump impeller passages [*]

Abstract. *Experiments on blade passage flows in model centrifugal pump impellers of low specific speed, that are rotating at a steady rate, are described. Using a custom-designed two-component laser-Doppler-velocimetry flow measurement system, capable of making immediate measurements in the rotor frame of reference, the radial and circumferential velocity components of the relative flow inside the impeller passages were measured, and from these measurements the streamwise passage velocity was computed. Measurements were taken from blade to blade in three 60°, logarithmically bladed impellers with five, nine, and fifteen blades respectively. Supplementary to the laser-Doppler-velocimetry flow measurements, particle-image flow visualisations and video-based image analyses were performed to expose some of the flow field characteristics caused by spanwise (system) rotation.*

The indirectly measured streamwise passage velocity was compared to the solution of the impeller passage flow velocity that holds asymptotically in a region well away from the blade tips. Additional potential-flow finite-element calculations were used for comparison for those regions where the asymptotic expansion does not hold. The agreement between the experimental and theoretical values appeared to be excellent for the core flow region, which extended from the blade pressure side to the viscous boundary layer layer at the blade suction side. The calculation of the boundary layer development along the suction side of the impeller blades was of particular interest, since – contrary to the blade pressure side – only there a significant departure from inviscid flow behaviour was observed. Calculations performed in the ordinary fashion, i.e. employment of the common thin-shear-layer approximation, substantiated the conception that for low-specific-speed impellers the effects of spanwise rotation and (modest) surface curvature are accommodated (for the larger part) in the description of the inviscid core flow. Furthermore, actual (overall) impeller performance was considered in terms of periphery circulation.

2.1 Introduction

This chapter represents the experimental counterpart of the theory described in chapter 1. Using non-invasive optical measurement techniques, the flow of water in three shrouded models of low-specific-speed centrifugal pump impellers of simple two-dimensional design was studied. These test impellers, as well as the casing geometry, were chosen in con-

---

[*] Parts of this chapter have been published in Visser & Jonker (1995*a*, *b*).

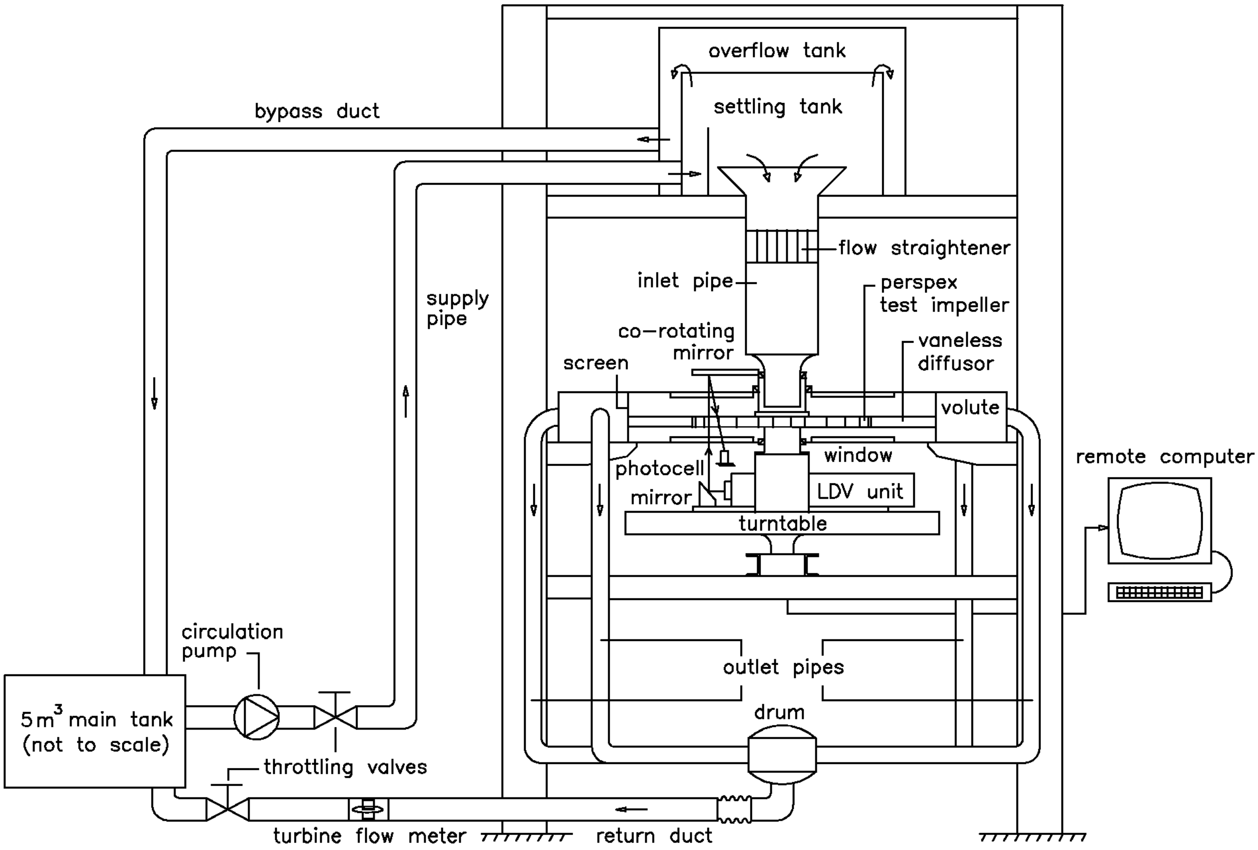

FIGURE 2.1. Diagram of impeller passage flow apparatus: LDV set-up.

formity with the theoretical model to enable clarification of the essentials of fluid flow in low-specific-speed centrifugal (pump) impellers through immediate comparison with the corresponding calculations. The test impellers were all three equipped with 60° logarithmic spiral blades, while the number of blades equalled five, nine, and fifteen.

The study of fluid flow in centrifugal-impeller passages, in particular by experiment, has interested many hydrodynamicists before, who – in broad outline – wished to gain insight or validate calculations in order to predict and improve (prediction of) impeller performance. The first experimental effort of note in this field was conducted by Uchimaru (1925), who reported measurements of the pressure distribution (in water) inside the passage of a rotating centrifugal impeller. More widely known, however, is the early experimental study of Fisher & Thoma (1932), who visualised the flow in a rotating impeller using dye injection while water was the working fluid. Other noteworthy visualisation studies on impeller passage flows are those of Fister (1966), who employed a spark-tracer method to visualise the flow in radial-flow compressor impeller passages, and Lennemann & Howard (1970), who utilised a hydrogen-bubble visualisation technique to investigate the flow in centrifugal-pump impeller passages running at part-capacity. Detailed *quantitative* impeller passage flow measurements were first reported by Fowler (1968), who quantified the air velocity in a single, rotating, radial diffuser channel by hot-wire anemometry, and also visualised the boundary layer by injecting damp ammonia (to stain ordinary printing paper). Experiments quite similar to those of Fowler (hot-wire anemometry, rotating radial-flow passage) were also conducted by Moore (1973). Howard & Kittmer (1975) focussed attention on the flow of water in shrouded and unshrouded impeller configurations, and used a hot-film measurement technique (miniature probe). Utilisation of the

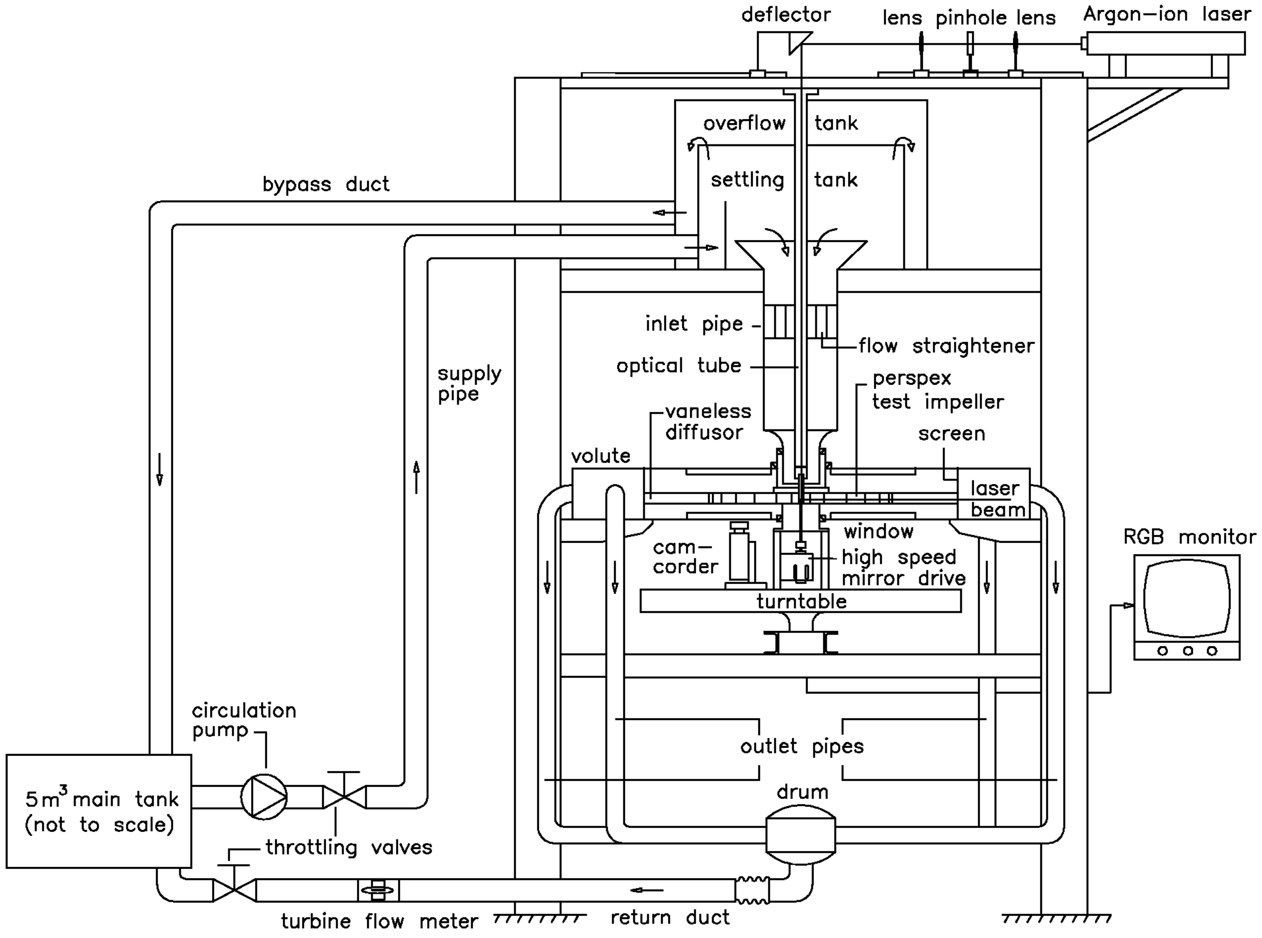

FIGURE 2.2. Diagram of impeller passage flow apparatus: PIV set-up.

non-invasive laser-Doppler-velocimetry flow measurement technique has been reported by Miner, Beaudoin & Flack (1989), and Abramian & Howard (1994*a*, *b*), who obtained their respective results by measuring from the fixed (non-rotating) laboratory frame of reference. Essentially, Miner, Beaudoin & Flack used a rotor-shaft encoder disk to label the (two-component) velocity measurements once the measurement result was checked to be valid, whereas Abramian & Howard were capable of measuring in the rotor frame of reference through the use of derotator optics.

The experimental (passage-flow-measurement) results of the current work were all obtained from the rotor frame of reference, without the employment of derotator optics or rotor-shaft encoder (trigger) devices. The fluid flow in the rotating impeller passages was investigated using a custom-designed co-rotating two-component laser-Doppler velocimeter, supplemented by sweep-beam laser-sheet flow visualisations and digital image analyses (also conducted with respect to the rotating frame). Employment of equipment capable of measuring directly in the rotor frame of reference enabled immediate comparison of experimental and theoretical results and, moreover, provided clear pictures of the flow patterns with respect to the rotating frame of reference. The measurements verified the potential-flow behaviour of the core flow inside the passages, and exposed a substantial boundary-layer development on the suction side of the blades, which could be calculated by a direct-hierarchy approach. The boundary layer on the blade pressure side was seen to be of a next-to-zero thickness that could not be computed by a direct-hierarchy approach; future study has to show if a no-hierarchy (triple-deck) approach will yield proper results

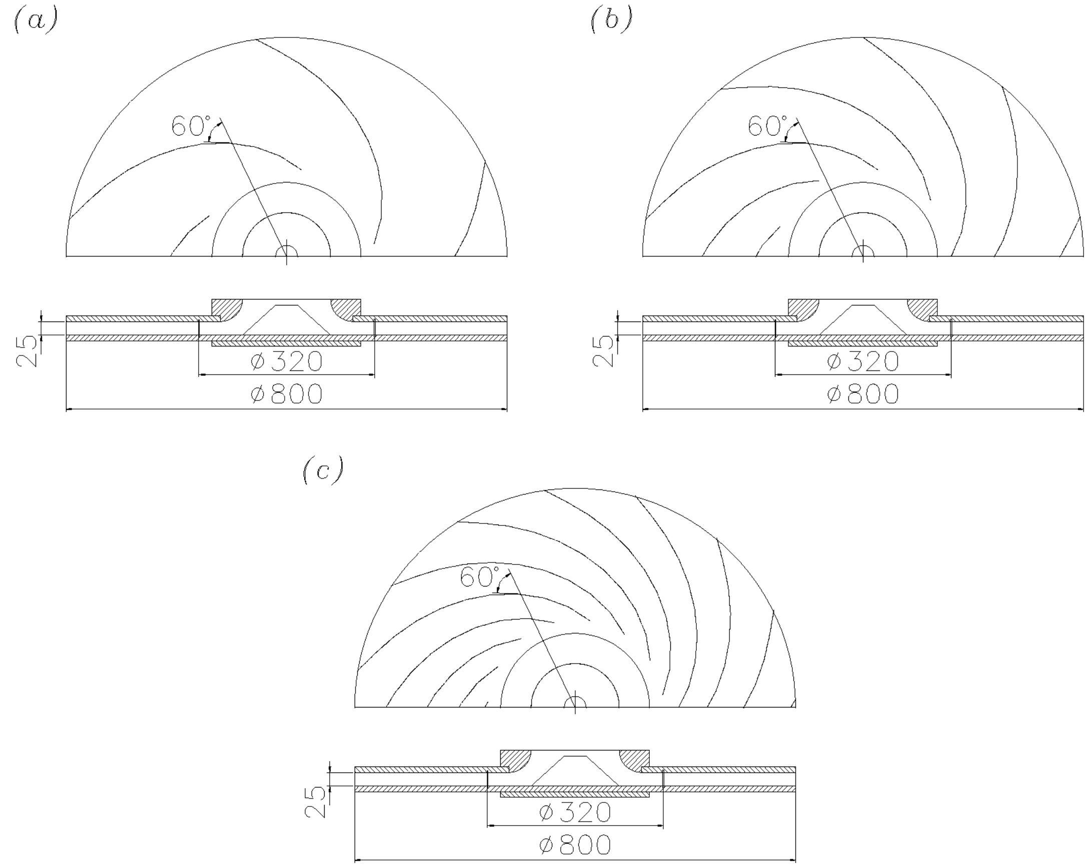

FIGURE 2.3. The test impellers: (*a*) five, (*b*) nine, and (*c*) fifteen blades.

for this particular boundary layer.

2.2 Experimental apparatus and techniques

In this section we will briefly discuss the experimental apparatus and techniques employed. Firstly we will give a description of the test facility, then the laser-Doppler-velocimeter (LDV) system will be discussed, and thirdly the flow visualisation and particle-image-velocimetry (PIV) arrangement will be outlined.

2.2.1 *Test facility*

The experiments were performed in the impeller passage flow apparatus illustrated schematically in figures 2.1 (LDV set-up) and 2.2 (PIV set-up). This open-loop test facility was designed such that throughput and impeller speed could be set independently, which enabled a wide range of operating points.

The test region comprised a transparent perspex test impeller mounted horizontally between two glass windows, on a support that was fixed rigidly on a turntable, which could be driven at any speed from 0 to 100 r.p.m. The volume flow rate through the impeller was controlled by means of a throttling valve in the return duct and could be set from 0 to 20 l/s. The impeller discharged in an oversized vaneless diffuser type of volute (unbounded-impeller performance!), which was equipped with four symmetrically

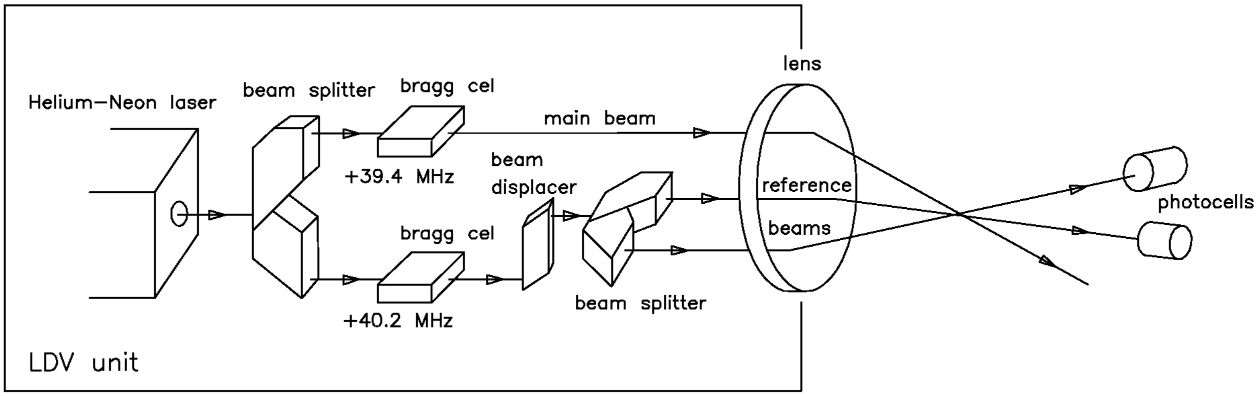

Figure 2.4. Arrangement of the LDV unit and photocells.

arranged outlets. Downstream disturbances were stemmed by a screen with 1.6 % opening, placed around the test impeller at the outer perimeter of the test section. Upstream, in the impeller inlet pipe, a honeycomb type of flow straightener was installed.

A frequency-controlled circulation pump fed the settling tank with demineralised (tap) water from the main tank, such that the test rig operated under overflow conditions; that is, the settling tank was flooded and a small flux of water was bypassed to the main tank. The water volume flow rate (Q_v) through the test region of the rig was measured by a turbine flow meter in the return duct. Both the main tank and the settling tank were open to atmosphere.

In the test rig, we investigated at steady angular speed the blade passage flow of three shrouded 60°, logarithmically-bladed models of low-specific-speed centrifugal pump impellers of simple two-dimensional design. These impellers were equipped with respectively five, nine and fifteen backward-leaning blades (figure 2.3), and they were designed to run at 32 r.p.m. At this angular speed, the Reynolds number based on impeller outlet diameter and tip speed equals 10^{+6}. Furthermore, the specific speed of the test impellers, expressed in terms of the common dimensionless quantity $\Omega_s = \Omega Q_v^{\frac{1}{2}}/(gH)^{\frac{3}{4}}$ (see for instance Dixon 1978), is of the order of 0.3.

2.2.2 *The LDV system*

The system that we used for the laser-Doppler-velocimetry (LDV) flow measurements was a commercial-grade two-component forward-scatter reference-beam arrangement (figure 2.4) with combined counter–tracker signal processor, which was developed by Delft Hydraulics – The Netherlands. Strong points of the arrangement were (*a*) high data density at good signal-to-noise ratio, (*b*) low laser power, and (*c*) simple realisation of two-dimensional measurement system (figure 2.5). The system was operated in its ±1.43 m/s speed range, and functioned as follows:

In the LDV unit (figure 2.4), a 6 mW Helium–Neon laser provided a beam bisected by a beam splitter into a (80 %) high-intensity main beam and a (20 %) low-intensity secondary beam. Two Bragg cells arranged for a frequency shift of 39.4 MHz to the main beam and 40.2 MHz to the secondary beam, thus establishing an actual frequency shift of 0.8 MHz. This pre-shift eliminated directional ambiguity, so that not only the absolute value but also the direction of the velocity components could be measured. A beam displacer corrected the alignment of the secondary beam after the Bragg cell, and a second beam splitter

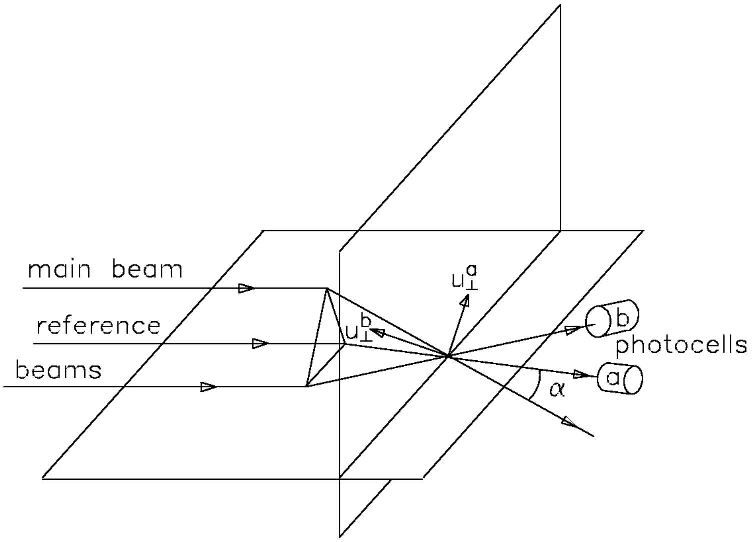

FIGURE 2.5. Principle of the two-dimensional reference beam forward-scatter LDV system.

divided the beam into two identical reference beams. These two reference beams and the main beam were focussed with a 400 mm focal-depth lens, so that they intersected in one point, yielding two ellipsoidal measurement volumes with a (beamwise) length of 6.5 mm each. Two photocells detected the scatter of (natural seed) particles moving through the measurement volumes (figure 2.5), while the detection signals themselves were sent to the processing unit. This signal processing contained two frequency trackers, each of them regulated by a counter; that is, the counters provided the capture range of the trackers and the matching of the signal frequency. This way the small capture range of the frequency trackers was overcome, while a high response rate could still be benefited. The output signal of each tracker was a (DC) voltage level between −10 and 10 V.

In the experimental (LDV) set-up (figure 2.1) the LDV unit was mounted on a traversing apparatus, that was stationed on the turntable and controlled remotely over a slip-ring arrangement. A mirror placed in front of the LDV unit deflected the three laser beams, so that the measurements volumes were positioned in an impeller passage (see also figure 2.6), while a second mirror, attached to the inlet–shroud configuration reflected the (post-measurement) reference beams onto the photocells, which were also mounted on the traversing apparatus. The turntable further held the signal processing unit, of which the output signals were transmitted over the slip-ring arrangement to a remote computer.

With the (co-rotating!) LDV arrangement the radial and circumferential relative (blade passage) fluid velocity could be measured instantly; that is, in each of the two measurement volumes the velocity component $u_\perp$ perpendicular to the bisector of the main beam and the respective reference beam was measured, and from these measurements the radial and circumferential components were computed (by the processing unit). At positions of measurement the two output signals of the processing unit, representing the instantaneous velocity components, were each sampled two thousand times by the remote computer, at a 30 Hz sample frequency, and from the collected samples the ensemble average and variance were computed.

Furthermore, the LDV equipment could also be mounted on the casing of the test section, so that just outside the impeller periphery LDV flow measurements from the fixed frame could be carried out. This way, in fact, the time-averaged impeller discharge-flow velocity could be obtained, and based upon that the actual impeller performance could be

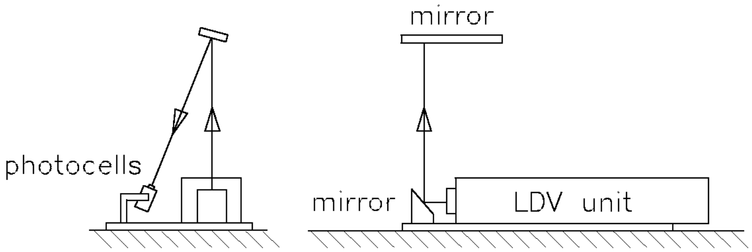

FIGURE 2.6. Arrangement of the LDV system.

computed (§ 2.3.3).

2.2.3 *The PIV system*

To supplement the LDV flow measurements, the experimental facility was modified to the set-up illustrated schematically in figure 2.2, so that visualisation tests by means of stroboscopic imaging of polystyrene tracer particles could be carried out, and, thereupon, video-based (digital) particle-image-velocimetry (PIV) analyses could be performed.

In essence, the technique involved (*i*) seeding the flow with light-scattering particles, (*ii*) visualising an area of the particle-laden flow field by intermittent illumination, (*iii*) recording (multi-exposed) images of the light scattering particles, and (*iv*) processing the particle images in order to obtain the quantitative velocity information desired. Each of these acts affects the outcome of an experiment, and, hence, deserves substantial attention:

(*i*) First of all, it is important that the (seed) particles follow the fluid without significant slip. This implies that the particles should be (almost) neutrally buoyant and as small as possible; that is still being detectable—which largely depends on the intensity of illumination, the scattering power of the particles, the sensitivity of the recording media, and the optics used. For the present work we used polystyrene microspheres of 300 micron with a specific gravity of 1.0 ± 0.02 (water being the carrier fluid). The slip of the particles was estimated by (Adrian 1991)

$$|\Delta u| = \frac{\rho_p}{\rho}\frac{d_p^2}{36\nu}|\dot{u}| \tag{2.1}$$

in which – with subscript p denoting particle properties – ρ is density and ν is kinematic viscosity of the carrier fluid, d is diameter and Δu and $\dot{u}$ are slip velocity and acceleration. This way the slip was found to be less than 2.5 % (based on $|\dot{u}| \approx u^2/r$ and taking into account that u and r are of the order of 1 m/s and 0.1 m respectively). Although this slip is quite substantial in magnitude, it is acceptable for the visualisation of the impeller passage flow.

Additionally, also the density of seeding is of importance: On the one hand, a high density is desired in order to improve the valid data yield (see Westerweel 1994), while on the other hand seeding should be kept low, so that sufficient optical transparency of the fluid remains and fluid↔particle↔particle coupling is avoided. The latter, i.e. the fluid dynamical influence of the seed particles, may be judged by the particle fraction

$$x_p = \rho_s/\rho_p \tag{2.2}$$

in which ρ_s is the density of seeding (i.e. the mass of particles per unit volume of working fluid). This particle fraction, in fact, yields the volume of particles per unit volume of

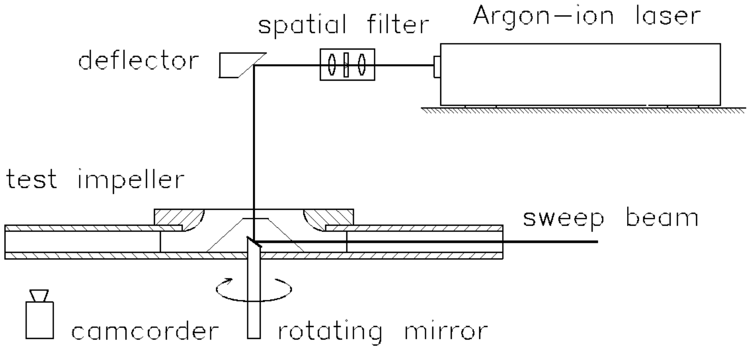

Figure 2.7. Sweep-beam optical arrangement. A beam from a continuous wave laser is deflected onto a rotating single-facet inclined mirror so that the plane of observation is scanned periodically.

working fluid. According to Elghobashi (1994) fluid↔particle↔particle coupling takes places at $x_p \geq 10^{-3}$. For the current study the (density of) seeding was taken such that – in conjunction with the way of illumination – the count of image pairs within an interrogation cell numbered the guide-line value of 15 (see Adrian 1991). This resulted in a particle fraction of the order of 10^{-4}, i.e. a dilute suspension (see also Elghobashi 1994), yielding a number density of the order of 10 particles per ml.

(*ii*) In order to illuminate the particle-laden flow field a sweep-beam (scanning) technique was employed (figure 2.7). The beam of a 3.5 W (output power) continuous wavelength Argon-ion laser was directed onto an inclined single-facet rapidly rotating mirror, which reflected the beam so that in the fluid the plane of observation was scanned periodically; the frequency of illumination being this way equal to the angular speed of the rotating mirror. The scanning frequency of the sweep beam was adjusted remotely, over the slip-ring arrangement, by means of voltage control of the mirror drive. The plane of observation could be set from hub to shroud by vertical adjustment of the rotating mirror; all visualisations, however, were done at blade passage midheight. A spatial filter was used to give the laser beam a diameter of 2 mm in the plane of observation. Furthermore, an air-filled optical tube was installed in the inlet pipe to get a short optical path through the water, so that the high energy of the laser beam was retained.

(*iii*) Because of the flexibility of videographic recording, a domestic (interlaced) Sony CCD-TR8E video camcorder with a spatial resolution of 470,000 pixels was used to record the images. The camcorder was mounted on the turntable – thus co-rotating with the impeller – and its video signal was wiretapped over the slip-ring arrangement so that (the recording of) the blade passage flows could be observed on a remote display. The video images of the flow patterns were stored on standard 8 mm video tape, while recording itself was controlled remotely by infra-red light.

(*iv*) At the (PIV) processing stage, a video-taped frame was first digitised into an eight-bit 640×480 pixel array, and then processed by image analysis software (so-called PIVware, developed at Delft University of Technology—The Netherlands) which we ran on a HP9000/700-series workstation. The PIVware computed the (most probable) map of displacement vectors, which were thereupon multiplied by the scanning frequency of the sweep beam and the length-per-pixel factor in order to get the velocity information. The length-per-pixel factor, linking bitmap and real-scene dimensions, was computed directly from the digitised frame. Furthermore, statistical tests, implemented in the PIVware, were employed to detect and subsequently delete invalid vectors (see also Westerweel 1994).

Deleted vectors were not replaced by interpolated vectors since, mathematically speaking, we have cuts in each image (namely the blades) and, hence, discontinuities in the fluid velocity; a straight-forward interpolation algorithm would have generated false vectors. (Mathematical details of the – digital – technique can be found in Westerweel 1993.)

The scanning-beam technique (compared to conventional pulsed laser sheet illumination using a cylindrical lens) is highly efficient and extremely profitable because of the high energy density of illumination. It enables imaging of small particles with limited scatter efficiency, which might remain undetected if the beam is expanded into a light sheet. A minor imperfection of the sweep-beam technique is that there will be a (small) systematic error in the computed velocity if no correction is made to account for the fact that not all particles are illuminated at the same instant. Yet, when the sweep velocity (v_s) is high compared to the velocity (v) in the experimental system, the correction required will be negligible. (For the experiments performed was $v/v_s < 10^{-2}$, and, hence, a correction was omitted.) Furthermore, one should be aware of the image-blurring drift of the particles as a result of the fact that illumination takes place over a certain period of time. This drift simply equals the particle velocity multiplied by the exposure time. The exposure time being for a scanning-beam arrangement approximately equal to the beam diameter (D) divided by the sweep velocity, taking into account that the particle diameter is much smaller than the beam diameter, and that the sweep velocity is much higher than the particle velocity. This way we computed for the present work that the drift was less than 4 micron ($v_s > 600$ m/s, $D = 2$ mm, $v = O(1$ m/s$)$). This distance represents only a fraction of a pixel in a digitised image, and is negligible by comparison with the maximum displacement (being $O(1$ mm$)$).

2.3 Results

In this section we will discuss the passage-flow real fluid behaviour, based upon the experimental data obtained. The discussion given will emphasize, in particular, the potential-flow character (of the core-flow region) of the blade passage flow.

Our plan of discussion is first to discuss the particle-image observations, as well as the outcome of the digital analysis. Then, we will present the LDV flow measurements of the blade passage flows, and compare them with the corresponding potential-flow calculations. Next, the (actual) impeller performance (obtained from the fixed-frame LDV flow measurements of the impeller discharge flow) will be discussed. Lastly, we will focus our attention on (the calculation of) the viscous boundary layer on the blade suction side, and demonstrate that the common thin-shear-layer approximation leads to satisfactory results.

N.B. As yet, the attention has been principally confined to the blade suction side because the LDV flow measurements particularly showed that there was no significant boundary-layer (displacement) thickness on the blade pressure side. Moreover, exploratory calculations performed in the way outlined below (§ 2.3.4) have indicated that a direct-hierarchy approach to compute the boundary layer on the blade pressure side does not hold. (The boundary layer, in particular the portion near the leading edge, was computed at values far beyond reality.) A possible way (that has not been explored here) to compute this particular boundary layer correctly, might be the multistructured triple-deck approach (strong interaction, no hierarchy), see for instance Stewartson (1974).

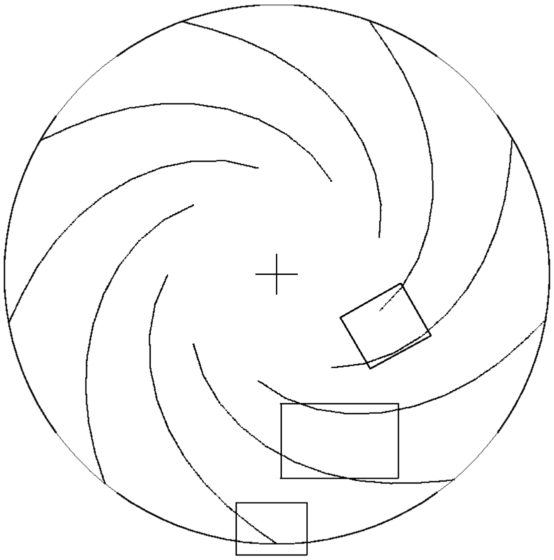

FIGURE 2.8. Location of the images.

2.3.1 *Particle-image exploration of blade passage flows*

During the visualisation tests that were carried out, the observation of the particle-image streaklines brought out clearly that the flow inside the blade passages (of the set-up) was steady with time and unidirectional, except at low off-design volume flow rates, that is at throughput well below the value corresponding to shockless entry. There we clearly observed the cyclic motion that is generally addressed as rotating stall (see also Fisher & Thoma 1932, and Lennemann & Howard 1970). This flow phenomenon was encountered (and video-taped) in all three test impellers at volume flow rates below $-\Phi \approx 0.05^{\dagger}$, at which the cycle frequency appeared to be equal to 15–20% of the rotational speed. Furthermore, near design discharge flow ($\Phi \approx -0.1$) the particle images showed a normal impeller passage flow with minor entrance shock, whereas well above design discharge flow a leading-edge streamline discontinuity and a modest pressure-side leading-edge separation bubble were observed.

Particularly, it became evident from the preliminary (visual) tests at near-design discharge that a predominant potential-flow type of fluid behaviour was actually present inside the blade passages, in that we observed higher values of the passage velocity at the blade suction side and near stagnation flow at the blade pressure side. A typical example of such a flow that we encountered near design discharge is shown is figure 2.9 (the location of the image is shown in figure 2.8). It displays the particle image and the PIV measurement result of the blade passage flow in the nine-bladed test impeller at $\Phi = -0.09$ ($Q_v = 7.8$ l/s; $\Omega = -32$ r.p.m.). The PIV measurement result originally contained approximately 15 % spurious vectors, which have been removed from the final result presented. The plot clearly exposes that between the blades there are low fluid velocities along the blade pressure side (PS/convex surface) and high fluid velocities along the blade suction side (SS/concave surface), which confirms the presence of the relative eddy. This presence is even better reflected in figure 2.10, which displays the outcome after subtracting the mean throughput velocity: $(v_r, v_\phi) = \frac{Q}{2\pi r}(1, \tan(\beta))$. This mean-throughput-subtracted result clearly

---

[†] By the convention of chapter 1, pump impellers with backward-leaning blades have a negative Φ!

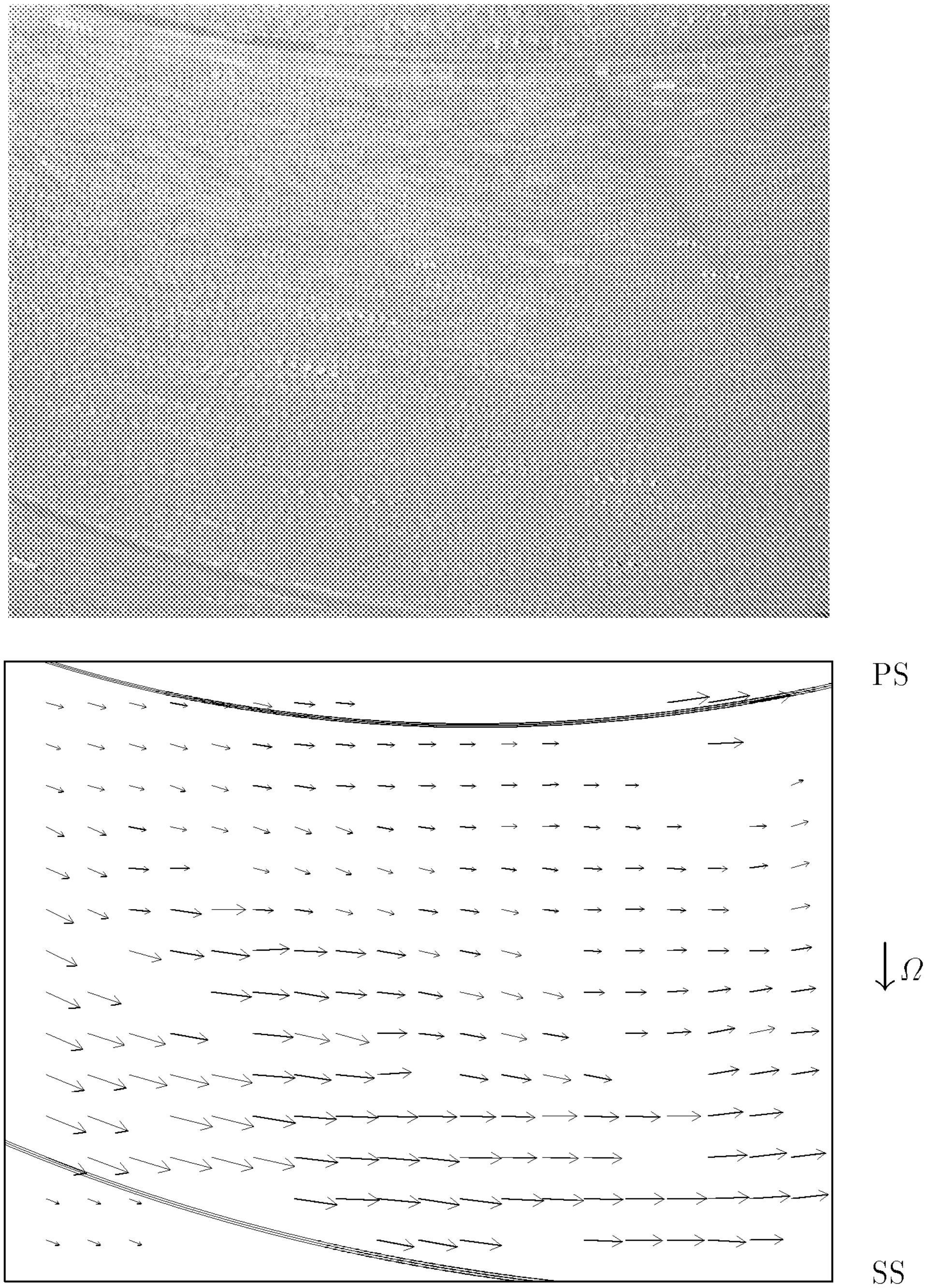

FIGURE 2.9. Image and PIV measurement result of the passage flow in the nine-bladed test impeller at $\Phi = -0.09$; the solid lines represent the blades.

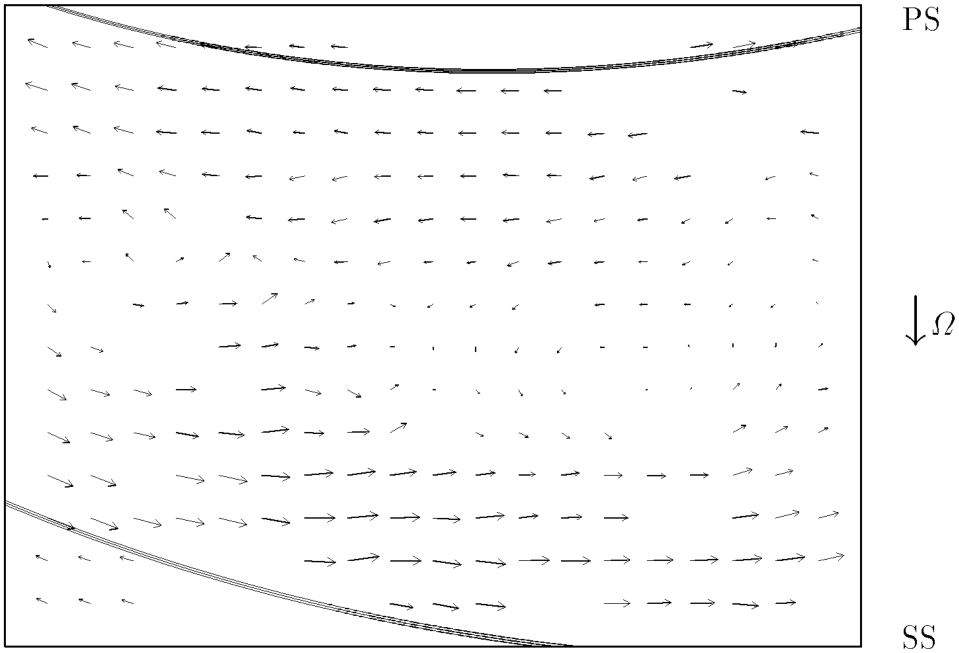

FIGURE 2.10. Flow pattern in the nine-bladed test impeller as obtained from figure 2.9 after subtracting the mean throughput velocity; the solid lines represent the blades.

shows the positive contribution to the fluid velocity along the suction side and the negative (i.e. reverse-flow) contribution along the pressure side, due to the rotation of the impeller (termed displacement flow as discussed in chapter 1).

Above-described (potential-flow) passage flow pattern was encountered over a relatively wide range of operation, both below and above design discharge, for regions reasonably well inside the blade passages. Differences in flow behaviour for the various operating points were concentrated near the entrance region, showing images like the ones presented in figure 2.11. This figure shows the flow near the leading edge of the nine-bladed impeller at low ($\Phi = -0.06$), medium ($\Phi = -0.09$), and high ($\Phi = -0.12$) volume flow rate. The high volume flow rate (figure 2.11*c*), as mentioned already above, resulted in the formation of a pressure-side leading-edge separation bubble, whereas the low volume flow rate (figure 2.11*a*) yielded separation of the flow on the suction side (i.e. stall). At medium volume flow rate (figure 2.11*b*), shockless entry was clearly observed.

Having discussed the flow field images that were obtained well inside the blade passages and at the entrance region, we lastly turn to the impeller discharge area or trailing edge region. Like the flow well inside the passages, the flow at this region looks quite the same over a relatively wide range of operation. As a characteristic example, figure 2.12 shows the flow near the trailing edge at $\Phi = -0.09$. The PIV measurement result demonstrates that the fluid runs off the trailing edge smoothly, exemplifying Zhukovski's hypothesis.

The preceding discussion briefly reviews the huge amount of visual data that was collected during the particle-image exploration of the flow in the test impellers. For the remainder, we shall refrain from further considering these supplementary (!) PIV measurement results since the LDV flow measurements, that are to be discussed below, provided superior data with regard to the validation of the potential-flow calculations and the further study of blade passage flows.

Finally, we remark that the images presented, particularly depict the flow field in the nine-bladed test impeller. Results obtained for the five-bladed test impeller and the fifteen-

(*a*)

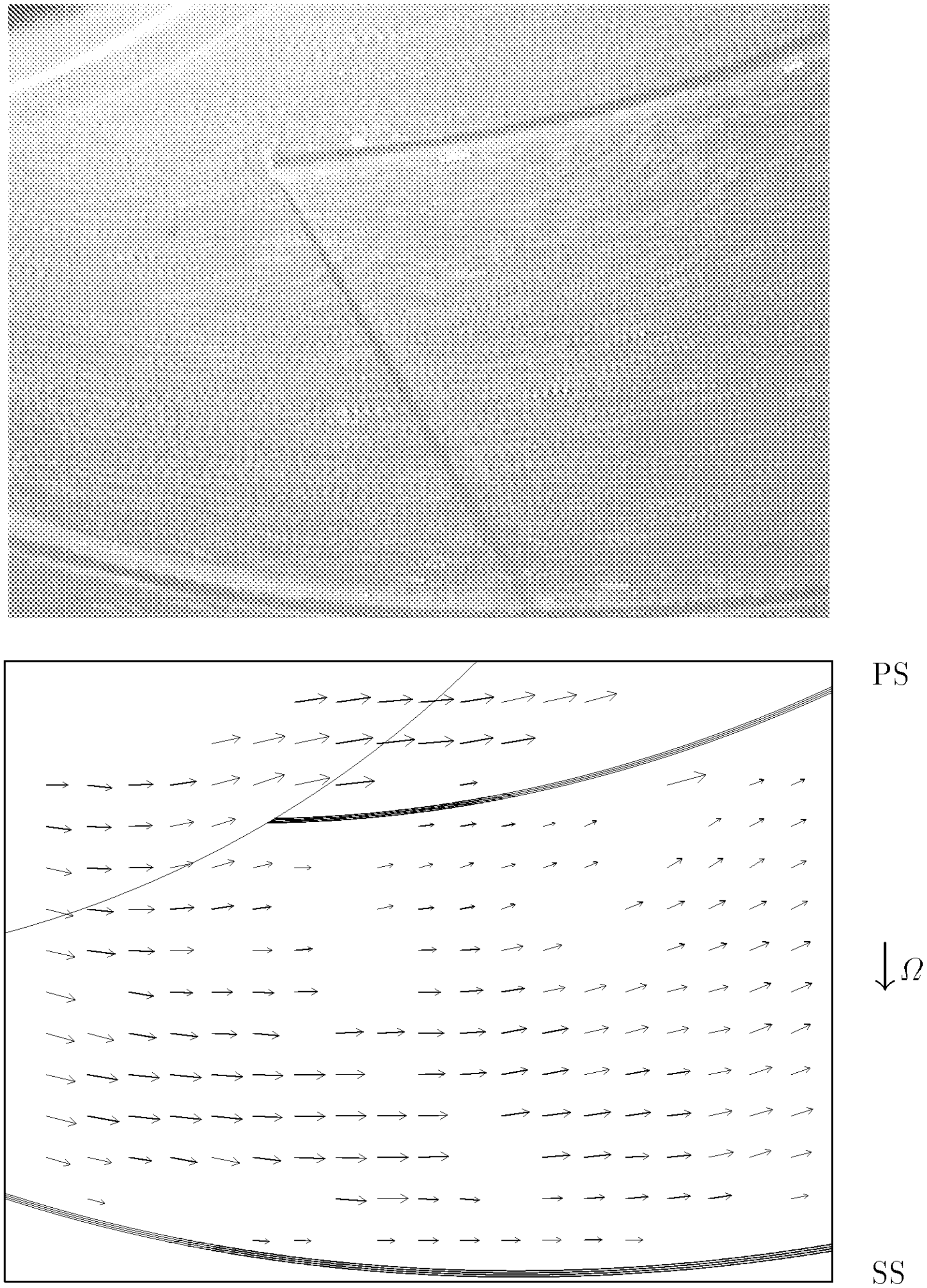

(*b*)

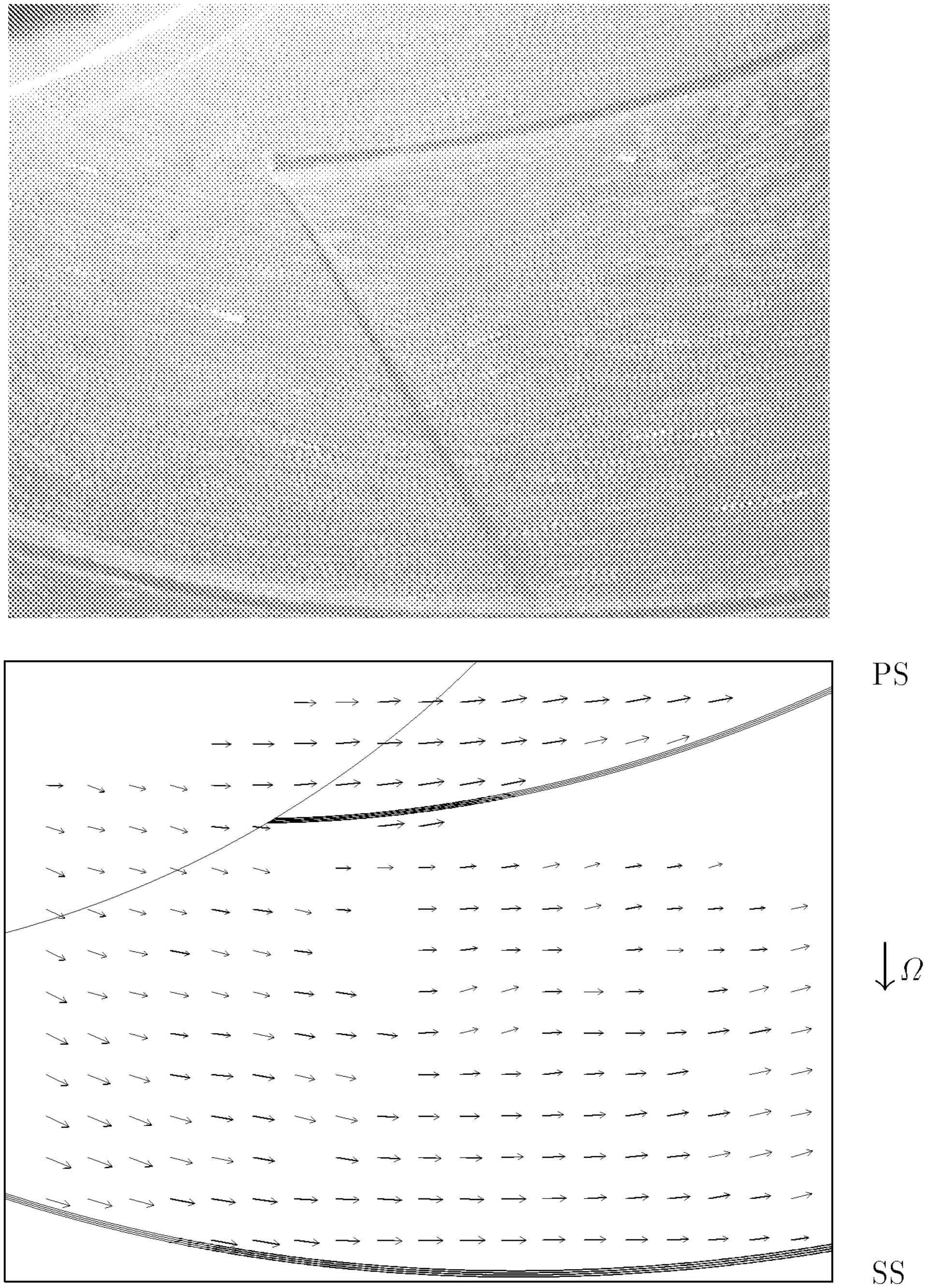

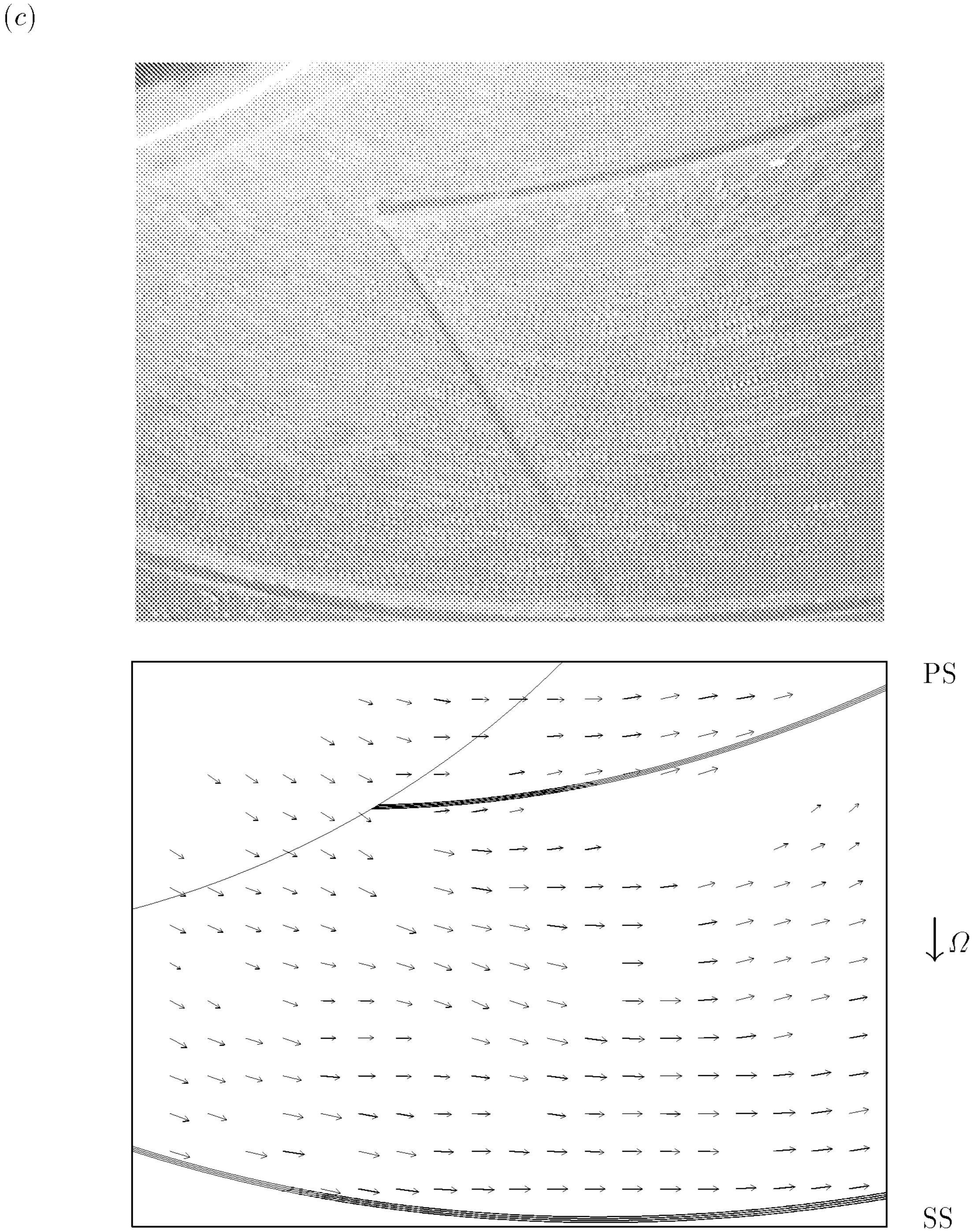

FIGURE 2.11. Image and PIV measurement result of the flow near the leading edge of the nine-bladed test impeller at (*a*) $\varPhi = -0.06$, (*b*) $\varPhi = -0.09$, and (*c*) $\varPhi = -0.12$; the solid lines represent the blades.

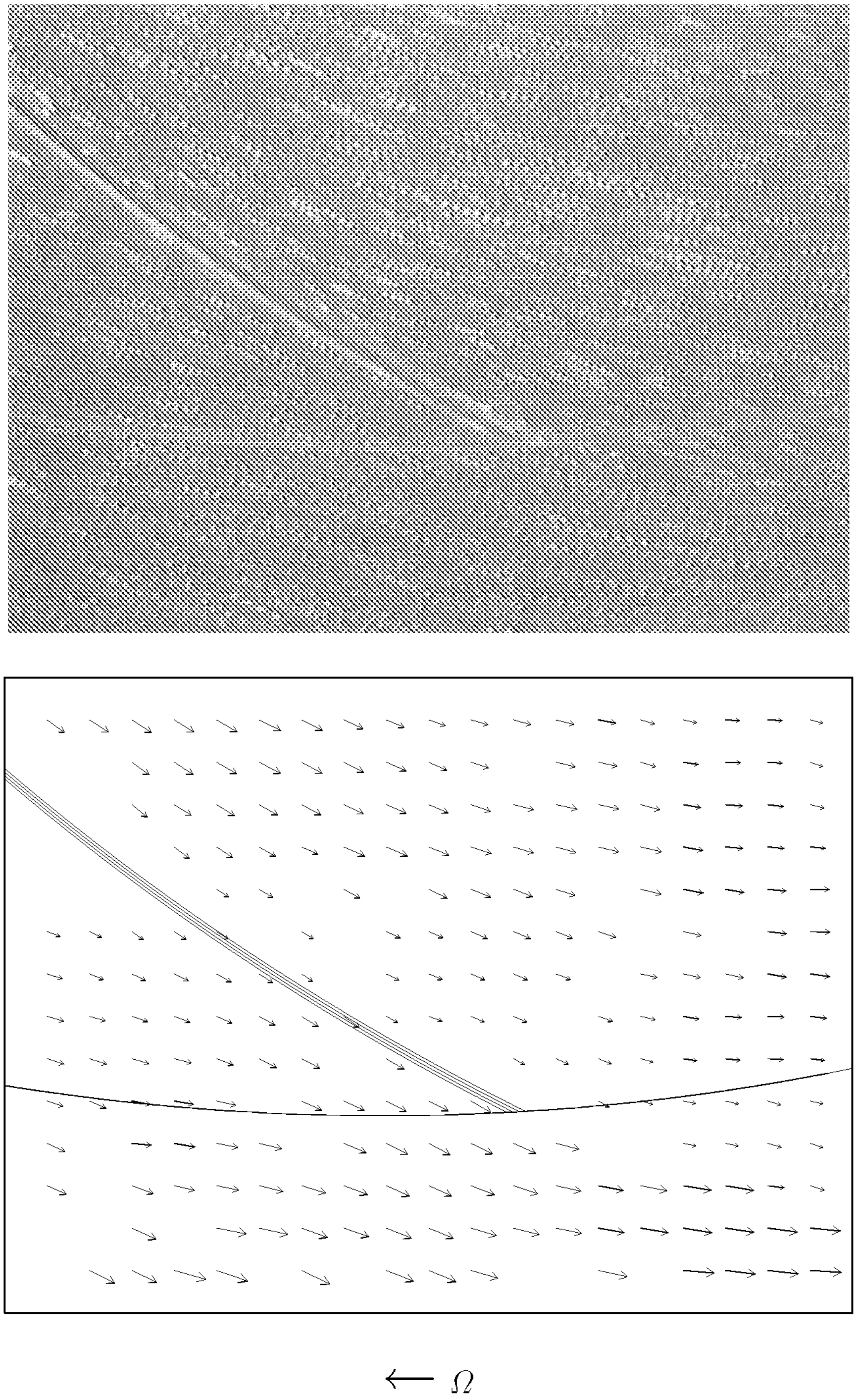

FIGURE 2.12. Image and PIV measurement result of the flow near the trailing edge of the nine-bladed test impeller at $\Phi = -0.09$; the solid lines represent the blade.

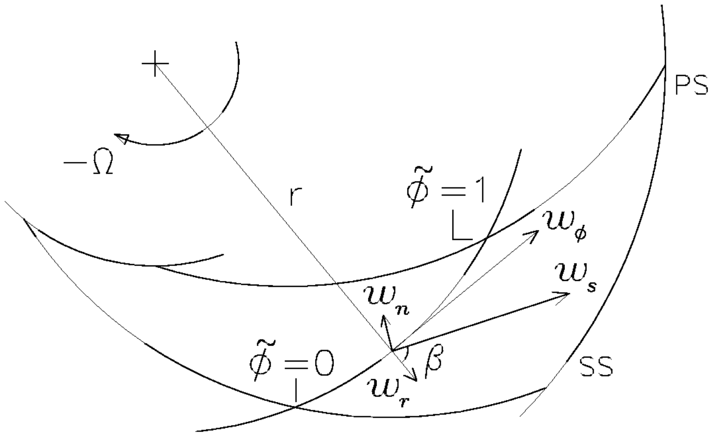

FIGURE 2.13. System of blade-passage coordinates.

bladed test impeller are however quite similar, that is they expose identical flow patterns, and, hence, discussion of these results has been omitted.

2.3.2 *Blade-to-blade LDV flow measurements*

The LDV flow measurements in the rotor frame of reference were the principal output of our experiments, and the prime results of it will be outlined here. Principally, we will discuss the blade-to-blade measurements that were made along radial cross-passage trajectories at passage midheight, inside all three test impellers, at steady revolutionary speed and design discharge flow. In addition, for the nine-bladed test impeller we will also present measurements along circumferential cross-passage trajectories at passage midheight, as well as two sets of hub-to-shroud cross-sectional measurements.

Measured were the radial and circumferential (relative) velocity components (w_r and w_ϕ), from which both the streamwise and (normal) cross-passage component w_s and w_n were obtained. The discussion, however, will be confined chiefly to the streamwise passage velocity since only this velocity component is of (actual) importance. The component normal to the streamwise velocity will just be discussed in passing.

The presentation of the respective results will be done in a dimensionless form and will include both the measurement data and the corresponding calculated potential-flow results. To this end the velocities have been scaled by the impeller tip speed (Ωr_2), and has the position along the respective trajectories been non-dimensionalised by blade-fitted coordinates $(\tilde{r}, \tilde{\phi}) \in [0, 1]$, defined as

$$\tilde{r} = \frac{r - r_{ps}}{r_{ss} - r_{ps}} \tag{2.3}$$

$$\tilde{\phi} = \frac{\phi - \phi_{ss}}{\phi_{ps} - \phi_{ss}} \tag{2.4}$$

where the respective subscripts denote suction side (ss) and pressure side (ps); see also figure 2.13.

Furthermore, the theoretical (potential-flow) results that will be presented, have been computed principally from the solution that holds asymptotically in a region well away from the blade tips, i.e. expansion (1.165), except for those regions were the expansion does not hold—there the theoretical results were obtained from additional finite-element

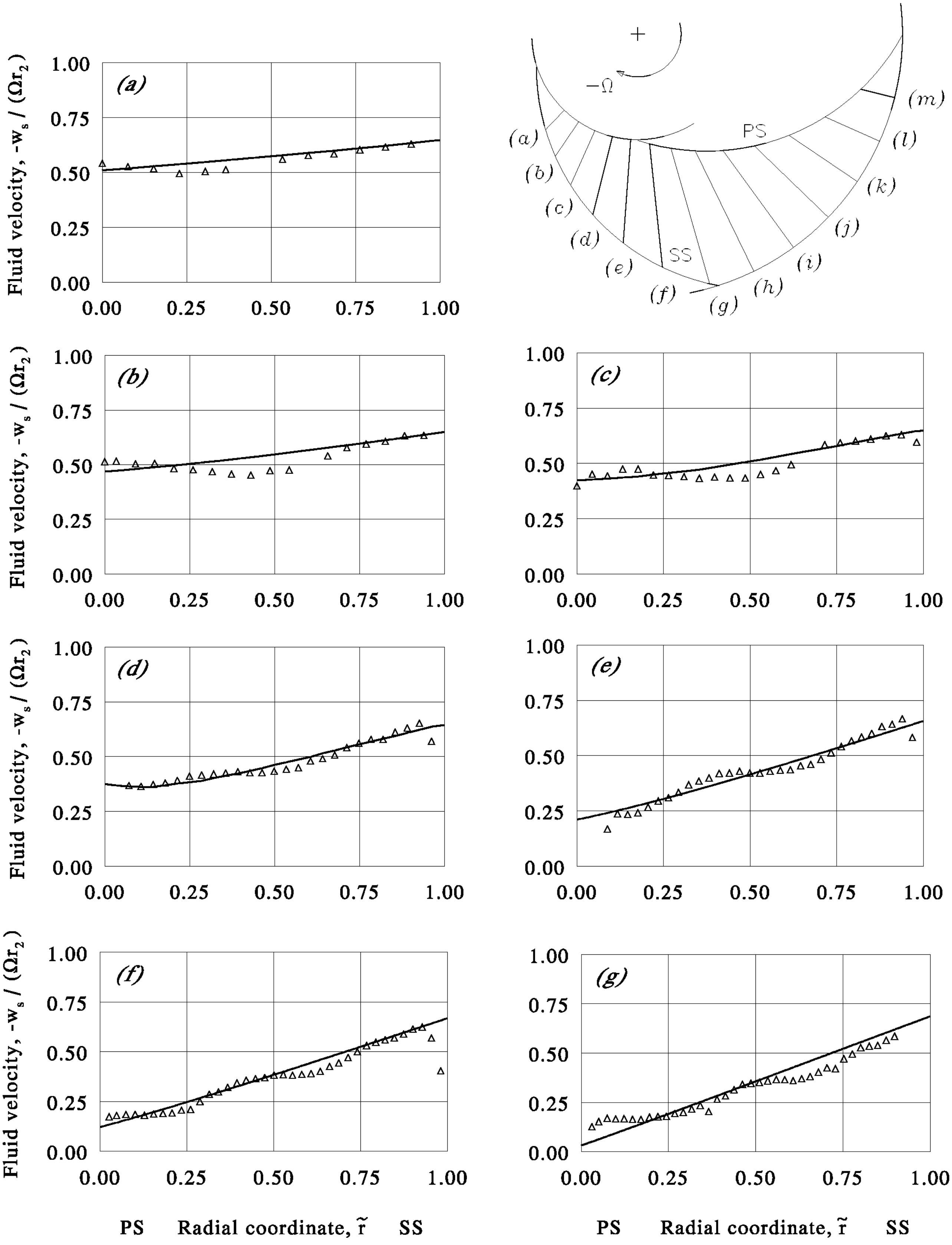
+
−Ω
PS
SS
(a)
(b)
(c)
(d)
(e)
(f)
(g)
(h)
(i)
(j)
(k)
(l)
(m)
Fluid velocity, -w_s / (Ωr_2)
1.00
0.75
0.50
0.25
0.00
0.00
0.25
0.50
0.75
1.00
PS Radial coordinate, r̃ SS

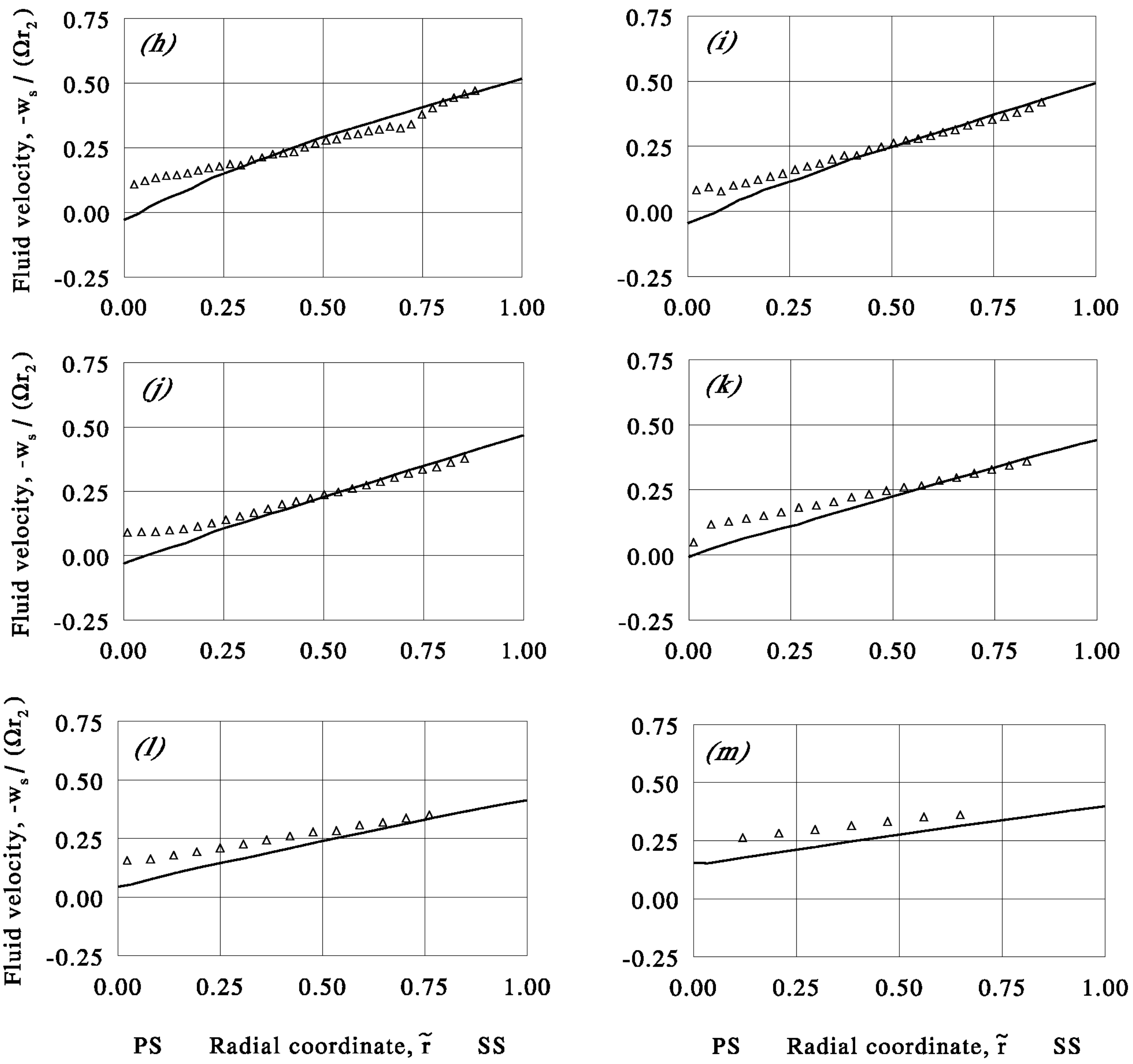

FIGURE 2.14. Measured and computed mid-height streamwise passage velocities at $\Phi = -0.11$ for the five-bladed test impeller; (*a*) $R_{ss} = 0.564$, (*b*) $R_{ss} = 0.621$, (*c*) $R_{ss} = 0.683$, (*d*) $R_{ss} = 0.751$, (*e*) $R_{ps} = 0.400$, (*f*) $R_{ps} = 0.440$, (*g*) $R_{ps} = 0.484$, (*h*) $R_{ps} = 0.533$, (*i*) $R_{ps} = 0.586$, (*j*) $R_{ps} = 0.664$, (*k*) $R_{ps} = 0.709$, (*l*) $R_{ps} = 0.780$, (*m*) $R_{ps} = 0.858$. Experimental data indicated by symbols; solid lines indicate computed results: (*a*)–(*d*) and (*h*)–(*m*), finite element method; (*e*)–(*g*), asymptotic expansion (1.165).

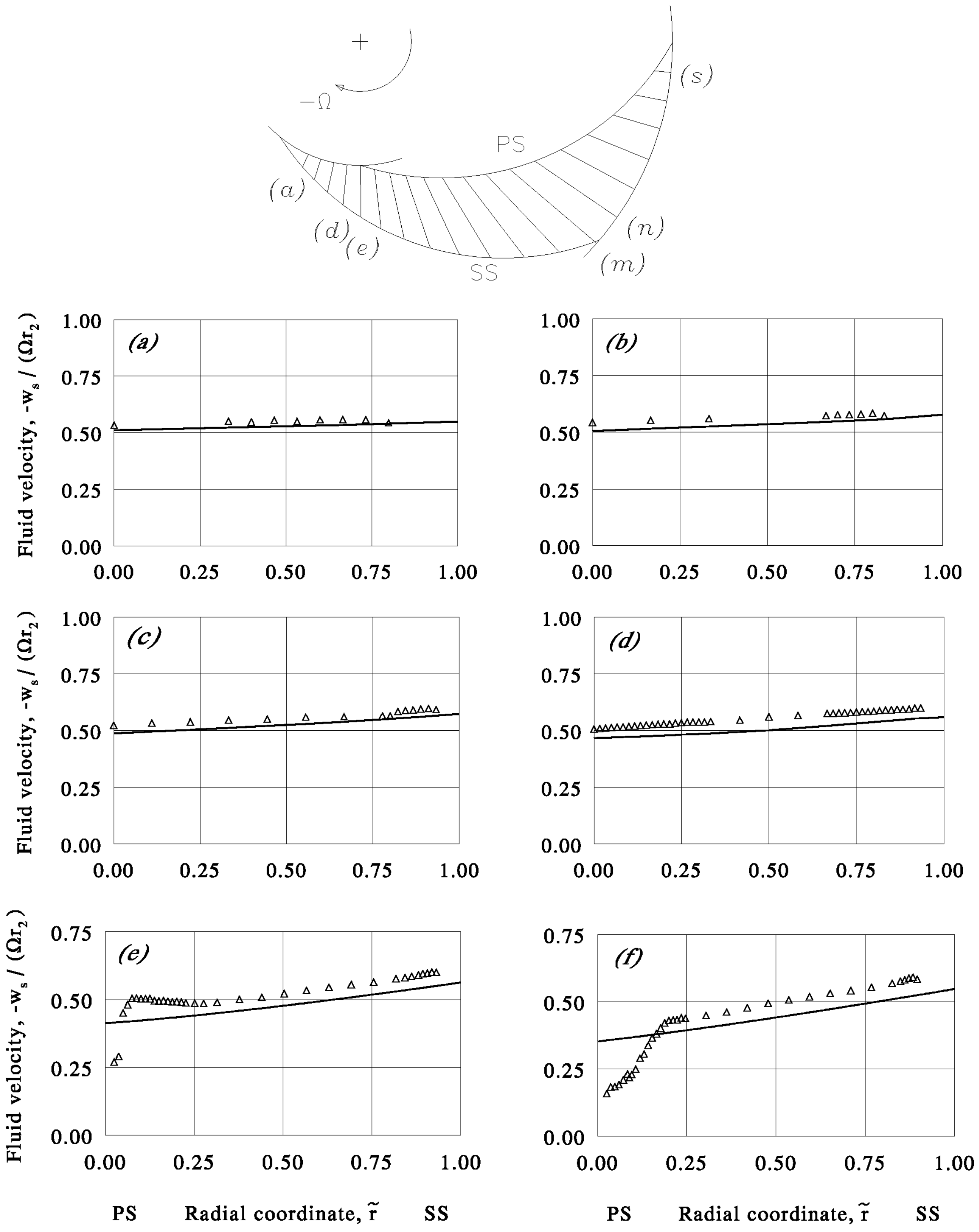
+
−Ω
PS
SS
(s)
(a)
(d)
(e)
(n)
(m)
(a)
(b)
(c)
(d)
(e)
(f)
Fluid velocity, $-w_s / (\Omega r_2)$
1.00
0.75
0.50
0.25
0.00
0.00
0.25
0.50
0.75
1.00
PS
Radial coordinate, $\tilde{r}$
SS

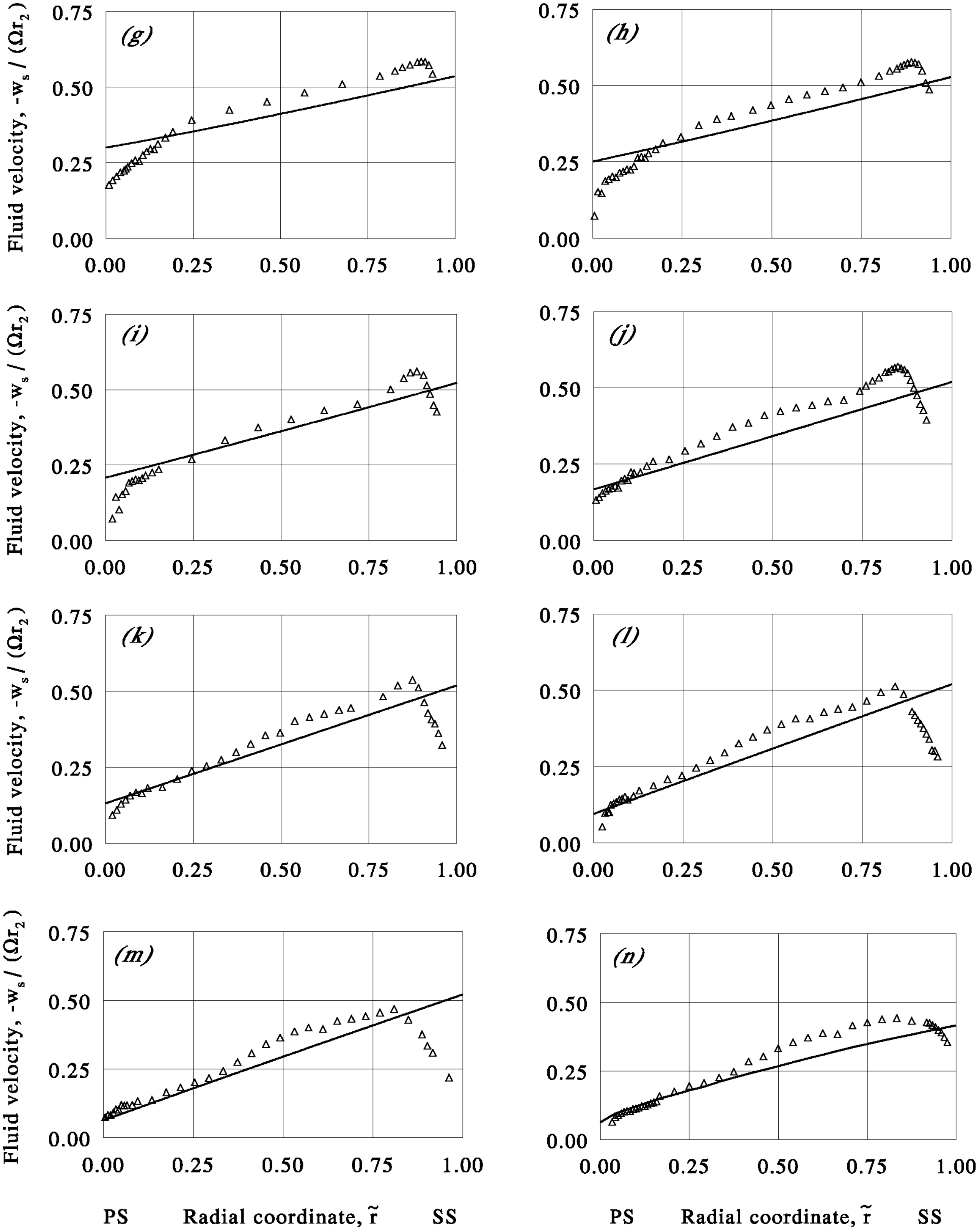
(g)
(h)
(i)
(j)
(k)
(l)
(m)
(n)
Fluid velocity, $-w_s / (\Omega r_2)$
0.00
0.25
0.50
0.75
1.00
PS
Radial coordinate, $\tilde{r}$
SS

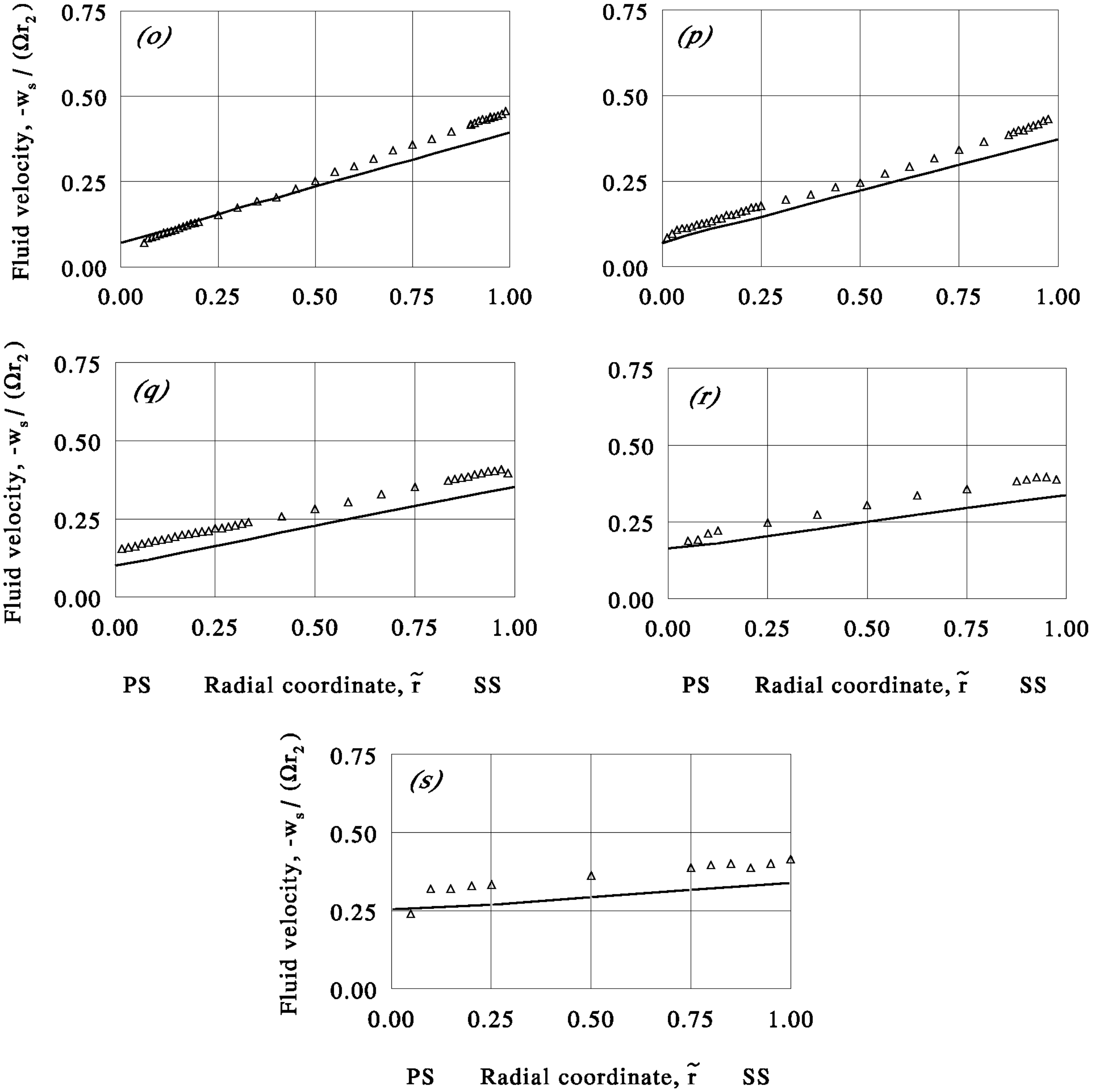

FIGURE 2.15. Measured and computed mid-height streamwise passage velocities at $\Phi = -0.11$ for the nine-bladed test impeller; (a) $R_{ss} = 0.438$, (b) $R_{ss} = 0.475$, (c) $R_{ss} = 0.513$, (d) $R_{ss} = 0.550$, (e) $R_{ps} = 0.400$, (f) $R_{ps} = 0.434$, (g) $R_{ps} = 0.467$, (h) $R_{ps} = 0.501$, (i) $R_{ps} = 0.534$, (j) $R_{ps} = 0.568$, (k) $R_{ps} = 0.601$, (l) $R_{ps} = 0.635$, (m) $R_{ps} = 0.668$, (n) $R_{ps} = 0.700$, (o) $R_{ps} = 0.750$, (p) $R_{ps} = 0.800$, (q) $R_{ps} = 0.850$, (r) $R_{ps} = 0.900$, (s) $R_{ps} = 0.950$. Experimental data indicated by symbols; solid lines indicate computed results: (a)–(d) and (n)–(s), finite element method; (e)–(m), asymptotic expansion (1.165).

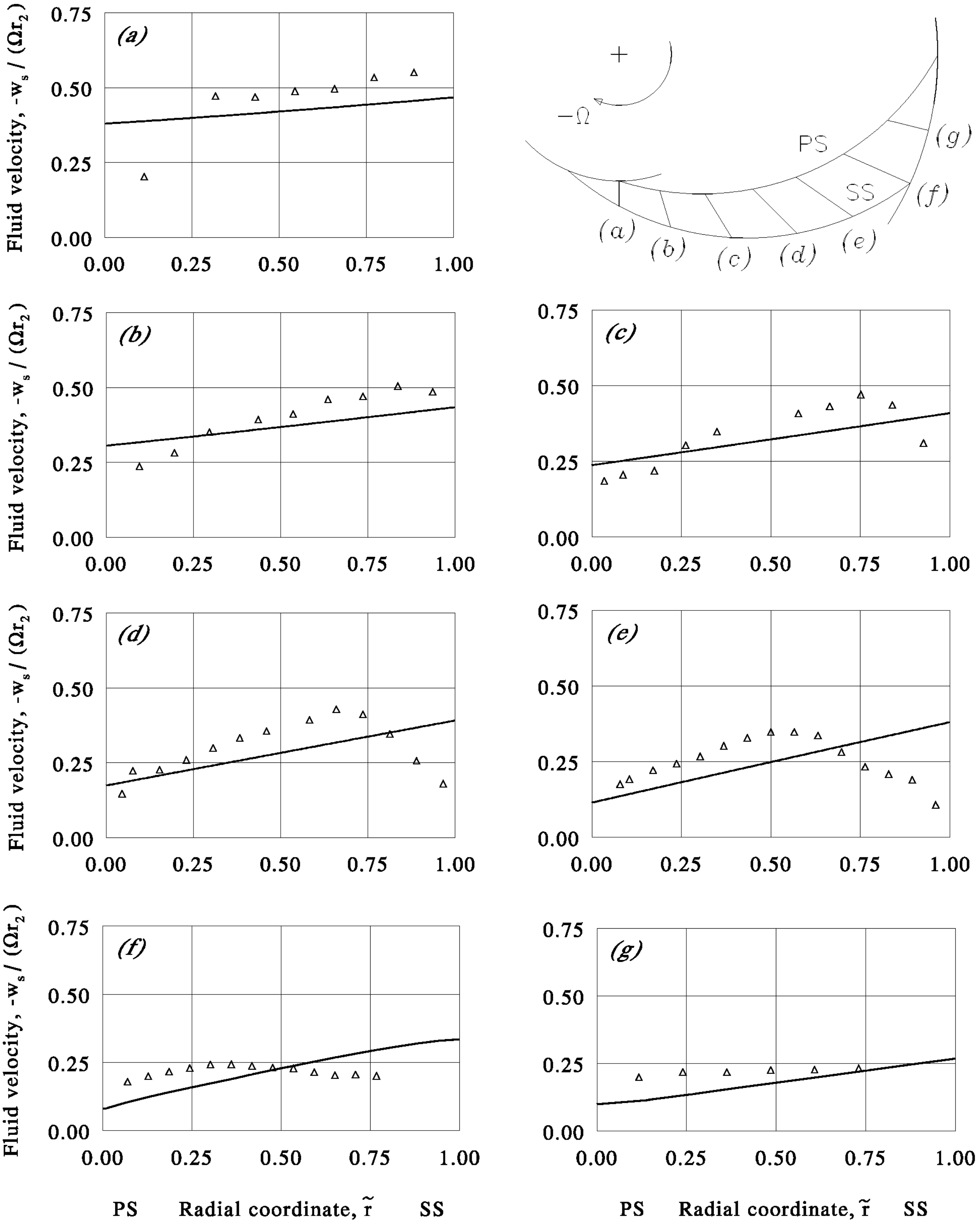

FIGURE 2.16. Measured and computed mid-height streamwise passage velocities at $\Phi = -0.09$ for the fifteen-bladed test impeller; (*a*) $R_{ps} = 0.400$, (*b*) $R_{ps} = 0.458$, (*c*) $R_{ps} = 0.525$, (*d*) $R_{ps} = 0.600$, (*e*) $R_{ps} = 0.685$, (*f*) $R_{ps} = 0.785$, (*g*) $R_{ps} = 0.898$. Experimental data indicated by symbols; solid lines indicate computed results: (*a*)–(*e*), asymptotic expansion (1.165); (*f*) and (*g*), finite element method.

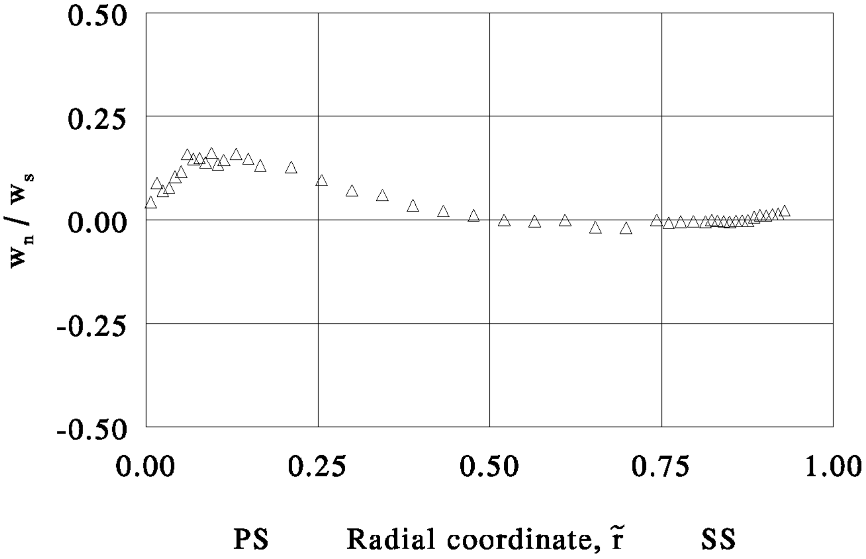

FIGURE 2.17. Relative magnitude of the (normal) cross-passage velocity along the $R_{ps} = 0.568$ traverse of the nine-bladed test impeller (trajectory j in figure 2.15).

calculations (van Esch 1995). Further, the asymptotic values along radial cross-passage trajectories were computed from (1.165) by using the relationship

$$\tilde{\phi} = 1 - \frac{n\tan(\beta)}{2\pi}\ln\left(\frac{r}{r_{ps}}\right) \tag{2.5}$$

which describes a radial traverse ($r_{ps} \le r \le r_{ss}$) in blade-fitted coordinates. The respective theoretical results are, in the figures concerned, reflected by solid lines.

The first result presented, concerns the radial-traverse measurements, which are given in figures 2.14–2.16 for, successively, the five-, nine-, and fifteen-bladed test impeller. These figures show the (scaled) values of the streamwise velocity (w_s) along radial traverses that are characterised by their interception with the blade pressure side, i.e. $R_{ps} = r_{ps}/r_2$, or the blade suction side, i.e. $R_{ss} = r_{ss}/r_2$.

Furthermore, to illustrate the low relative magnitude of the (normal) cross-passage velocity, we have plotted the w_n to w_s ratio for the $R_{ps} = 0.568$ traverse inside the passage of the nine-bladed impeller (figure 2.17). This figure clearly shows that in the core-flow region a next-to-zero cross-passage velocity prevails. Only near the pressure side we notice a comparatively high cross-passage velocity. Nonetheless, the absolute contribution of this velocity component to the passage velocity still being negligible.

The last plots presented here, i.e. figures 2.18 and 2.19, show the additional measurements for the nine-bladed test impeller. Figure 2.18 shows the values of the blade-to-blade streamwise passage velocity at midheight along the circumferential cross-passage trajectories, while figure 2.19 displays the cross-sectional hub-to-shroud measurements.

With reference to the respective plots we see that the measurement data compare extraordinarily well with the respective theoretical potential-flow predictions (for the core-flow region) all along the passage. So, the potential-flow character is distinctly present! Near the blade surfaces we further notice a departure from the potential-flow behaviour due to the effect of viscosity. In particular, we experience substantial development of (non-separated) viscous boundary layers along the suction side of the blades, whereas the boundary layer growth along the blade pressure side is seen to be next to zero. The latter

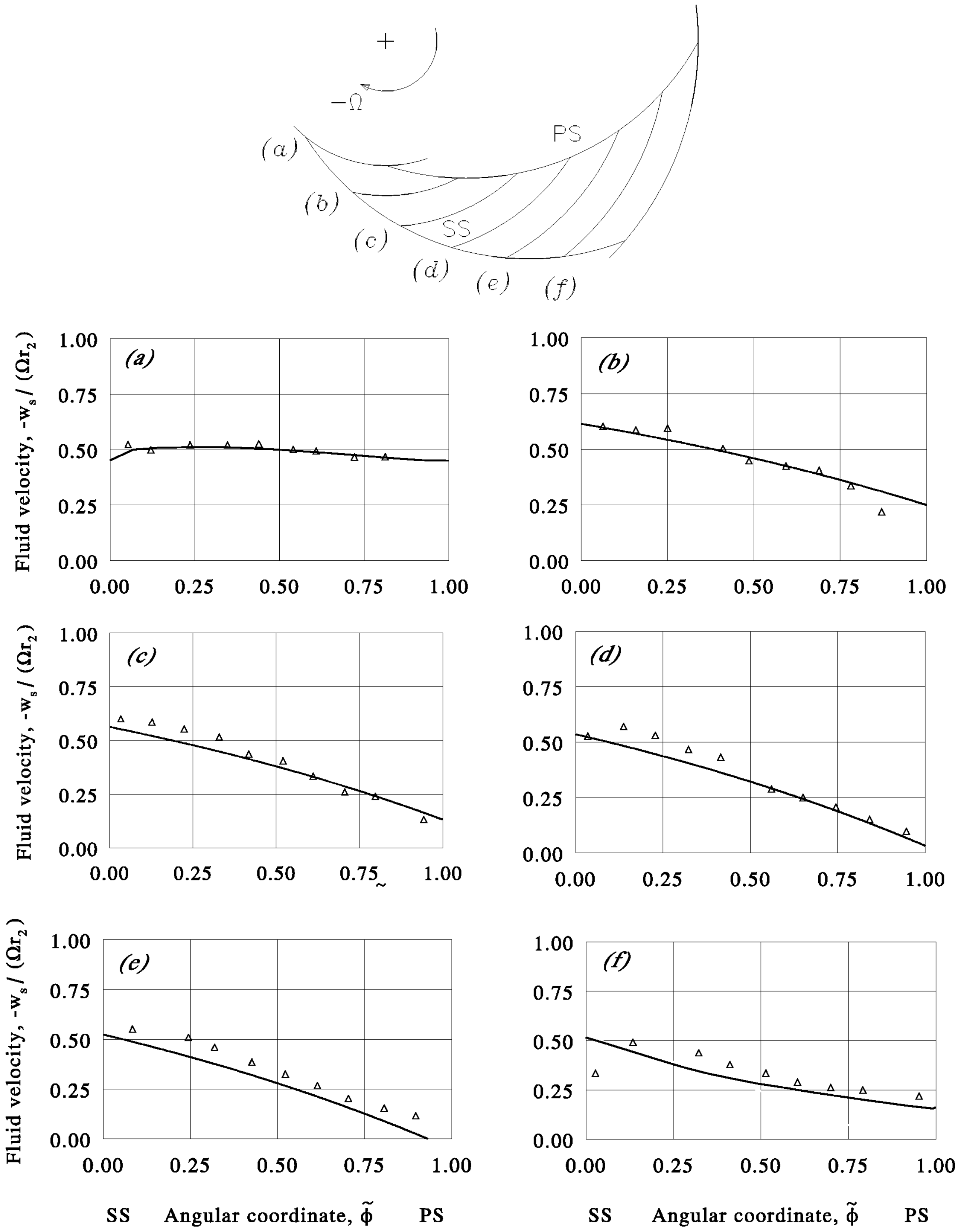

FIGURE 2.18. Measured and computed mid-height streamwise passage velocities at $\Phi = -0.11$ for the nine-bladed test impeller at radial distances $(r - r_1)/(r_2 - r_1)$ of (*a*) 1/6, (*b*) 2/6, (*c*) 3/6, (*d*) 4/6, and (*e*) 5/6. Experimental data indicated by symbols; solid lines indicate computed results: (*a*) and (*f*), finite element method; (*b*)–(*e*), asymptotic expansion (1.165).

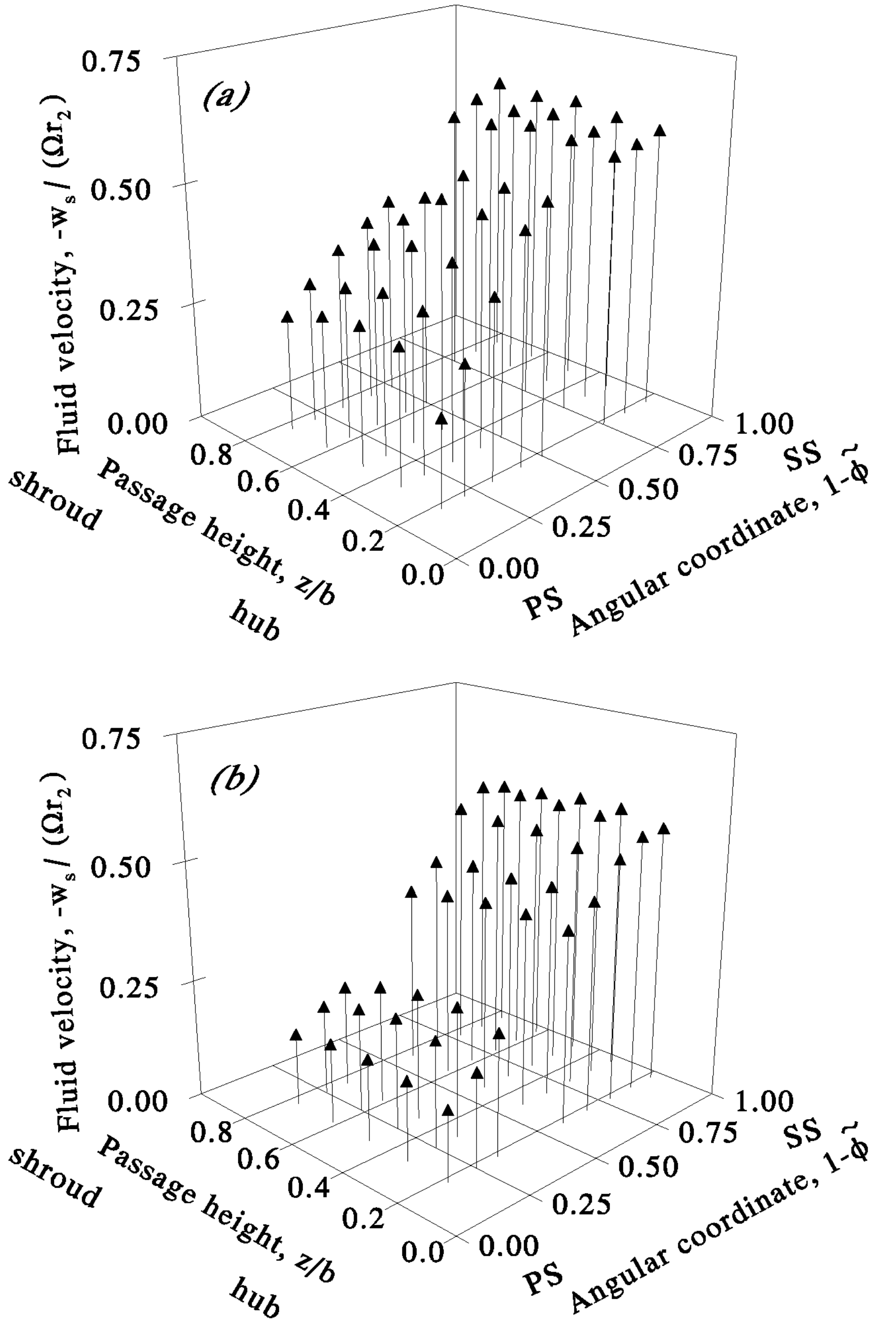

FIGURE 2.19. Cross-sectional passage velocities at $\Phi = -0.11$ for nine-bladed test impeller, measured at a radial distance $(r - r_1)/(r_2 - r_1)$ of (*a*) 1/6, and (*b*) 3/6.

observation, i.e. the fact that there is a next-to-zero pressure-side boundary layer growth, is of particular importance, since it means that the core flow will hardly be influenced, that is to say displaced, by the boundary layer on the pressure side of the blades. Stated differently, merely the development of the boundary layer along the blade suction side needs to be taken into account with regard to the displacement of the core flow (§ 2.3.4). It should, however, still be recognised that the boundary layer on the blade pressure side remains to be of importance regarding the determination of the viscous drag, and by consequence, for the prediction of the impeller efficiency.

Turning our attention to the results of the five-blade impeller, we further see that there is a region of considerable length along the blade pressure side with a next-to-zero core-flow velocity, which does not appear on the blade pressure side of the other two impellers. The reason for such taking place is that the five-bladed impeller is operated below minimum discharge, that is the (actual) volume flow rate coefficient lies below the minimum value prescribed by potential-flow theory (i.e. $-\Phi < -\Phi_m$); see also § 1.7.3. In this context, we further remark that for such below-minimum-discharge cases, potential-flow theory predicts that there would be an area of reverse flow along the blade pressure side, which evidently is not encountered because of the high relative magnitude of the viscous forces due to the low (expectantly-negative) fluid velocity relative to the blades. So, instead of areas of reverse flow we experience a region of flow obstruction in which the fluid is nearly at rest (relative to the blade). Nonetheless, the concept of minimum flow, i.e. the requirement $-\Phi > -\Phi_m$, still holds, only the interpretation of it is somewhat different.

Lastly, completing the discussion of the current subject-matter, we note that the cross-sectional hub-to-shroud measurements (figure 2.19) expose that there is a (nearly) uniform velocity distribution from hub to shroud, i.e. $\partial w(x,y,z)/\partial z \approx 0$, which corroborates the assumption of two-dimensional flow.

2.3.3 *Impeller performance*

We shall now proceed to outline the (actual) performance of the test impellers, and discuss it in view of the theoretical prediction. To that end, experimental data will be presented that was collected from performance tests that were carried out at three different angular speeds (i.e. 15, 30, and 45 r.p.m.) for each impeller.

In brief, these performance tests yielded impeller characteristics, measured in terms of the impeller periphery circulation Υ_2 $(= \Gamma_2/(2\pi\Omega r_2^2))$ and the volume flow rate coefficient Φ. The volume flow rate coefficient readily followed from the (Q_v) reading of the turbine flow meter, while the periphery circulation was computed from the (time-averaged) circumferential impeller discharge velocity $\bar{v}_\phi$ that was measured in the fixed frame just outside the impeller periphery at a distance of radial extent $r = 465$ mm; this way $\Upsilon_2 = r\bar{v}_\phi/(\Omega r_2^2)$.

The performance characteristics obtained in this way, are plotted in figure 2.20. This figure also displays the corresponding one-dimensional Eulerian value $(\Upsilon_{2E} = 1+\Phi\tan(\beta)))$ as well as the two-dimensional theoretical characteristic $(\Upsilon_{2th} = \sigma_\Omega + \Phi\tan(\beta))$. From the respective plots we see that the actual circulation around the impellers is reasonably well predicted near design discharge flow by the two-dimensional theoretical value. (N.B. Υ_2 is somewhat over-predicted near design discharge due to blockage of the passages.) The figure shows further that the impeller periphery circulation declines considerably at either side of the design point. These deviations are caused by less-than-perfect blade circulations, due

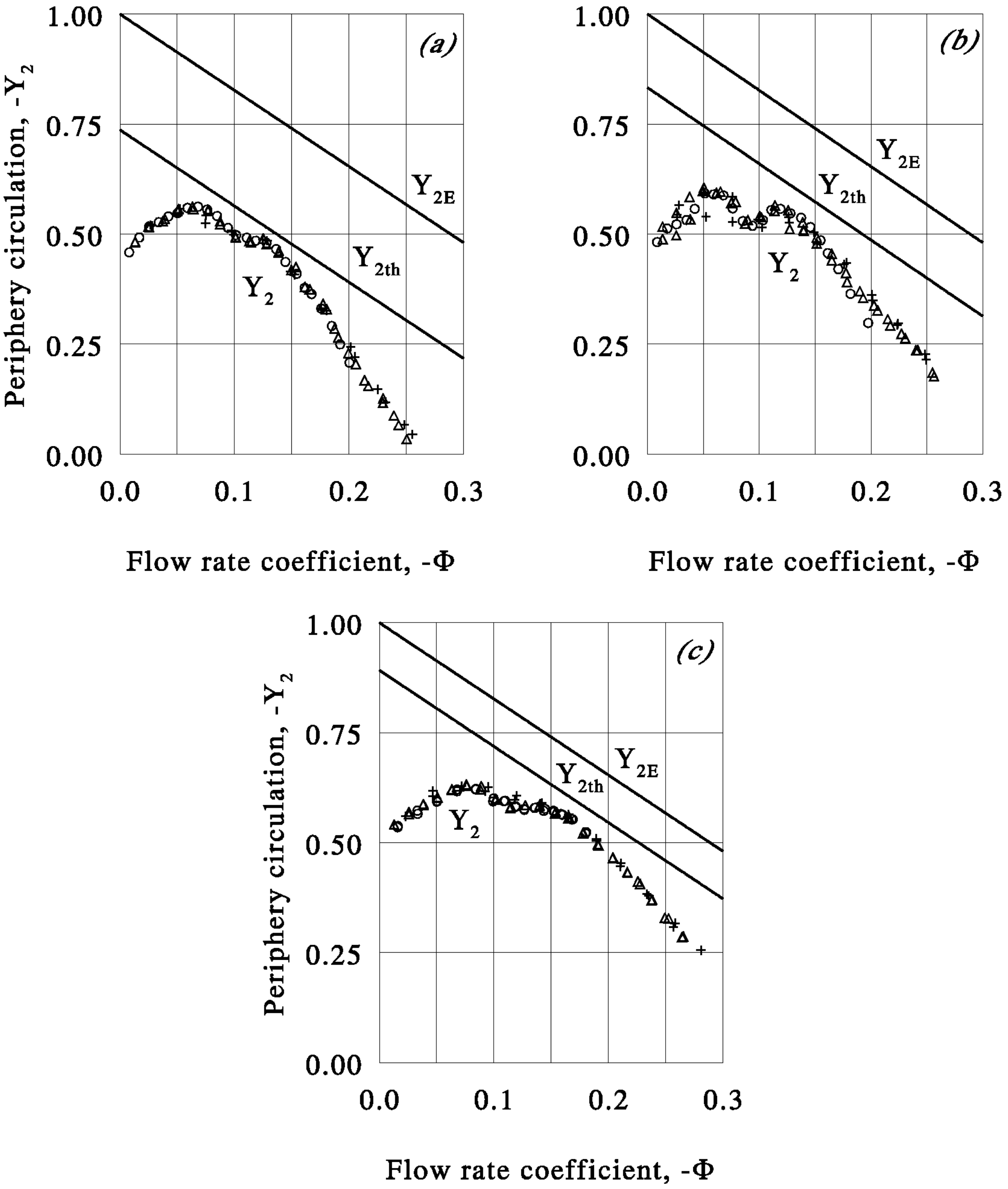

FIGURE 2.20. Performance characteristic of the (*a*) five-, (*b*) nine-, and (*c*) fifteen-bladed test impeller, with corresponding one-dimensional Eulerian (Υ_{2E}) and two-dimensional (inviscid) theoretical (Υ_{2th}) periphery circulation. Measurements at: +, 15 r.p.m.; △, 30 r.p.m.; ○, 45 r.p.m.

to the effect of viscosity at off-design operation—which may be explained as follows.

First, we consider the situation of high volume flow rates, that is discharge (well) above design. This type of operation will give rise to a separation bubble or reverse flow area near the leading edge on the pressure side of the blade. As a result the actual circulation ($n\Gamma_b$) around the impeller blades will be less than the (inviscid) potential-flow value. This situation gradually aggravates (i.e. higher circulation loss) when the volume flow rate increases, as is reflected in the plots of figure 2.20.

Next, we turn to the case of low (i.e. below-design-discharge) volume flow rates. Up to the inception of rotating stall, pinpointed at, say, $\Phi = \Phi_{RS}$, this will show a situation of (ordinary) stall on the suction side of the blades, and, hence, the actual blade circulation will lie below the theoretical value. Little by little this situation worsens (i.e. higher circulation loss) as the throughput is decreased. Decreasing the throughput however below Φ_{RS} will change the flow situation drastically, in that it will give rise to rotating stall, which causes the circulation to drop off rapidly because (some) blades will have next-to-zero or even non-positive circulations.

2.3.4 *Boundary layer at blade suction side*

The last item that will be discussed concerns the viscous boundary layers on the blade suction side, which, as we have seen, is quite substantial in magnitude. The development of the boundary layer along the blade pressure side, as noted before, was seen to be negligible, and will not be discussed[†]. Furthermore, the discussion of the subject-matter will be principally confined to (the calculation of) the displacement thickness.

The basic perception of the current analysis is that the common (flat-wall) thin-shear-layer (TSL) approximation applies (also) to the case of rotating low-specific-speed impellers equipped with blades of modest (i.e. sufficiently weak) curvature, so that calculations performed in the ordinary, i.e. direct-hierarchy, fashion can be employed to compute the blade-suction-side boundary layer. Additional conditions on the impeller speed (Ω) and the impeller-blade surface curvature to assure the validity of the assumption thereby being (see also Johnston & Eide 1976)

$$\left|\frac{\Omega\delta}{w_e}\right| \ll 1 \qquad \text{and} \qquad \left|\frac{\delta}{R_c}\right| \ll 1 \tag{2.6}$$

in which δ denotes the boundary-layer thickness, and where R_c is the local longitudinal radius of curvature, which for logarithmic spiral blades simply equals $r/\sin(\beta)$. Both conditions, as it turns out to be, hold in most of the practical cases concerning fluid flow in centrifugal impellers. In fact, effects of system rotation and surface curvature are for those situations of fluid flow fully accommodated in the description of the core flow. (N.B. Johnston & Eide 1974 pointed out that the TSL approximation applies as long as the above-mentioned parameters will not get as large as 0.05.)

To illustrate above-mentioned perception, the boundary layer (displacement thickness) on the blade suction side for all three test impellers was computed at $\Omega = 32$ r.p.m., by means of the integration method due to Truckenbrodt (see for instance Schlichting 1979, or Cebeci & Smith 1974). By way of approximation it was thereby assumed that the turbulent boundary layer started at $s = 0$, that is without a laminar inlet portion. Furthermore,

---

[†] See also the remark after the second paragraph at the beginning of § 2.3.

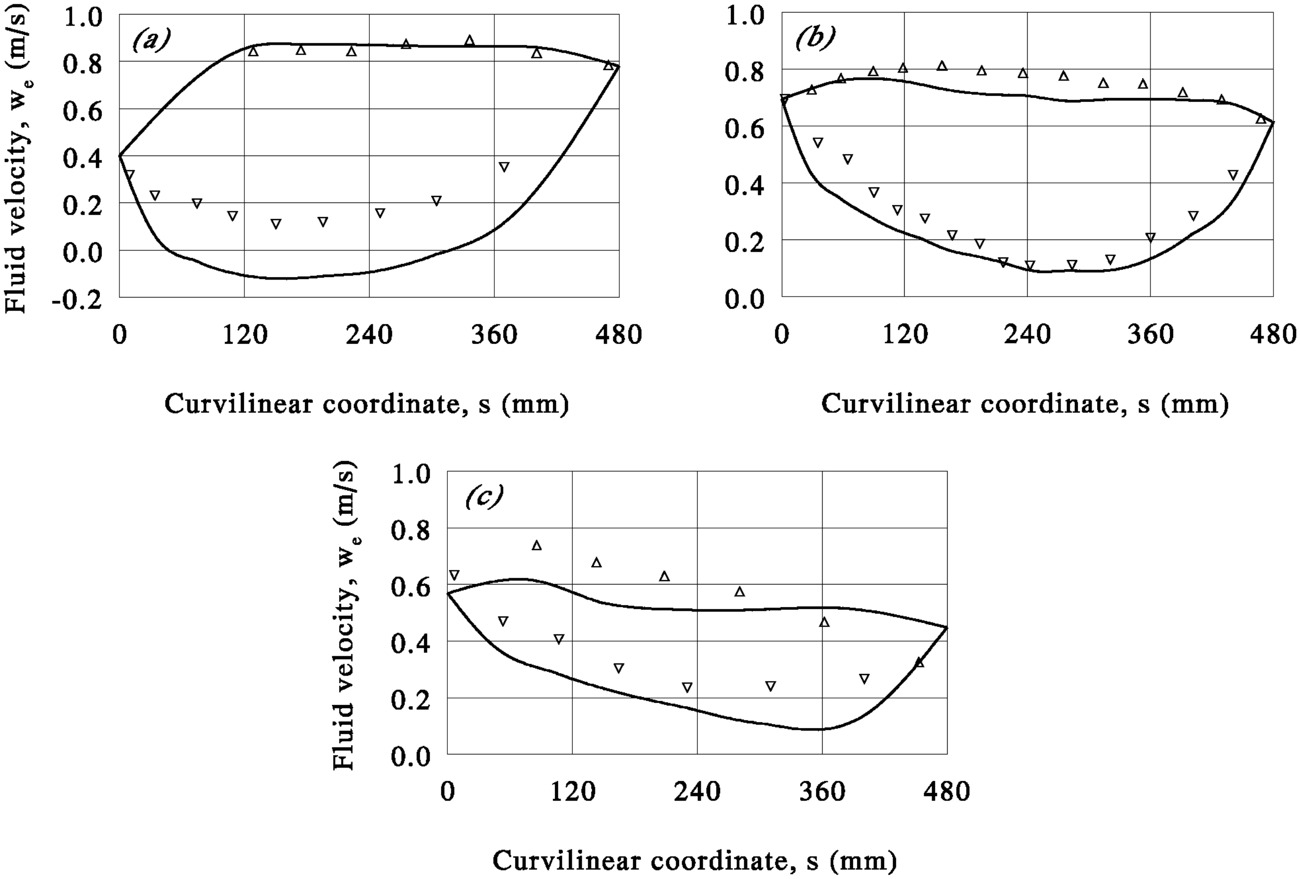

FIGURE 2.21. Longitudinal edge velocities at the blades of the (a) five-, (b) nine-, and (c) fifteen-bladed test impeller. Solid line indicates potential-flow calculation; Symbols indicate experimental values: $\triangle$, suction side; $\bigtriangledown$, pressure side.

it was supposed that the shape factors equalled the value corresponding to the case of a zero pressure gradient. This is strictly speaking not correct since we have a chiefly adverse pressure gradient, but the actual values do not differ more than a few percent from the zero-pressure-gradient values (see also Schlichting 1979). Therefore, the latter being (still) well suited for an engineering approach.

The results thus obtained, i.e. the displacement thickness $\delta_1(s)$, is presented graphically in figure 2.22. The graphs show computed values that are based on the potential-flow longitudinal edge velocity (w_e), as well as calculation results derived from the measured longitudinal edge velocity; see also figure 2.21. In figure 2.22 we have further plotted the corresponding experimental values obtained from the LDV flow measurements, which have been derived indirectly from the observed boundary-layer thickness (δ) by using the "corollary" $\delta_1 \approx 0.13\delta$. (By the law of the wake we know that $\delta_1/\delta = (c_f/2)^{\frac{1}{2}}(1+\Pi)/\kappa$, where c_f is the skin friction coefficient, $\kappa = 0.41$, and Π is Coles' parameter, which is about 0.2 for the current case of low-Reynolds-number turbulent boundary-layers, see also Monin & Yaglom 1971 and Cebeci & Smith 1974; the skin friction coefficient is estimated at 0.005 ($Re_s \approx 2\times10^5$) by applying the well-known formula of Schultz-Grunow, i.e. $c_f = 0.370\,(\log(Re_s))^{-2.584}$, see for instance Schlichting 1979, p. 643, or Monin & Yaglom 1971, p. 324.)

With reference to the respective plots, we see that there is good agreement between the experimentally obtained values of the displacement thickness and the theoretical calcula-

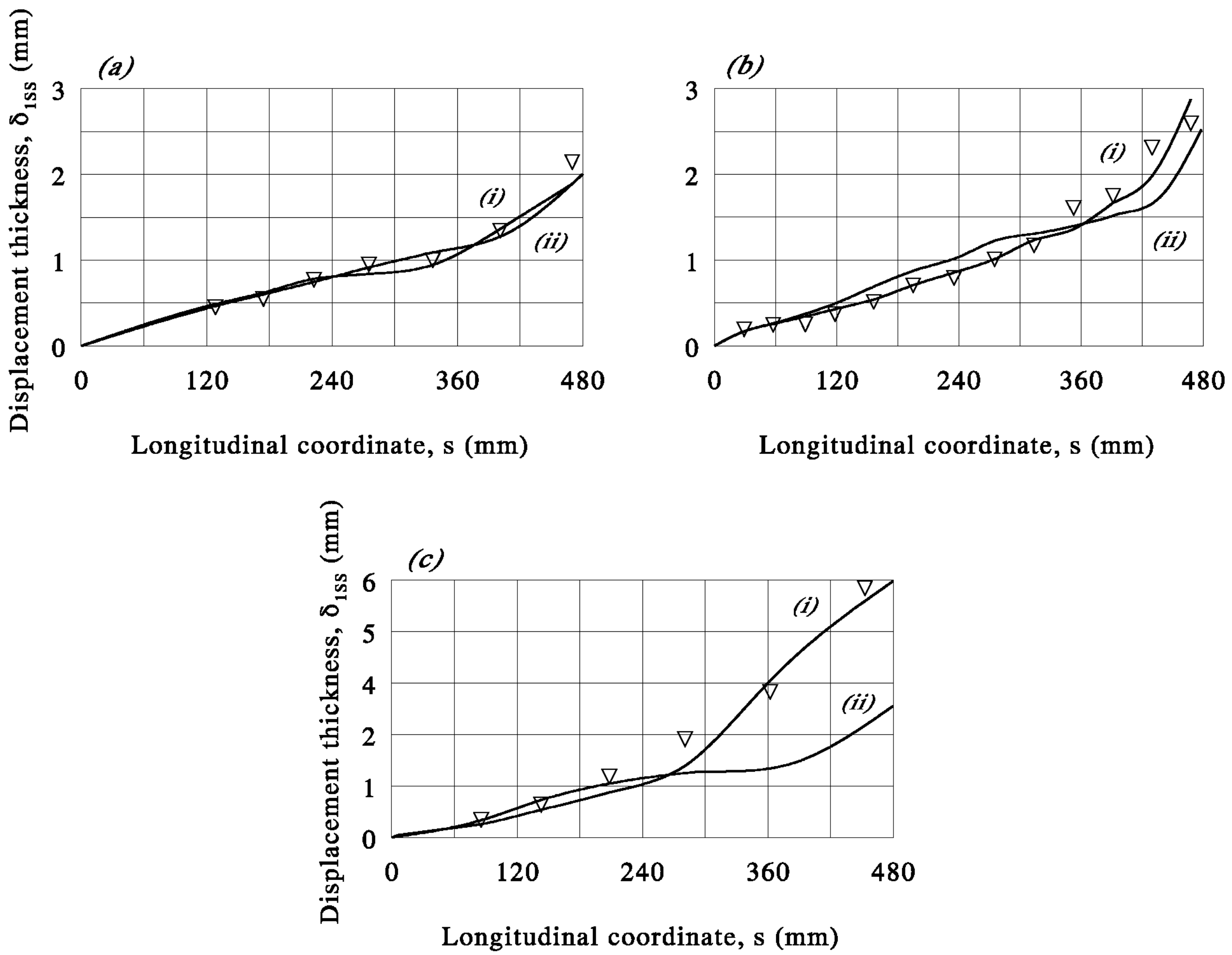

FIGURE 2.22. Measured and calculated displacement thickness on the suction side of the blades of the (*a*) five-, (*b*) nine-, and (*c*) fifteen-bladed test impeller. Experimental data indicated by symbols; solid lines indicate (*i*) prediction from potential-flow free-stream velocity, and (*ii*) calculation based on measured edge velocity (see also figure 2.21).

tions on the basis of the actual (measured) edge velocity. Further, we also detect proper agreement for the calculations performed with the potential-flow free-stream velocities, except for the fifteen-bladed test impeller. There we clearly see that the boundary-layer growth is under-estimated, due to the displacement interaction. (The fact that there is substantial displacement in the passages of the fifteen-bladed impeller became already apparent before, at the discussion of the blade-to-blade LDV flow measurements.)

In conclusion, taking into consideration the preceding results, it can be said that there is (apparently) no reason whatsoever to doubt whether or not the well-established ordinary approaches may be applied to calculate the boundary-layer on the suction side of the blades of low-specific-speed centrifugal impellers. This may seem quite obvious, but many hydrodynamicists think (or at least expect) otherwise. Only at high operating speeds, and for cases of strong blade-surface curvature, so that the conditions $|(\Omega\delta)/w_e| \ll 1$ and $|\delta/R_c| \ll 1$ are severely violated, it seems natural to expect that application of common direct-hierarchy flat-plate (TSL) approximations will yield improper results. Furthermore, it is emphasised that the passage flows are not fully-developed turbulent channel flows, but merely potential-flow core flows with thin low-Reynolds-number turbulent boundary layers on the blade-passage walls; provided, of course, that the passages are sufficiently wide with regard to the displacement due to the boundary-layer growth. In the event that the latter is not the case, like we saw well downstream the passages of the fifteen-bladed test impeller, the potential-flow concept still remains applicable, only one has to take into account the relative magnitude of the displacement thickness; that is, recompute the potential-flow free-stream velocity by incorporating the initial estimate of the displacement.

In connexion with the preceding argument, it is further brought to attention that many early experimental efforts regarding rotary flows, involved rotating-channel flows of which the core flow was essentially not free from vorticity (in the absolute sense); e.g. the works of Johnston, Halleen & Lezius (1972), Rothe Johnston (1976), and Kikuyama *et al.* (1993). It is therefore questionable whether or not the results of such studies are appropriate for turbomachinery flows, which are essentially irrotational in the absolute sense. In fact, flow systems rotating as a whole are not quite so representative for turbomachinery flows as often thought, because from the outset the frameworks of the respective flow problems differ. The only proper way to examine impeller passage flows experimentally, is by testing real (model) impellers—not by some rotating-channel apparatus.

2.4 Concluding remarks

Based on laser-Doppler-velocimetry flow measurements in the rotor frame of reference, supplemented by scanning-beam particle-image flow visualisations and digital image analysis, the flow inside the passages of three, 60° five-, nine-, and fifteen-bladed, low-specific-speed model centrifugal pump impellers of logarithmic design has been investigated in view of the theory described in chapter 1.

From the respective experimental results it has been shown that the core of the blade passage flow is well described by two-dimensional potential-flow theory. Particularly, the presence of the (potential-flow) relative eddy, which is responsible for the rotational slip in centrifugal impellers, has been corroborated in line with potential-flow theory by higher values of the passage velocities in the proximity of the blade suction side and near-stagnation flow at the blade pressure side.

Furthermore, the measurements have exposed that only the boundary layer on the blade suction side is substantial in magnitude, contrary to the one on the blade pressure side, which proved to be negligible in size. Additionally, it has been demonstrated that the boundary layer (i.e. the displacement thickness) on the blade suction side can be well computed by application of ordinary direct-hierarchy flat-plate boundary-layer theory, indicating that effects of system rotation and blade-surface curvature are well accommodated in the potential-flow description. Likewise, as yet not performed, it is expected that the boundary layer on the blade pressure side can be computed by a multistructured triple-deck approach (future investigation).

Apart from the immediate comparison to flow field calculations the measurements have further been discussed regarding the performance of the impellers, in terms of impeller periphery circulation. Here also good agreement was found between theoretical and experimental values; that is, near design discharge.

References

ABRAMIAN, M. & HOWARD, J. H. G. 1994*a* A rotating laser-Doppler anemometry system for unsteady relative flow measurements in model centrifugal impellers. *J. Turbomachinery* **116**, 260–268.

ABRAMIAN, M. & HOWARD, J. H. G. 1994*b* Experimental investigation of the steady and unsteady relative flow in a model centrifugal impeller passage. *J. Turbomachinery* **116**, 269–279.

ABRAMOWITZ, M. & STEGUN, I.A. 1972 *Handbook of Mathematical Functions with Formulas, Graphs, and Mathematical Tables.* John Wiley and Sons.

ACOSTA, A. J. 1954 An experimental and theoretical investigation of two-dimensional centrifugal impellers. *Trans. ASME* **76**, 749–763.

ADRIAN, R. J. 1991 Particle-imaging techniques for experimental fluid mechanics. *Annu. Rev. Fluid Mech.* **23**, 261–304.

AYYUBI, S. B. & RAO, Y. V. N. 1971 Theoretical analysis of flow through two-dimensional centrifugal pump impeller by method of singularities. *Trans. ASME* D: *J. Basic Engng* **93**, 35–41.

BADIE, R. 1993 Analysis of unsteady potential flows in centrifugal pumps—analytical and finite element calculations in a centrifugal volute pump. PhD thesis, University of Twente.

BACHELOR, G. K. 1967 *An Introduction to Fluid Dynamics.* Cambridge University Press.

BETZ, A. 1964 *Konforme Abbildung.* Springer.

BETZ, A. 1966 *Introduction to the Theory of Flow Machines.* Pergamon.

BUSEMANN, A. 1928 Das Förderhöhenverhältnis radialer Kreiselpumpen mit logaritmisch-spiraligen Schaufeln. *Z. Angew. Math. Mech.* **8**, 372–384.

CEBECI, T. & SMITH, A. M. O. 1974 *Analysis of Turbulent Boundary Layers.* Academic.

CUMPSTY, N. A. 1989 *Compressor Aerodynamics.* John Wiley and Sons.

DIXON, S. L. 1978 *Fluid Mechanics, Thermodynamics of Turbomachinery.* Pergamon.

ELGHOBASHI, S. 1994 On predicting particle-laden turbulent flows. *Appl. Sci. Res.* **52**, 309–329.

ELHOLM, T., AYDER, E. & BRAEMBUSSCHE, R. VAN DEN 1992 Experimental study of the swirling flow in the volute of a centrifugal pump. *J. Turbomachinery* **114**, 366–372.

ESCH, B. P. M. VAN 1995 Private communication. University of Twente.

ESSEN, T. G. VAN 1995 Fluid-induced impeller forces in centrifugal pumps—finite element calculations of unsteady potential flow in centrifugal pumps. PhD thesis, University of Twente.

FISHER, K. & THOMA, D. 1932 Investigation of the flow conditions in a centrifugal pump. *Trans. ASME* HYD-54-8, 141–155.

FISTER, W. 1966 Sichtbarmachung der Strömungen in Radialverdichterstufen, besonders der Relativströmung in rotierenden Laufrädern, durch Funkenblitze. *Brennst.-Wärme-Kraft* **18**, 425–429.

FOWLER, H. S. 1968 The distribution and stability of flow in a rotating channel. *Trans. ASME* A: *J. Engng Power* **90**, 229–236.

GRADSHTEYN, I. S. & RYZHIK, I. M. 1980 *Table of Integrals, Series, and Products.* Academic.

Howard, J. H. G. & Kittmer, C. W. 1975 Measured passage velocities in a radial impeller with shrouded and unshrouded configurations. *Trans. ASME* A: *J. Engng Power* **97**, 207–213.

Johnston, J. P., Halleen, R. M. & Lezius, D. K. 1972 Effects of spanwise rotation on the structure of two-dimensional fully developed turbulent channel flow. *J. Fluid Mech.* **56**, 533–557.

Johnston, J. P. & Eide, S. A. 1976 Turbulent boundary layers on centrifugal compressor blades: prediction of the effects of surface curvature and rotation. *Trans. ASME* I: *J. Fluids Engng.* **98**, 374–381.

Kikuyama, K., Maeda, T., Nishibori, K. & Nomura, S. 1993 Effects of channel rotation on turbulent boundary layers along a convex surface. *Trans. JSME* B **36**, 86–92.

König, E. 1922 Potentialströmung durch Gitter. *Z. Angew. Math. Mech.* **2**, 422–429.

Kucharski, W. 1918 *Strömungen einer reibungsfreien Flüssigkeit bei Rotation fester Körper.* R. Oldenbourg.

Lamb, H. 1932 *Hydrodynamics.* Cambridge University Press.

Lennemann, E. & Howard, J. H. G. 1970 Unsteady flow phenomena in rotating centrifugal impeller passages. *Trans. ASME* A: *J. Engng Power* **92**, 65–72.

Milne-Thomson, L. M. 1958 *Theoretical Aerodynamics.* Macmillan.

Miner, S. M., Beaudoin, R. J. & Flack, R. D. 1989 Laser velocimeter measurements in a centrifugal flow pump. *J. Turbomachinery* **111**, 205–212.

Mohana Kumar, T. C. & Rao, Y. V. N. 1977 Theoretical investigation of pressure distribution along the surfaces of a thin blade of arbitrary geometry of a two-dimensional centrifugal pump impeller. *Trans. ASME* I: *J. Fluids Engng* **99**, 531–542.

Monin, A. S. & Yaglom, A. M. 1971 *Statistical Fluid Mechanics: Mechanics of Turbulence.* MIT.

Moore, J. 1973 A wake and eddy in a rotating, radial-flow passage. Part 1: Experimental results. *Trans. ASME* A: *J. Engng Power* **95**, 205–212.

Moretti, G. 1964 *Functions of a Complex Variable.* Prentice Hall.

Pfleiderer, C. 1991 *Strömungsmaschinen.* Springer.

Prandtl, L. 1963 *Essentials of Fluid Dynamics.* Blackie and Son.

Schlichting, H. 1979 *Boundary-Layer Theory.* McGraw-Hill.

Rothe, P. H. & Johnston, J. P. 1976 Effects of system rotation on the performance of two-dimensional diffusers. *Trans. ASME* I: *J. Fluids Engng* **98**, 422–430.

Schulz, W. 1928*a* Das Förderhöhenverhältnis der Kreiselpumpen für die ideale und wirkliche Flüssigkeit. *Forschg. Ing.-Wes.* vol. 307. VDI Verlag.

Schulz, W. 1928*b* Das Förderhöhenverhältnis radialer Kreiselpumpen mit logaritmisch-spiraligen Schaufeln. *Z. Angew. Math. Mech.* **8**, 10–17.

Spannhake, W. 1925*a* Die Leistungsaufname einer parallelkränzigen Zentrifugalpumpe. *Festschrift der Technische Hochschule Karlsruhe*, pp. 387–400.

Spannhake, W. 1925*b* Anwendung der Konforme Abbildung auf die Berechnung von Strömungen in Kreiselrädern. *Z. Angew. Math. Mech.* **5**, 481–484.

Spannhake, W. 1930 Eine strömungstechnische Aufgabe der Kreiselradforschung und ein Ansatz zu ihrer Lösung. *Mitteillungen des Instituts für Strömungsmaschinen der Technische Hochschule Karlsruhe*, pp. 4–38.

Sörensen, E. 1927 Potentialströmungen durch rotierende Kreiselräder. *Z. Angew. Math. Mech.* **7**, 89–106.

Sörensen, E. 1941 Potential flow through centrifugal pumps and turbines. *NACA TM 973.*

STEWARTSON, K. 1974 Multistructured boundary layers on flat plates and related bodies. *Adv. Appl. Mech.* **14**, 145–239.

UCHIMARU, S. 1925 Experimental research on the distribution of water pressure in a centrifugal impeller. *J. Fac. Engng, Tokyo Imperial University* **16**, 157–169.

UCHIMARU, S. & KITO, S. 1931 On potential flow of water through a centrifugal impeller. *J. Fac. Engng, Tokyo Imperial University* **19**, 191–223.

VAVRA, M. H. 1960 *Aero-Thermodynamics and Flow in Turbomachines.* John Wiley and Sons.

VISSER, F. C. 1991 Two-dimensional potential flow through a centrifugal impeller. MSc thesis, University of Twente.

VISSER, F. C., BROUWERS, J. J. H. & BADIE, R. 1994 Theoretical analysis of inertially irrotational and solenoidal flow in two-dimensional radial-flow pump and turbine impellers with equiangular blades. *J. Fluid Mech.* **269**, 107–141.

VISSER, F. C. & JONKER, J. B. 1995*a* Laser doppler velocimetry flow measurements in the rotating frame inside the passage of a low specific speed model centrifugal pump impeller. *Proceedings of the sixth international conference on laser anemometry—advances and applications, August 13–18, Hilton Head Island, South Carolina, USA*, pp. 139–151.

VISSER, F. C. & JONKER, J. B. 1995*b* Investigation of the relative flow in low specific speed model centrifugal pump impellers using sweep-beam particle image velocimetry. *Proceedings of the seventh international symposium on flow visualisation, September 11–14, Seattle, Washington, USA*, pp. 654–659.

WESTERWEEL, J. 1993 Digital particle image velocimetry—theory and application. PhD thesis, Delft University of Technology.

WESTERWEEL, J. 1994 Efficient detection of spurious vectors in particle image velocimetry data. *Exp. Fluids* **16**, 236–247.

WIESNER, F. J. 1967 A review of slip factors for centrifugal impellers. *Trans. ASME* A: *J. Engng Power* **89**, 558–572.

WHITTAKER, E. T. & WATSON, G. N. 1927 *A Course of Modern Analysis.* Cambridge University Press.

Summary

In this thesis it has been shown that the flow of an incompressible fluid in the passages of centrifugal impellers of low specific speed can be well described by a potential-flow formulation of the inviscid core flow, supplemented by ordinary direct-hierarchy boundary-layer calculations to take account of the suction-side core-flow displacement due to viscosity. Thus reads the overall conclusion of the investigation that might be summarised as follows:

Firstly, a comprehensive mathematical analysis has been carried out on the basis of two-dimensional, irrotational, and solenoidal (core) flow in model centrifugal impellers that are made free from their surroundings. From this analysis, that rests heavily on the findings of complex-function theory and the theory of special functions, new formulations for the calculation of important quantities in the field of turbomachinery (design) have emerged. These quantities pertain to the velocity field, the pressure distribution, and a number of impeller design parameters like the slip factor, that plays an important role in the prediction of the head, and the minimum flow rate coefficient to determine the correct blading so that a proper passage flow is accomplished. These analytic results all give a large quantity of important information about the operation of radial-flow impellers, and, moreover, can serve as a practical and meaningful reference for numerical methods used to compute turbomachinery flow fields.

Secondly, the analytic results, particularly the fluid velocity in the blade passages, have been verified by means of laser-Doppler-velocimetry flow measurements conducted on three perspex model centrifugal pump impellers in a custom-designed test facility, which were supplemented by particle-image flow visualisations and digital images analyses. These experiments have clearly shown that the concept of a potential flow, supplemented by (suction-side) boundary-layer calculations holds well for low-specific-speed impeller passage flows. In addition, as indicated by the measurements, it has been found that the viscous boundary layer on the blade pressure side is of a next-to-zero thickness, whereas the viscous boundary layer on the blade suction side proved to be of considerable magnitude.

Lastly, on the basis of the observations, the theory has been further examined with respect to the impeller performance and the boundary-layer (displacement) thickness at the blade suction side. Regarding the latter, it has been shown that the common boundary-layer approach is well applicable to the type of passage flows considered here, in that calculations performed in the ordinary (direct-hierarchy) fashion predicted the boundary-layer development successfully. Likewise, the results of the performance tests were most satisfactory. Particularly near design discharge, the computed values were in good agreement with the measurement results.

Samenvatting

In dit proefschrift is aangetoond dat de stroming van een incompressibele vloeistof in de kanalen van centrifugaalwaaiers met een laag specifiek toerental goed kan worden beschreven met behulp van een potentiaalformulering voor de invisceuse hoofdstroom, aangevuld met gewone traditionele grenslaagberekeningen ter verdiscontering van de vloeistofverdringing aan de zuigzijde van de schoepen als gevolg van viscositeit. Aldus luidt de algemene conclusie van het onderzoek dat als volgt kan worden samengevat:

Om te beginnen is een wiskundige analyse opgezet op basis van een twee-dimensionale rotatie- en divergentievrije stroming in model centrifugaalwaaiers die zijn vrijgemaakt van hun omgeving. Deze analyse, die sterk leunt op de bevindingen van de complexe-functie theorie alsook de kennis van speciale functies, heeft geleid tot nieuwe relaties voor het berekenen van grootheden die van belang zijn voor het (voor-)ontwerpen van roterende stromingsmachines. Deze grootheden hebben betrekking op het snelheidsveld, de drukverdeling, en ontwerpparameters zoals de slipfactor, die belangrijk is ten aan zien van het voorspellen van de opvoerhoogte, en de coefficient voor het minimumdebiet ter bepaling van het benodigde aantal schoepen opdat een goede stroming wordt verkregen. Deze analytische resultaten verschaffen ruime informatie ten aanzien van de werking van radiaal doorstroomde waaiers, en dienen bovendien als een praktische referentie voor toetsing van numerieke berekeningsmethoden op het gebied van radiale-stromingsmachines.

Vervolgens zijn de analytische bevindingen, in het bijzonder de vloeistofsnelheid in de waaierkanalen, geverifieerd aan de hand van snelheidsmetingen op basis van laser Doppler velocimetry en particle-image stromingsvisualisatie met image-analyse, welke zijn uitgevoerd in drie perspex modelwaaiers in een speciaal daarvoor ontwikkelde testopstelling. Deze experimenten hebben duidelijk naar voren gebracht dat het concept van een potentiaalstroming, aangevuld met grenslaagberekeningen (aan de zuigzijde van de schoepen), goed standhoudt voor het berekenen van de stroming in waaiers met een laag specifiek toerental. Daarnaast, zoals aangegeven door de metingen, blijkt de grenslaag aan de drukzijde van een schoep een niet-waarneembare dikte te hebben, terwijl de grenslaag aan de zuigzijde van aanmerkelijke dikte is.

Tenslotte is op basis van de observaties de theorie nader beschouwd ten aanzien van de waaier-*performance* en de grenslaag – verdringings – dikte aan de zuigzijde van een schoep. Met betrekking tot laatst genoemde, blijkt dat de traditionele (directe hierarchie) grenslaagaanpak ook voor de hierbeschouwde stromingen toepasbaar is, gezien het feit dat de berekeningen goed overeenstemmen met de gemeten grenslaagdikte. Zo ook zijn de resultaten met betrekking tot de *performance* zeer bevredigend te noemen. In het bijzonder rond het ontwerpbedrijfspunt was de berekende waarde hiervan in goede overeenstemming met de meetresultaten.

Acknowledgements

The work presented in this thesis can, of course, not be credited to one person only. In the course of the investigation, several people have assisted to achieve the respective results, and their help is gratefully acknowledged. Particularly, I am indebted to the persons listed below.

Supervision:	J.J.H. Brouwers[*]
	J.B. Jonker[*]
Students:	R. Batenburg[**]
	D.J. Bussink[*]
	M.E. van der Horst[**]
	J. de Roos[*]
	D.J. Schuitemaker[**]
	J.W. Verkaik[*]
	J.G.G. Wannet[*]
	R.R. van der Woude[*]
Technical Support:	C.A. Bakker[*]
	J.B.M. Bossink[*]
Co-assistance:	M. Kwast[*]

Furthermore, I very much appreciated the cooperation (in the J.M. Burgers Centre for fluid mechanics) with Dr. J. Westerweel (PIVware) of Delft University of Technology, and the support from the Laboratory of Heat and Fluid Dynamics (University of Twente). Also, I am grateful for the input that I received from Prof. L. van Wijngaarden (method of conformal mapping) and Dr. D. Dijkstra (mathematics) of the University of Twente. Further, it is noted that the software that was used for the digital PIV analysis (PIVware) originated from the Laboratory for Aero and Hydrodynamics of Delft University of Technology, while part of the experimental program was sponsored by Shell–The Netherlands.

In addition, I wish to thank my wife Lenneke for her support, understanding, and encouragement. Besides that I appreciate her effort to read through the manuscript—which must have been a dull job for a psychologist (!).

F. C. V.

---

[*] Laboratory of Thermal Engineering, University of Twente.

[**] Hogeschool Alkmaar.